

FLUORESCENT COLLOIDAL SILICA RODS

SYNTHESIS AND PHASE BEHAVIOR

Anke Kuijk

Fluorescent colloidal silica rods

Synthesis and phase behavior

Cover: Scanning electron microscopy image of silica rods in a smectic phase

PhD thesis, Utrecht University, The Netherlands, January 2012

ISBN 978-90-393-5720-0

A digital version of this thesis is available at <http://www.colloid.nl>

Fluorescent colloidal silica rods

Synthesis and phase behavior

Fluorescente colloïdale silicastaafjes

Synthese en fasegedrag

(met een samenvatting in het Nederlands)

Proefschrift

ter verkrijging van de graad van doctor aan de
Universiteit Utrecht op gezag van de rector magnificus,
prof. dr. G.J. van der Zwaan, ingevolge het besluit van het
college voor promoties in het openbaar te verdedigen
op maandag 23 januari 2012 des middags te 2.30 uur

door

Anke Kuijk

geboren op 3 december 1983 te Deventer

Promotor: Prof. dr. A. van Blaaderen

Co-promotor: Dr. A. Imhof

Contents

Chapter 1.	Introduction	1
Part 1.	Preparation of rods	7
Chapter 2.	Synthesis of rod-like silica colloids	9
Chapter 3.	Preparation of silica rods for quantitative 3D confocal laser scanning microscopy	27
Part 2.	Phase behavior of rods in external fields	49
Chapter 4.	Phase behavior of colloidal silica rods studied in real and reciprocal space	51
Chapter 5.	Phase behavior of rods in an external electric field	77
Chapter 6.	Rods in combined shear and gravitational fields	95
Chapter 7.	Directing smectic liquid crystal phases of silica rods by colloidal epitaxy	105
	Bibliography	119
	Summary	128
	Samenvatting voor iedereen	131
	Dankwoord	138
	Curriculum Vitae	140

1

Introduction

1.1. COLLOIDS

Colloids are hidden in many substances that we use in everyday life. Without realizing, we eat them, drink them or put them on our skin or walls. They even flow through our veins. Mayonnaise, milk, creams, paint, and blood are examples of colloidal systems. Generally, colloidal dispersions consist of two phases that do not mix. One of these phases consists of particles in the size-range of nanometers to micrometers: the colloids. The other phase consists of much smaller units and is considered as a continuum: the solvent. Both colloid and solvent can be any phase: gas, liquid or solid. They can even be of the same phase, except for two gas phases since all gasses are mutually miscible. Paint, for instance, consists of solid particles in a liquid. Liquid fat droplets in water make milk and foams are gas bubbles in liquids or solids.

The word colloid was introduced by Thomas Graham. He studied diffusion through membranes and found that a sticky substance was filtered out of certain aqueous solutions by a parchment membrane [1]. The particles that stuck to the membrane were called colloids, after the Greek word *κόλλα* for glue. Nowadays, the term ‘colloid’ is used for any type of particle in the size-range from nanometers to micrometers. This size-range is set by two limits. On the one hand, the particles must be larger than the solvent molecules. On the other hand, the particles must be small enough to experience Brownian motion. Brownian motion is the diffusive motion that is caused by solvent molecules that collide with the colloid. For large objects, the forces that are exerted via these collisions are averaged out for all directions, resulting in movement according to the laws of mechanics only. Colloids, however, are small enough to experience the forces from fluctuations in the number of collisions by solvent molecules individually and are

therefore kicked around in their environment. This kind of movement was first observed by Robert Brown, who studied grass pollen in water [2]. The theoretical explanation for the phenomenon was given later by Albert Einstein [3], in combination with the experimental verification by Jean Baptiste Perrin [4, 5].

As may be evident from the previously mentioned examples, the study of colloidal systems is important to several areas of industry. The food industry, for example, but also the paint, coating and cosmetics industry benefit from detailed knowledge of colloid science. But beside their application in many industrial products, colloids are also used as a model system for more fundamental studies on the behavior of condensed matter [6]. Because of their Brownian motion, colloids show the same thermodynamic phase behavior as atoms and molecules [7]. Unlike atoms and molecules, however, the time and length scale of colloidal behavior is experimentally easily accessible. Simple light microscopy techniques can be used to visualize colloids, while for molecular systems advanced techniques like atomic force microscopy (AFM) or scanning tunneling microscopy (STM) are needed. Also, colloids move much slower than molecules; a typical colloid with a radius of 500 nm diffuses its own radius in half a second, which makes real-time observations possible. By using confocal laser scanning microscopy, it is even possible to obtain 3D quantitative data from colloidal systems.

1.2. LIQUID CRYSTAL PHASES

The phase behavior of the most simple, spherical particle consists of four different phases: the gas, the liquid, the crystal and the glass phase [8]. When the shape of the particles becomes less symmetrical (elongated or disk-like), a variety of phases with mechanical and symmetry properties that are intermediate between those of a liquid and a crystal can be added to these four. These phases are called liquid crystalline or mesomorphic phases (for an extensive introduction to liquid crystals see reference [9]). The classification of these phases is essentially based on their symmetry and was first set out by Georges Friedel in 1922 [10]. There are three major classes of liquid crystal phases: nematics, smectics and columnar phases. The arrangement of particles in the phases between the fully liquid (isotropic) and fully crystalline phase is shown in Fig. 1.1.

In the fully liquid, or isotropic, phase the particles show no positional or orientational order at all. The liquid crystal phase that shows most similarities with the liquid phase is the nematic phase. The term ‘nematic’ was thought of by Friedel and comes from the Greek word $\nu\eta\mu\alpha$, which means thread. It refers to the thread-like defects (disclination lines) that are commonly observed in nematic materials. In the nematic phase the particles do not show long-range positional order, but do point in the same direction. This direction can be indicated by a unit vector, which is called the director.

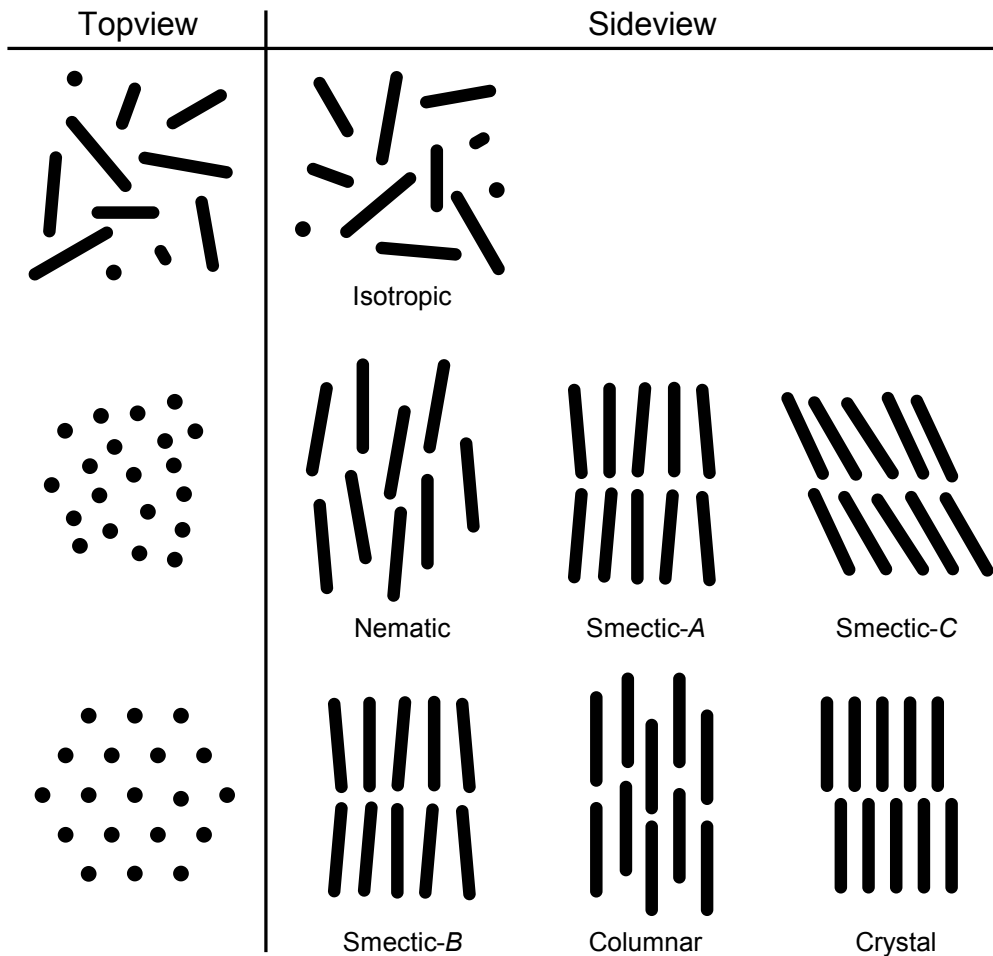


FIGURE 1.1. Schematic representation of several liquid crystal phases.

In the smectic phase, orientational order is accompanied by quasi-long-range order in one dimension; the particles form layers. Since the smectic phase possesses mechanical properties reminiscent of soaps, Friedel used the Greek word $\sigma\mu\eta\gamma\mu\alpha$, which means soap, to name the phase. The way the particles are organized inside the layers of the smectic phase depends on the type of smectic. In a smectic-*A*, for example, the rods are oriented parallel to the layer's normal and show no long-range positional order within the layers. Each layer is essentially a 2D-liquid. The smectic-*C* has the same properties, except that the rods inside the layers are now tilted with respect to the layers normal. When the rods inside the layers are oriented parallel to the layer's normal and additionally ordered in a hexagonal way, showing long range bond orientational order but no long range positional order, the smectic is called hexatic smectic-*B*. In a full smectic-*B*, the positional hexagonal order inside the layers is also long-range, making the structure in fact a three-dimensional stack of crystalline layers that are weakly attached to each other.

The third type of liquid crystal phase is the columnar phase. In this phase, the particles are ordered in columns, without long-range order along the columns. Often, these columns are ordered on a lattice themselves as well. The hexagonal columnar phase, for example, consists of rods that are ordered in columns, which in their turn are ordered on a hexagonal lattice.

Although classified in 1922, the first experimental observations of liquid crystals were reported in 1888 already. Botanical physiologist Reinitzer and physicist Lehmann studied cholesterol derivatives, which are now known as cholesteric liquid crystals [11, 12]. Other building blocks for liquid crystal phases include elongated organic molecules such as *p*-azoxyanisole [13], discoid organic molecules such as hexasubstituted phenylesters and polymers. Most of these molecular liquid crystals (MLCs) are thermotropic: their phase transitions are induced by varying temperature. As mentioned before, colloids show the same thermodynamic phase behavior as atoms and molecules. Therefore, there are also colloidal systems that form liquid crystal phases. In contrast to MLCs, colloidal liquid crystals are mainly lyotropic: they undergo phase transitions as a function of concentration. However, there are examples of colloidal systems, such as micelles, that show (weak) thermotropic behavior as well. The first reports of colloidal liquid crystals date back to the 1920s, when a nematic phase was found in systems of vanadium pentoxide ribbon-like particles [14]. Nematic phases were also observed for systems of rod-like tobacco mosaic virus (TMV) in the 1930s [15]. The smectic phase that also occurs in this system was reported in 1950 [16]. Later, liquid crystal phases were found in many more colloidal systems, including mineral particles such as goethite (α -FeOOH) [17] and gibbsite ($\text{Al}(\text{OH})_3$) [18, 19], and bio-organic particles like *fd*-virus or DNA [20, 21].

Recently, systems have been developed that can be used in confocal microscopy studies so that quantitative 3D studies of colloidal liquid crystals are possible. E.g., poly(methyl methacrylate) (PMMA) ellipsoids were produced by stretching PMMA microspheres imbedded in elastic poly-(dimethylsiloxane) [22, 23]. These particles were used to study the nematic order of colloidal rods in a centrifugal field [24]. The colloidal silica rods that are described in this thesis are a beautiful addition to the collection of anisotropic colloids that can be studied in 3D real-space. We will show that these rods form both nematic and smectic phases, in contrast to the PMMA ellipsoids for which only nematics have been observed.

Theoretical studies on liquid crystals date back to 1949, when Onsager showed that a system of long, hard rods that interact purely through repulsive forces exhibits orientational (nematic) order when the density is increased from the isotropic liquid phase [25]. This is caused by a gain in translational entropy at the higher concentrations of the nematic phase, which dominates the loss in orientational entropy. Later, computer

simulations have shown that systems of hard spherocylinders do not only form nematic phases, but also smectic and crystalline phases [26, 27].

1.3. EXTERNAL FIELDS

In contrast to atoms and molecules, colloids are very susceptible to external fields due to their relatively large size. This susceptibility can be exploited to control a colloidal dispersion either by steering the interactions between the particles or by bringing the suspension into nonequilibrium in a controlled way [28]. Because the extent of their influence is adjustable and often also reversible, external fields are extensively used in many applications. An example of this is e-paper [29]. The technology behind e-paper relies on electrophoretic motion; charged colloids are attracted to positive or negative electrodes. By using oppositely charged particles of different colors, it is possible to switch from, for instance, black to white by changing the direction of the electric field. Another effect of electric fields on which applications are based is the electro-rheological effect: the electric field induces dipole-dipole interactions between particles which lead to changes in the structure of the suspensions [30, 31]. Consequently, the flow behavior of the suspension changes. This effect is used in, for instance, hydraulic valves, brakes and displays [32, 33]. Since understanding of the effect of external fields on colloidal behavior is clearly relevant, we explored the effects of gravity, electric fields, shear and templates on dispersions of colloidal rods in part 2 of this thesis.

The most common external field that acts on colloids is gravity. Since it is very hard to match the density of colloid and solvent exactly, gravity almost always influences colloidal behavior. It can only be truly eliminated by performing experiments in space [34]. Gravity makes colloids that are not density-matched sediment. This gives rise to an equilibrium sedimentation profile, in which the volume fraction varies with height (high at the bottom and low on top). In the case of hard-spheres, sedimentation profiles have been used to check the hard-sphere equation of state experimentally [35–37].

Other external fields, such as electric or magnetic fields, shear flow and templates are used in addition to the gravitational field to manipulate the phase behavior of colloids. For anisotropic particles, we know that external fields can be used to align particles. Goethite particles, for example, were aligned with a magnetic field [38] and titanium dioxide ellipsoids with an electric field [39]. The alignment of liquid crystals is interesting because liquid crystal phases also have special optical properties, such as birefringence, which is used in display applications (the liquid crystal display, or LCD) [40]. In LCDs two types of external fields are used: templates and electric fields. The templates are used to create a twisted nematic state between two perpendicularly oriented polarizers, so that polarized light is guided and oriented with the nematic phase and passes through the second polarizer. However, when an electric field is

applied, the nematic phase aligns with the field and the light is not reoriented inside the cell anymore, so that it cannot pass the second polarizer.

1.4. OUTLINE OF THIS THESIS

In this thesis, we describe the synthesis of silica rods and their phase behavior in several external fields. **Part 1**, which includes Chapter 2 and 3, focusses on the development of this new anisotropic colloidal model system that can be used to study rod-like particles in 3D real-space. The simple one-pot method that is used to synthesize silica rods is discussed in detail in **Chapter 2**, as well as the comparison of the material properties of our system of rods with the classic ‘Stöber’ system of silica spheres. In **Chapter 3** is described what adaptations are needed to make the system suitable for confocal microscopy studies. Here, fluorescent labeling, single particle imaging and image analysis are addressed.

In **Part 2** of this thesis, the rods are used as a model system to study the phase behavior of rod-like systems in several external fields on the single particle level. We start by studying the system in the most common external field: gravity. In **Chapter 4**, confocal microscopy and small angle X-ray scattering are used to analyze the phase behavior of rods in gravity. In the next chapters, other external fields are added to influence the rods’ normal phase behavior. First, the behavior of rods in an external electric field is studied in **Chapter 5**. Here, we compare experiment and theory on the induced dipole moment of rods and report on the observation of a crystal phase that had never been seen in experiments before. Second, shear flow was used to align the rods and create aligned smectic and columnar phases in **Chapter 6**. Finally, the effect of templates on a sediment of rods is studied in **Chapter 7**.

Part 1

Preparation of rods

2

Synthesis of rod-like silica colloids

ABSTRACT

Although the experimental study of spherical colloids has been extensive, similar studies on rod-like particles are rare because suitable model systems are scarce. To fulfill this need, we present the synthesis of monodisperse rod-like silica colloids with tunable dimensions. Rods were produced with diameters of 200 nm and larger and lengths up to 10 μm , which resulted in aspect ratios ranging from 1 to 25. The longer aspect ratio rods formed both nematic and smectic liquid crystal phases. The growth mechanism of these rods involves emulsion droplets of water in pentanol, inside which silica condensation takes place. Since the silica nucleus is attached to the water/pentanol interface, the supply of reactants to the nucleus is anisotropic, causing it to grow on one side only, which results in rod formation. The material properties of the resulting silica rods were compared to those of Stöber silica spheres.

2.1. INTRODUCTION

Dispersions of rods exhibit various states of orientational and positional ordering, depending on aspect ratio and density. Liquid crystal phases, in which the rods are oriented, but do not show positional ordering in all three dimensions, have been studied in theory since 1949. Onsager was the first to show that a system of long, hard rods that interact purely through repulsive forces exhibits orientational (nematic) order when the density is increased from the isotropic liquid phase [25]. Later, computer simulations have shown that not only nematic, but also smectic and crystalline phases can occur in systems of hard spherocylinders, and phase diagrams were calculated as a function of density and aspect ratio [26, 27].

The experimental study on the phase behavior of rods has been less extensive. While spherical colloids have proven to be an excellent model system to study the phase behavior of atoms and molecules, similar systems to study rods are rare. Nevertheless, examples of liquid crystal phase behavior have been observed using bio-organic rods (such as fd-virus, TMV, or DNA [20, 21, 41]) as well as inorganic materials such as boehmite, vanadium pentoxide or β -ferric oxyhydroxide [42–44]. The first real space observation of rods ordering was reported by Maeda in 2003 [45]. However, 3D reconstructions of the systems that were used in this work are difficult because of the high refractive index of the materials used. To solve this problem, for colloidal spheres materials are used that can be index matched and imaged by confocal laser scanning microscopy (CLSM). Examples of such materials are poly(methyl methacrylate) (PMMA) and silica. Methods to fabricate rod-like particles from these materials were reported by Keville et al. [22], Ho et al. [23] and van Kats et al. [46]. The first two described a method to produce PMMA ellipsoids of various aspect ratios by stretching PMMA microspheres embedded in elastic poly-(dimethylsiloxane). Mohraz et al. [47] showed that it is possible to image these particles by CLSM and track their positions and orientations. Although this seems a promising system that shows a nematic phase, no smectic phases were observed for ellipsoidal particles as far as we know. A system of silica rods was developed by van Kats et al. [46], but the semi-2D nature of the procedure limits the possibilities of using this system to study concentrated dispersions of rods. Another system of anisotropic colloids are silica dumbbells, which can also be imaged in real space, but do not form liquid crystal phases because of their too small aspect ratio [48, 49].

In this chapter we present the wet-chemical synthesis of rod-like silica colloids. This synthesis has a high yield and provides easily enough particles to study concentrated dispersions because of its bulk nature. The synthesis was inspired by the work of Zhang *et al.*, who describe the formation of anisotropic silica nanostructures. They hypothesized that these structures were formed due to the presence of gold induced

polyvinylpyrrolidone (PVP) aggregates [50]. Our experiments however, led to new insights, alterations to the synthesis and an alternative model for the growth mechanism of silica rods, which is completely uncoupled from the gold particles.

2.2. EXPERIMENTAL

2.2.1. Synthesis

Rods with a length of 1.7 μm and a diameter of 225 nm were prepared as follows. In a closed 500 ml glass laboratory bottle, 30 g of polyvinylpyrrolidone (PVP, average molecular weight $M_n = 40.000$, Sigma-Aldrich) was dissolved in 300 ml of 1-pentanol ($\geq 99\%$, Sigma-Aldrich) by sonication for 2 hours. When all PVP had been dissolved, 30 ml of absolute ethanol (Baker), 8.4 ml of ultrapure water (Millipore system) and 2 ml of 0.18 M sodium citrate dihydrate (99%, Aldrich) solution in water was added to the pentanol. The flask was shaken by hand to mix the content, which then became turbid because an emulsion was formed. Subsequently, 6.75 ml of ammonia (25%, Merck) was added, the flask was shaken again and 2.5 ml of tetraethyl orthosilicate (TEOS, $\geq 98\%$, Fluka) was added to the mixture. After shaking again, the bottle was left to rest and the reaction was allowed to proceed overnight. Next, the reaction mixture was centrifuged at 1500 g for 1 hour. The supernatant was removed and the particles in the sediment were redispersed in ethanol. This centrifugation procedure was repeated at 1500 g for 15 minutes, 2 times with ethanol, 2 times with water and finally again with ethanol.

To remove small rods and improve monodispersity, the rods were centrifuged three times at 700 g for 15 minutes. The supernatant, which was still turbid at this point was removed and the rods in the sediment were redispersed in fresh ethanol. Large rods and aggregates were removed from the sample by sedimentation in ethanol. After the particles had sedimented for several hours, the clear supernatant was removed and maximally the same volume of the upper part of the sediment was used for further experiments. The remaining particles were redispersed and the procedure was repeated several times to obtain a sufficient amount of rods.

2.2.2. Characterization

Particle size distributions were determined by transmission electron microscopy (TEM), using a Technai 10 and 12 electron microscope (FEI company). The average length $\langle L \rangle$ and diameter $\langle D \rangle$ of the rods, as well as their standard deviation δ , were measured using iTEM 5.0 imaging software. The polydispersity is defined as $\sigma_L = \delta_L / \langle L \rangle$. For each sample 50 to 100 particles were measured.

The refractive index of the particles was measured using oils of varying refractive index (using steps of 0.01, Cargille refractive index liquids, measured at 589.3 nm at

25°C). Observation with an optical microscope allowed us to determine whether the refractive index of the particles was higher or lower than that of the oil.

The density of the particles was measured using a mixture of bromoform and methanol. Centrifugation at 700 *g* for 15 minutes showed whether rods in such a mixture creamed or sedimented. The composition of the mixture between creaming and sedimentation was converted to a density using Fig. 1 from [51].

Thermo gravimetric analysis (TGA) was performed in ambient air using a Pyris 1 machine of Perkin Elmer. The temperature was raised from 30°C to 900°C at rate of 10°C/min. At 150°C a drying step of 30 minutes was inserted. The sample stayed at 900°C for one minute. The samples that were measured were prepared as follows. A dispersion of silica particles in ethanol was centrifuged, after which the supernatant was removed as much as possible. Then the particles were dried for one night at 50°C.

N₂-adsorption measurements were performed at -196°C using a Micromeritics Tristar 3000. Before the measurement, the particles were dried at 300°C.

Elemental analysis was performed by Mikroanalytisches Laboratorium Kolbe in Germany. For carbon (C), nitrogen (N) and hydrogen(H), combustion analysis was performed by a CHNOS-analyzer. Silicon (Si) was measured with inductive coupled plasma (ICP) analysis.

²⁹Si solid state nuclear magnetic resonance (NMR) measurements were performed in the Institute for Molecules and Materials, Department of Physical Chemistry / Solid-state NMR at the Radboud University, Nijmegen. Spectra were recorded with 1H-decoupling, 8 kHz magic angle spinning (MAS) and a 600 MHz magnet. No cross polarization was used, to obtain quantitative results. Pulse delays of 1000 s were used. For the sample of Stöber silica spheres 90 scans were averaged, for the rods 173.

2.3. RESULTS AND DISCUSSION

The synthesis of silica rods is a simple one-pot procedure. Ethanol, water, sodium citrate and ammonia are added to a solution of PVP in pentanol, after which an emulsion of water in pentanol is formed. Upon the addition of TEOS, silica rods start to grow. Typical systems are shown in Fig. 2.1. One peculiar aspect of the rods is that one end is flat, while the other end is rounded, i.e. the rods are bullet shaped. The rods generally have a diameter around 200 to 300 nm and a variable length. The polydispersity of the system can be brought down to 6% in length and 12% in diameter.

2.3.1. Growth mechanism

Although the synthesis procedure is simple, there is no straightforward explanation for the growth of anisotropic structures of amorphous silica. Zhang *et al.* proposed a templated growth, where PVP molecules form complexes with gold particles and act as soft templates. However, we found that it is not the gold nanoparticles that induce

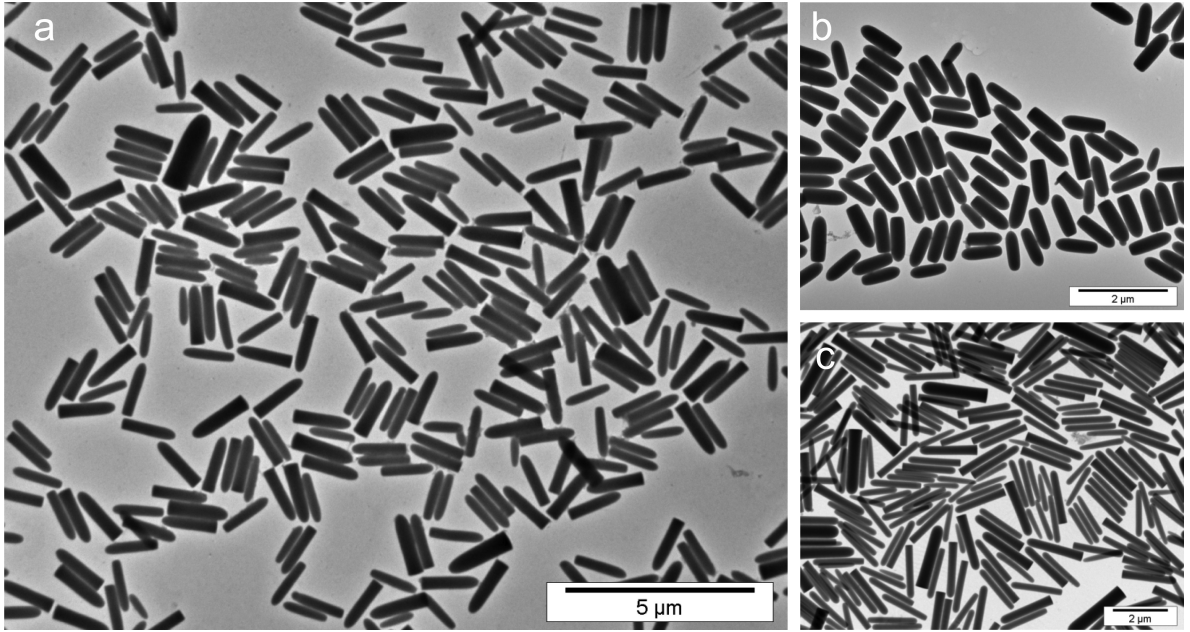


FIGURE 2.1. Transmission electron microscopy (TEM) images of typical systems after synthesis. (a) $L = 1.4 \mu\text{m}$ and $D = 280 \text{ nm}$ ($L/D = 5$, $\sigma_L = 6\%$, $\sigma_D = 14\%$). (b) $L = 1.0 \mu\text{m}$ and $D = 351 \text{ nm}$ ($L/D = 2.9$, $\sigma_L = 6\%$, $\sigma_D = 10\%$). (c) $L = 1.85 \mu\text{m}$ and $D = 237 \text{ nm}$ ($L/D = 7.8$, $\sigma_L = 9\%$, $\sigma_D = 8\%$).

rod formation, but the presence of sodium citrate that was used to stabilize the gold particles. The growth mechanism we propose is reminiscent of the vapor-liquid-solid method, where nanowires of several materials grow from metal droplets [52].

Figure 2.2 summarizes the growth mechanism; the first step involved the formation of droplets (Fig. 2.2a). Although pentanol, PVP, ethanol and water mix well for the volume ratios used in this synthesis (no phase separation was observed), a white turbid mixture is formed upon the addition of sodium citrate: an emulsion of water in pentanol stabilized by sodium citrate and PVP. It is striking that this emulsion is stable without a surfactant; addition of a common nonionic surfactant (Igepal CO-520, up to 0.8 g per 10 ml pentanol) did not have any noticeable effect on the resulting emulsion or rod growth. The presence of emulsion droplets was confirmed by dynamic light scattering measurements on the synthesis mixture containing all reagents except TEOS, where particles with a hydrodynamic radius of 100 nm were found. The diameter of the droplets corresponds to the diameter of the rods after synthesis. The fact that these droplets are visible in the vacuum environment of the electron microscope (Fig. 2.2a-c) suggests that they are not composed of water only, but probably contain a high concentration of PVP, which is imaged in the noncryo images. The assumption that the water droplets contain a high concentration of PVP is supported by the observation that when water was added to a solution of PVP in pentanol (water/pentanol = 1:1), the viscosity of the pentanol phase decreased, while the viscosity of the water phase

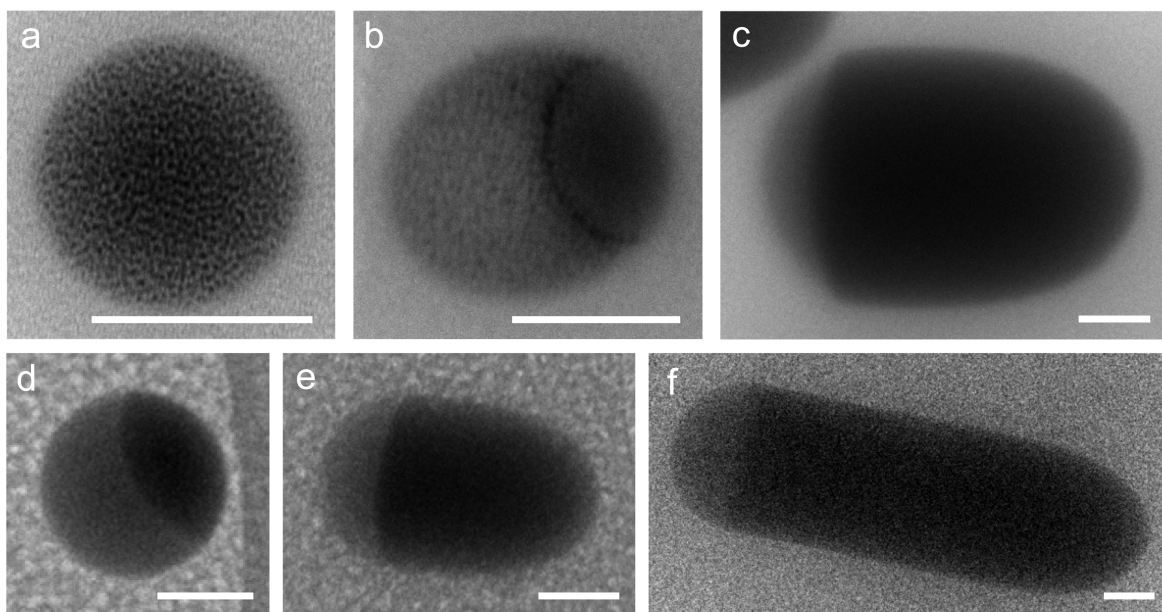


FIGURE 2.2. (a)-(c) TEM images of rods during growth after respectively 0, 30 and 180 minutes. (d)-(f) Cryo-TEM images of rods in a different run after 30, 60 and 120 minutes, respectively. Scale bars indicate 100 nm.

increased. This indicates that PVP moved from the pentanol to the water phase. Cryo-TEM images show that the shape and size of the droplet, this time also containing water, was not significantly different from the dried ‘droplets’ (Fig.2.2d-f).

The second step in the growth mechanism is initiated by the addition of the silica precursor TEOS. TEOS reacts to silica via a hydrolysis reaction followed by condensation. While TEOS itself dissolves well in pentanol, its hydrolyzed form is hydrophilic and will therefore move towards the water-rich emulsion droplets. The growing silica nucleus was found to be positioned at the surface of the emulsion droplets, as follows from Fig 2.2b. Subsequently, hydrolyzed TEOS is only supplied from within the droplet and grows onto the existing nucleus rather than nucleating elsewhere. Because only one side of the nucleus faces the water droplet, the supply of fresh TEOS to the nucleus is one-sided, and the nucleus grows in one direction only (Fig. 2.2c) while the droplet stays attached to one end. Surface tension keeps the angle between the growing silica rod and the emulsion droplet constant, resulting in a nearly constant rod diameter and a rapidly increasing length (Fig. 2.3). When all TEOS has reacted to silica, the growth stops. Figure 2.3 shows that this happens after approximately 17 hours of reaction time. The transition from linear to non-linear growth after 4 hours is caused by a transition from reaction to diffusion limited growth, since unreacted TEOS is not abundantly present anymore. The emulsion droplet that is still attached to the rod’s end at the end of the reaction can be washed away, after which a flat rod end remains. Note that this growth mechanism is quite different from that of Stöber silica growth, which takes place in

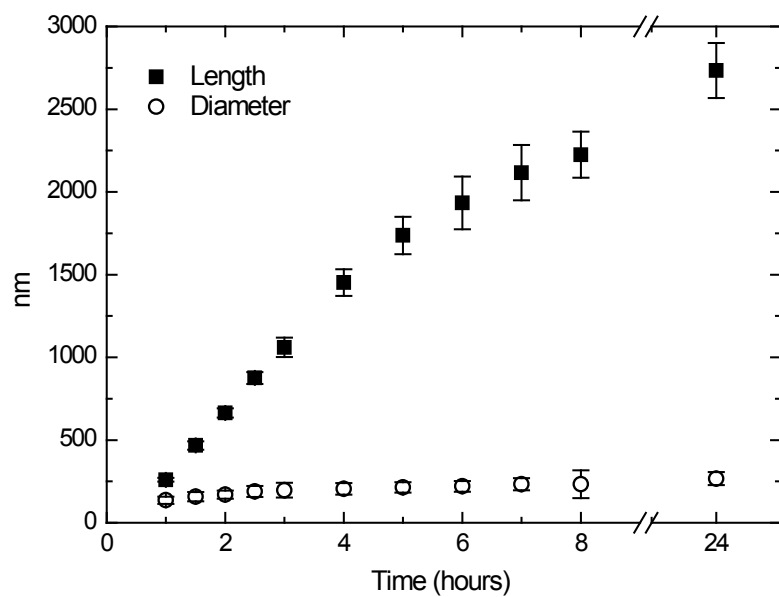


FIGURE 2.3. Length and diameter of the rods during growth. The growth rate in length is significantly higher than the growth rate in diameter.

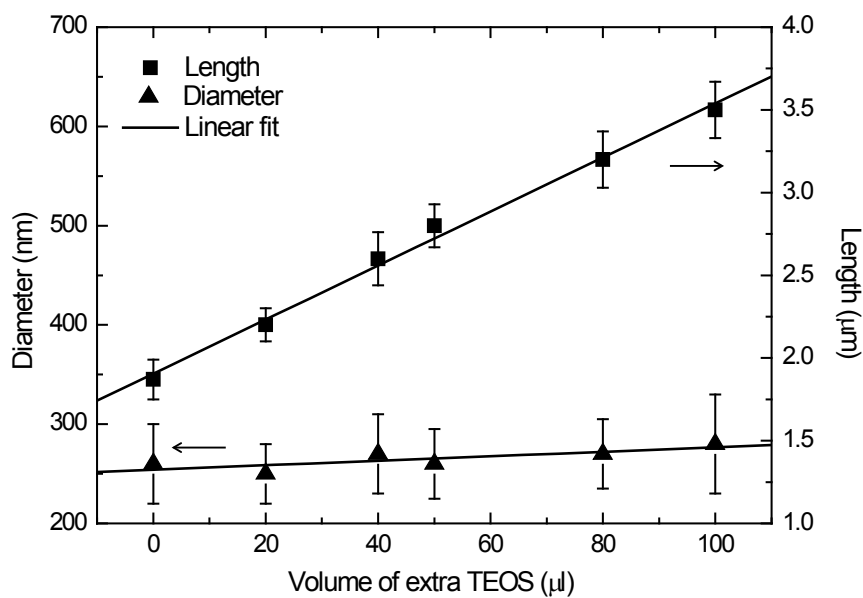


FIGURE 2.4. Addition of extra TEOS during synthesis leads to an increase in rod aspect ratio. Shown is the dependence of length (squares) and diameter (triangles) on the volume of extra added TEOS.

ethanol-water-ammonia mixtures and where the growth is proportional to the surface area [53, 54]. In this case, however, the limiting step is the hydrolysis of TEOS.

2.3.2. Control over rod-size and aspect ratio

While the diameter of the rods is fixed by the size of the emulsion droplets, the length and aspect ratio of the rods can be controlled via three different routes: reagent concentrations, seeded growth or the growth of shells.

Alterations in reaction conditions such as temperature and reagent concentrations hardly affected the thickness of the rods, while they highly affected the length and shape. Generally, changed reaction conditions had two possible consequences: either the particles turned out to be longer and eventually curly, or shorter until they became spherical. The different shapes will be discussed in the next section; here we focus on the rod-regime. The range of reagent concentrations that can be used to make rods is shown in Fig. 2.5. Within this range, longer particles could be obtained by lowering the water or ammonia concentration. Also, changing solvent to a shorter chain alcohol, adding more ethanol, or increasing the reaction temperature led to longer rods. For shorter particles the opposite of the previously mentioned alterations was found to be applicable.

A seeded growth procedure, involving the addition of extra TEOS to the synthesis mixture, allowed for growth in length as long as the emulsion droplet was still attached to the rod. This way, the length of the rod could be increased even after the initial synthesis was finished. The volume of extra TEOS that could be added at once was maximally the initial volume used for rod formation and could be added from 6 hours after addition of the initial amount. Figure 2.4 shows that the length of the rods grew linearly with the added amount of TEOS. The diameter of the rods increased only slightly upon extra TEOS addition. Addition of more than the initial volume of TEOS at once led to unstable rod growth resulting in curly rod-ends. Multiple growth steps were possible and lengths up to 10 μm were achieved, which extended the achievable aspect ratio to ~ 25 . Besides the increase in length of the rods, the second TEOS-addition step also increased the yield from $\sim 25\%$ for a 1-step synthesis to $\sim 45\%$ for 2-step synthesis. This was caused by the fact that only the long, stable rods grew further and small rods were removed by centrifugation. Since the number of stable rods decreased with every growth step, the extremely long rods of 10 μm were produced in very low quantities (yields less than 1%).

Finally, it is possible to tune the aspect ratio of the rods by growing extra layers of silica around them using standard seeded Stöber or Giesche growth [53–55]. With this method, the length as well as the diameter was increased, which made it (together with seeded growth) a perfect tool to tune the aspect ratio of existing rods. Additionally, the growth of extra layers of silica decreased the polydispersity of the rods significantly.

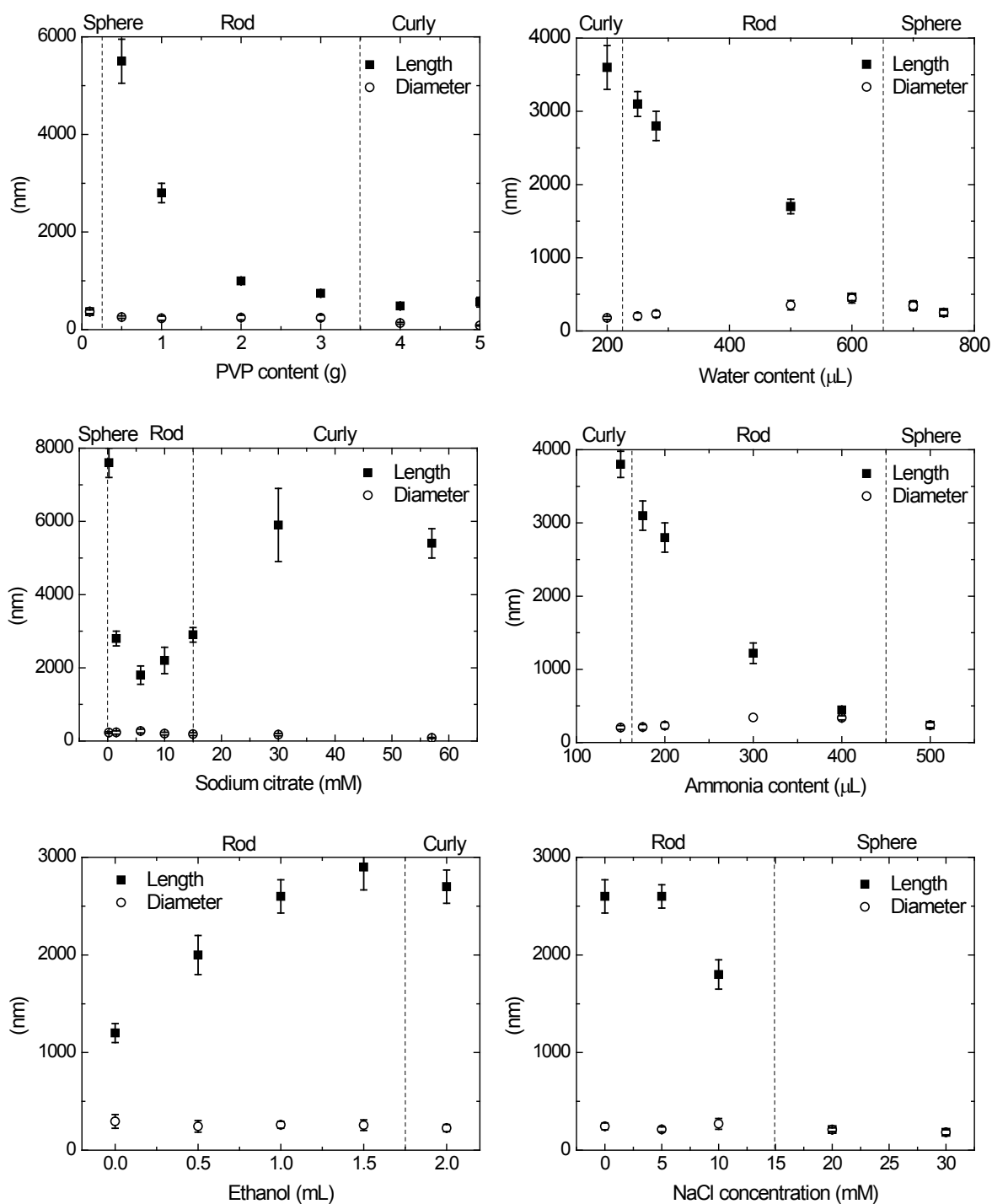


FIGURE 2.5. Graphs showing the dependence of length and diameter on reagent concentrations. Depending on several concentrations, the resulting particles can be spheres, straight rods, or curly rods (see also Fig. 2.6). The standard concentrations were: 10 ml pentanol, 1 g PVP, 1 ml ethanol, 0.28 ml water, 0.225 ml ammonia, 0.1 ml 0.18 M sodiumcitrate solution and 0.1 ml TEOS.

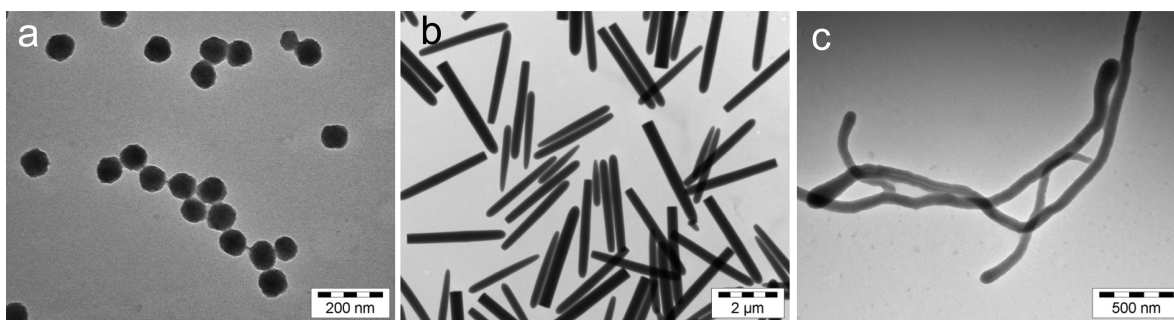


FIGURE 2.6. Depending on reagent concentration, particles become spherical (a), rod-like (b), or curly (c). The corresponding concentrations can be found in Fig. 2.5.

Especially the polydispersity in diameter can be decreased from $\sim 15\%$ to less than 10% . This is in accordance with the expectations of a reaction mechanism as given in reference [54], where each particle grows the same amount, thus reducing polydispersity with $1/R$. For a rod with a mean diameter of 300 nm that typically grows to $500\text{--}600\text{ nm}$, this would mean a reduction of the polydispersity from $\sim 15\%$ to $10\text{--}7.5\%$.

2.3.3. Discussion of several reaction conditions and resulting rod-shapes

As mentioned in the previous section, three different particle shapes were observed depending on reagent concentrations: spheres, rods and curly structures (Fig. 2.6). Solid spheres were found at low PVP concentration, high water or ammonia concentration and high salt (NaCl) concentration. Also, spheres were formed when no sodium citrate was added. As explained in Section 2.3.1, PVP and sodium citrate are key reagents for rod formation. In the absence of either one of them, there was no droplet formation and consequently silica particles grew via the ‘normal’ nucleation-and-growth model, which resulted in spheres. However, we found that it is possible to replace sodium citrate by sodium phosphate or tartrate to stabilize the emulsion droplets, although at slightly different concentrations. It is not clear what exactly happened at high water, ammonia or salt concentrations that caused sphere formation.

At the other side of the rod regime in Fig. 2.5, we found curly structures. These were formed at low water and ammonia concentration, or at high ethanol, sodium citrate and PVP concentrations. Most likely, the curliness of the rods resulted from the changed reaction conditions that disturbed the process in such a way that surface tension was no longer able to keep the angle between the emulsion droplet and the growing silica rod constant during growth.

Apart from reagent concentrations, the solvent in which the reaction occurs also influenced shape and size. Figure 2.7 shows particles that were grown in different alcohols, ranging from ethanol to octanol. Water dissolves well in short alcohols, such as ethanol and propanol. However, in presence of sodium citrate and PVP, even in

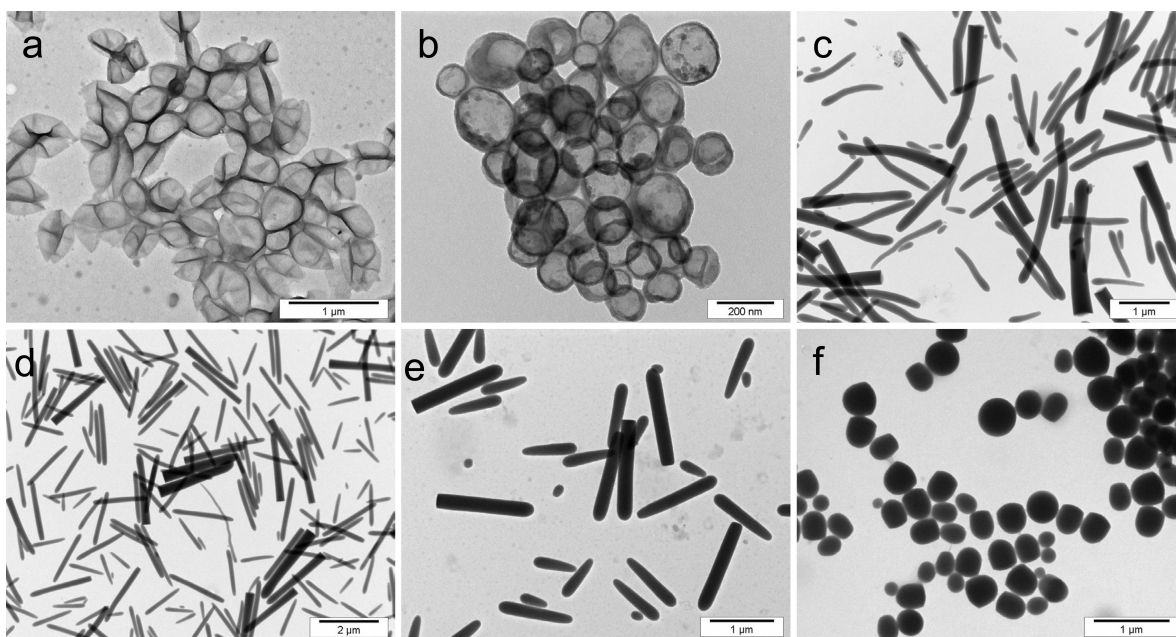


FIGURE 2.7. When different alcohols are used as a solvent during synthesis, different shapes of particles result. (a) ethanol. (b) propanol. (c) butanol. (d) pentanol. (e) hexanol. (f) octanol.

these solvents an emulsion was formed. Even though emulsion droplets were formed, the hydrolyzed TEOS did not show a strong preference for the water phase in this case. Therefore, it did not rapidly diffuse into the water droplets, but condensed on the surface of the droplets, which resulted in the hollow spheres shown in Fig. 2.7a-b. With increasing chain length, the alcohols become more hydrophobic and hence the hydrolyzed TEOS obtained a stronger preference for the water droplets and diffused into the droplets faster. New silica therefore grew from within the droplets rather than on their entire surface. This resulted in curly to bent rods when butanol was used, and straight rods in the case of pentanol and hexanol. In the case of octanol, the rods became so short that we expect longer alcohols to result in sphere formation.

Another factor that influences the shape of the rods is stirring. Straight rods were best grown without any stirring. When the mixture was stirred magnetically in a round bottom flask, though, two different types of rods were found, as shown in Fig. 2.8. These shapes were caused by two different phenomena. First, stirring caused instabilities that allowed salt to crystallize from the emulsion droplets. This resulted in long needles with rods sticking out of the emulsion droplets and connecting with other droplets (Fig. 2.8a). Regarding the reagents in our synthesis mixture and the work done by Wang *et al.* [56], we assume these were ammonium citrate crystals, probably coated with a thin layer of silica. Second, stirring induced a shear-flow in the synthesis mixture. At the start of rod-growth, this did not cause problems, but when the rods reached a certain length the shear affected the rod-growth in such a way that the droplet at the end of the rod

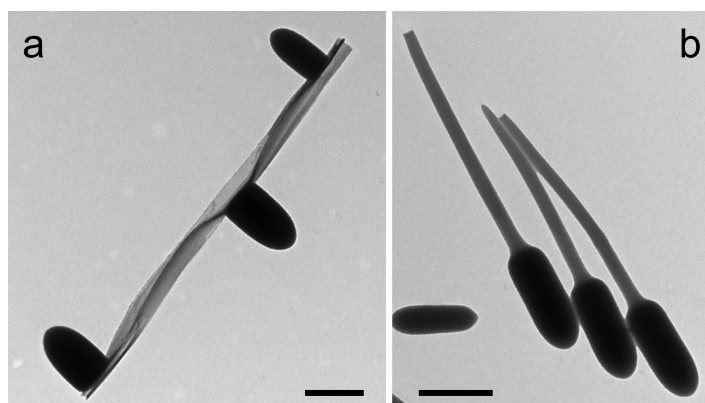


FIGURE 2.8. Peculiarly shaped particles due to instabilities induced by stirring. (a) rods, shaped like thorn branches, grown on ammonium citrate crystals. (b) rods with thin tails (bulrushes) due to instabilities of the droplet that was attached to the end of the rod during growth. Scalebars indicate 500 nm.

became unstable and shrunk, after which the rod grew further with a smaller diameter (Fig. 2.8b). Although stirring had a negative effect during the growth of the rods, the way of mixing the reagents at the start of the reaction did not matter at all. Sonication, shaking and stirring did not influence the size or polydispersity of the emulsion droplets and the resulting rod diameter. Also, the addition of a surfactant (Igepal CO-520, up to 0.8 g per 10 ml pentanol) did not have any effect on the resulting emulsion or rod-growth.

Finally, we found particles that were shaped like a rod with a (hollow) sphere attached to its round end, as shown in Fig. 2.9c. Figure 2.9 also shows that the hollow sphere part of these particles was formed first during synthesis, after which the rod growth started. These particles were fabricated only with one specific (several years old) bottle of TEOS. We hypothesize that the TEOS in this bottle was partly hydrolyzed. Since the TEOS did not need to be hydrolyzed in the water droplets anymore, it condensed very fast when it reached the emulsion droplets in which the concentration of the catalyst ammonia is higher than in the pentanol. Consequently, a shell of silica was formed around the emulsion droplet instead of the usual cap. The water-droplet, or part of it, was subsequently pushed out after which the growth continued similarly to normal rod growth. However, we did not find any direct evidence to support this model for the growth of these particles. The hypothesis that prehydrolyzed TEOS is involved is supported by the result shown in Fig. 2.9d. Using fresh TEOS that was prehydrolyzed by letting it react with water in a volume ratio of 1/2.8 for 1 night before addition to the synthesis mixture resulted in rods with a hollow sphere attached, but not as regularly as with the old bottle of TEOS (compare Fig. 2.9c and d).

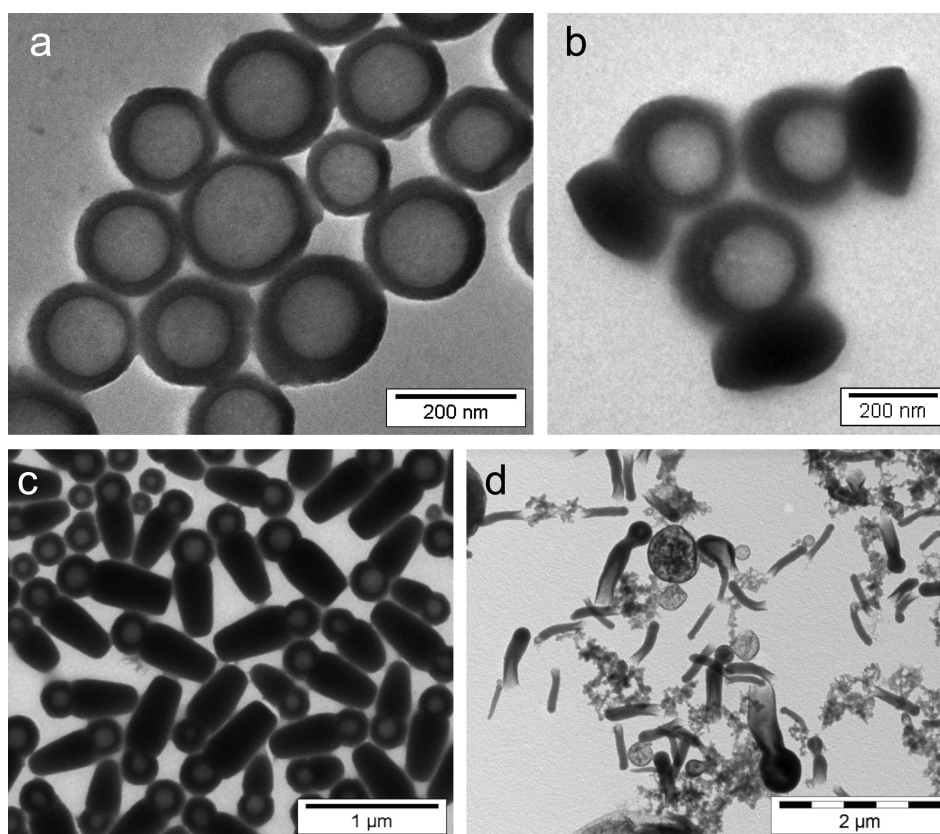


FIGURE 2.9. Rods with a hollow sphere attached. (a) 30 min after start of synthesis. (b) 60 min after start. (c) Final result. (d) Rods prepared with fresh TEOS that was prehydrolyzed.

2.3.4. Material properties of silica rods versus spherical Stöber silica

Spherical silica particles have been used in colloid science since Stöber, Fink and Bohn reported their synthesis of monodisperse spherical colloids in 1968 [53]. We compared the material properties of this so-called Stöber silica with those of the silica rods. The Stöber silica spheres that were used to this end had a diameter of 606 nm and a polydispersity of 10%. The spheres were synthesized in a mixture of 713 g of ethanol, 109.3 g of ammonia and 35.54 ml of TEOS.

Properties that are of direct interest for future use in confocal microscopy studies are the index of refraction and density. Table 2.1 shows that the index of refraction of the rods does not differ significantly from that of Stöber silica: both around 1.45. The density however, is slightly lower for the rods, which suggests a more porous structure.

More information about the porosity of the structure was obtained by N_2 -adsorption measurements of particles first dried at 300°C , at which all water is evaporated from the particles' pores. This was done for rods of $L = 1.6 \mu\text{m}$ and $D = 310 \text{ nm}$. The results showed that the BET-surface area (Brunauer-Emmett-Teller) of the spheres was much smaller ($6.1 \text{ m}^2/\text{g}$) than that of the rods ($47.7 \text{ m}^2/\text{g}$). The actual geometrical surface

System	L (μm)	D (nm)	L/D	ρ (g/ml)	n
B17	0.76	407	1.8	1.90 ± 0.04	
B11	1.1	270	4.1	1.90 ± 0.03	1.455 ± 0.005
B22	1.6	335	4.8	1.89 ± 0.03	
B23	2.1	252	8.4	1.89 ± 0.02	1.445 ± 0.005
Stöber silica	-	606	1	1.99 ± 0.01	1.445 ± 0.005

TABLE 2.1. Density (ρ) and refractive index (n) of several systems of rods and Stöber silica spheres.

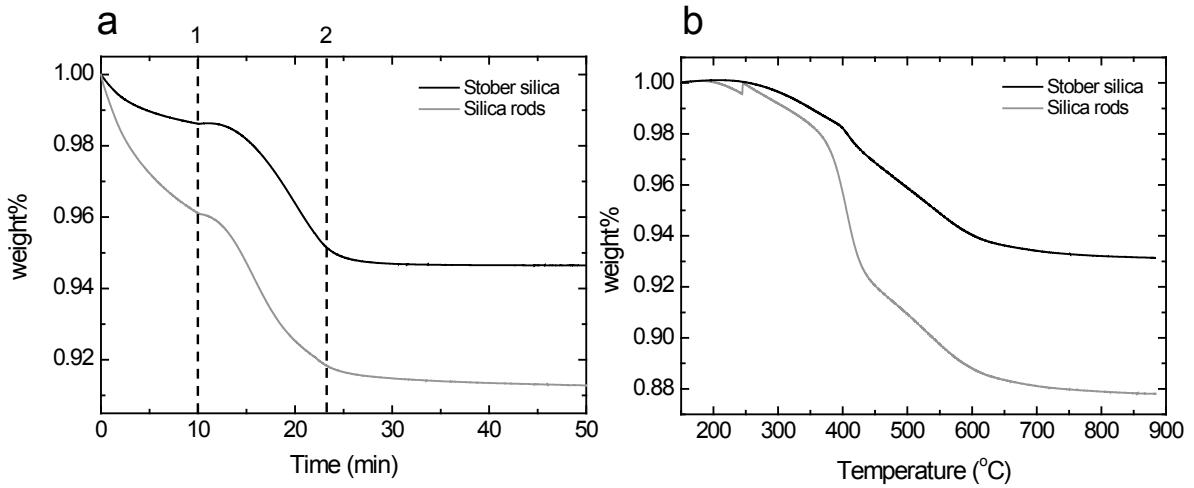


FIGURE 2.10. Thermo gravimetric analysis of silica rods and spheres. (a) Drying step before TGA measurement; the Stöber silica spheres contain less water than the silica rods. (1: heating from 30°C to 150°C , 2: constant temperature of 150°C). (b) TGA measurement after drying step. The temperature was increased with 10°C per minute. The rods lose more weight than the spheres.

areas of the spheres and rods are $5.0 \text{ m}^2/\text{g}$ and $8.0 \text{ m}^2/\text{g}$, respectively. This means that 18% of the measured BET-surface area of spheres stems from internal pores, while this value is 83% for the rods. The rods thus have a more porous structure than the spheres. This was confirmed by the determination of pore volumes for pore diameters between 1 and 300 nm: a significantly larger pore-volume was measured for the rods (0.034 ± 0.003 versus $0.013 \pm 0.001 \text{ cm}^3/\text{g}$). In summary, we can conclude that the rods are more porous than Stöber silica.

System	C(%)	H (%)	N (%)	Si (%)
rods	3.48	1.20	0.68	38.96
spheres	1.12	0.91	0.01	44.08

TABLE 2.2. Elemental analysis results in weight percentages.

The higher porosity of the rods compared to Stöber silica can be explained by the presence of PVP in the structure. This hypothesis is supported by the observation that the rods looked brownish white after heating to 300°C for the N₂-adsorption measurement, which indicates that something was burned: probably PVP. Thermogravimetric analysis (TGA) confirmed this observation; the rods decreased more in weight than the Stöber silica: 12% versus 7% (Fig. 2.10b). The temperature of around 400°C at which the additional decrease for rods occurs is the temperature at which PVP burns (see for instance [57]).

Elemental analysis was used to obtain more direct proof of PVP inside the rods. Elemental analysis was done for carbon, hydrogen, nitrogen and silicon. The results are listed in Table 2.2. The presence of N-atoms in the rods is an indication for PVP-molecules, which is the only species in the synthesis that contains nitrogen apart from the (gaseous) catalyst ammonia. From the measurements for Stöber silica we know that ammonia does not stay inside the silica structure, as there were no N-atoms detected for the spheres. The molecular formula of PVP is (C₆H₉NO)_m, with *m* the number of monomers. For the found weight percentage of 0.68% for N in the rods, a corresponding weight-percentage of 0.44 for H, 0.78 for O and 3.50 for C is thus expected due to PVP molecules. This suggests that all carbon in the rods stems from PVP-molecules. The total weight percentage of PVP calculated from the elemental analysis results is 5.4%, which corresponds well to the value of 5% found in the TGA measurement. Furthermore, the amount of PVP-molecules per surface area can be calculated using these data. Assuming all PVP is adsorbed on the surface of the rods, we found an amount of 7.4 mg/m². Compared with the maximum adsorption of 0.8 mg/m² for PVP25 (molecular weight 25000 g/mol) on silica that was found by Van der Beek *et al.* [58], this seems to be too high. It is therefore more likely that the PVP was also built in the internal structure of the rods, causing the higher porosity.

The water content of the rods was measured in drying steps before the TGA and elemental analysis (Fig. 2.10a). The rods were dried at 150°C for 30 minutes for the TGA measurements and at 100°C for 1 night for the elemental analysis. After drying, the rods had lost on average 8.7% of their weight and the spheres 4.7%. The rods thus contained more water than the spherical colloids, as was expected due to the higher porosity of the rods.

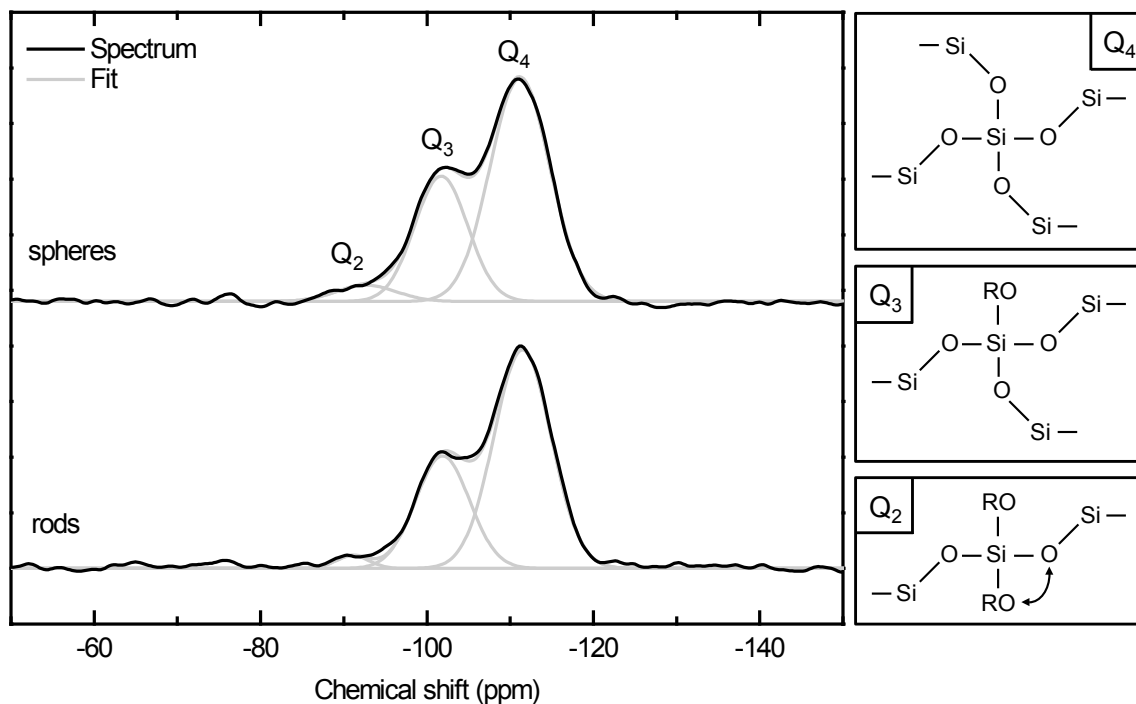


FIGURE 2.11. ^{29}Si solid-state NMR spectra (black) of silica rods and Stöber silica spheres. Q_4 , Q_3 and Q_2 are silicon atoms bonded with four, three or two other silicon atoms via an oxygen atom. Exact positions and relative heights were determined by fitting Gaussian functions (grey) to the spectra, see Table 2.3.

System	Site	Position (ppm)	T_1 (s)	I_R
spheres	Q_2	-92.7		4.8%
	Q_3	-101.7	113	32.5%
	Q_4	-111.2	129	62.7%
rods	Q_2	-91.0		1.6%
	Q_3	-101.9	135	35.8%
	Q_4	-111.5	67	62.6%

TABLE 2.3. Positions, delay times (T_1) and relative intensities (I_R) of the peaks in the ^{29}Si solid-state NMR spectra shown in Fig. 2.11.

Although the structure of the rods is more porous than that of the spheres, their chemical structure is similar. Using ^{29}Si solid-state NMR, the atomic surrounding of the silicon atoms in the structure was determined. The resulting spectra are shown in Fig. 2.11. Chemical shifts are given in parts per million (ppm), relative to tetramethylsilane. The three peaks in these spectra correspond to silicon atoms with 4 (Q_4), 3 (Q_3) or 2 (Q_2) O-Si bonds. The other groups around the silicon atom are ethoxy or hydroxy groups. Quantitative ^{29}Si solid-state NMR measurements showed that the silica which the rods and spheres are made of both consist of about 62% of Q_4 , 35% of Q_3 and a few percent of Q_2 (Table 2.3), which is consistent with earlier measurements for colloidal silica [59].

2.4. CONCLUSIONS

We developed a new anisotropic monodisperse colloidal model system that is tunable in length and aspect ratio. The growth mechanism of the rods involves emulsion droplets of water and PVP in pentanol inside which silica condensation takes place. Due to the positioning of the nucleus at the emulsion droplet's wall and the consequent anisotropic supply of reactants, the nucleus grows to one side only, which surprisingly results in rod formation. The growth mechanism even allows for a seeded growth procedure using the original water/PVP droplet for further growth. Hereby, the amount of TEOS that is added determines the length of the rods. This way, aspect ratios up to 25 were obtained. Other techniques to control rod-length and diameter include carefully chosen reagent concentrations and the growth of shells.

Disturbance of the reaction conditions influenced the shape of the rods in different ways. As a result, particles were observed with shapes ranging from spherical to rod-like to curly snake-like. Also, we found particles shaped like thorn branches and bulrushes, and even rods with a hollow sphere attached to one end with a high yield and purity, but for now difficult to exactly pinpoint reaction conditions.

The properties of our silica rods were compared to those of Stöber silica spheres. It was found that the refractive index of rods and spheres is equal (1.45 ± 0.005), while the density of rods is slightly lower than that of spheres (1.9 g/cm^3). Furthermore, the porosity of the rods was higher than that of the spheres. Elemental analysis showed that this is most likely caused by the presence of about 5% by weight of PVP-molecules inside the silica matrix of the rods. Despite their more open structure, the chemical structure of the silica that the rods and spheres consist of was equal within error. They consist of a not fully condensed siloxane structure, of which 62% is Q_4 , 35% is Q_3 and a few percent is Q_2 .

2.5. ACKNOWLEDGEMENTS

We would like to acknowledge Hans Meeldijk for performing the Cryo-TEM measurements. We are also grateful to Arjen van de Glind for useful discussions about the TGA and N₂-adsorption measurements. Also, we wish to thank Johan Stiefelhagen for the synthesis of the Stöber silica spheres and for all sorts of advise on syntheses and lab-work. Finally, Margriet Verkuijlen is acknowledged for performing the solid state NMR measurements.

3

Preparation of silica rods for quantitative 3D confocal laser scanning microscopy

ABSTRACT

Silica rods were made suitable for quantitative real-space studies by ‘conventional’ confocal laser scanning microscopy. We present and discuss several methods of fluorescent labeling to prepare rods with different fluorescent patterning, ranging from constant fluorescence levels to gradients from one rod-end to the other, and even patterns of two colors. Single particle imaging was achieved by creating core-shell rods that had a fluorescent core and a non-fluorescent shell. Alternatively, the rods could be coated with 3-(trimethoxysilyl)propyl methacrylate or octadecyltrimethoxysilane and dispersed in a solvent with a low dielectric constant to induce micron-sized double layers. To enable quantitative measurements, a tracking algorithm was developed that identifies the rods’ positions and orientations in 2D optical slices. Initial testing of the method showed that projected 2D orientational order parameters can be used to assess the 3D orientational order parameter in both dilute and strongly interacting systems.

3.1. INTRODUCTION

Confocal laser scanning microscopy (CLSM) is a technique that is frequently used in colloid science to obtain quantitative information in 3D and real space about the structure and dynamics of colloidal systems with single particle resolution [60–62]. In recent years, CLSM has been applied to study a varied range of colloidal phenomena [63], for instance nucleation and growth of colloidal crystals [64, 65], and shear induced formation and melting of crystals [66, 67]. However, most advances in understanding the properties of colloidal materials by CLSM have been made for systems of spherical particles, mainly due to the scarcity of model materials suitable for experimental studies of anisotropic colloids. To our knowledge, only a few anisotropic experimental systems have been used in confocal microscopy studies, e.g. poly(methyl methacrylate) (PMMA) ellipsoids obtained by stretching spheres, and dumbbell shaped particles made from fluorescent core-shell particles of silica [24, 47–49]. The aspect ratio for dumbbells is not large enough to expect liquid crystal phases, contrary to the PMMA ellipsoids. To this date, however, only isotropic and nematic liquid crystal phases were observed for this system and no smectic phases. Our system of silica rods, which forms isotropic, nematic and smectic phases, offers therefore interesting new possibilities for real-space studies of anisotropic colloids on the single particle level.

In this chapter, we describe the adaptations that are necessary to make our silica rods suitable for quantitative 3D real-space analysis by confocal microscopy. Three different approaches are presented to prepare fluorescently labeled silica rods. The resulting particles each have their own characteristic fluorescent pattern. After describing the different methods that were explored to enable single particle imaging in CLSM experiments, preliminary results of the determining rod-position and orientation are discussed as well.

3.1.1. Confocal microscopy

The confocal microscope was developed by Marvin Minsky in the 1950s to improve the imaging of biological systems by conventional optical microscopy [63, 68, 69]. In optically dense samples, such as biological tissues or concentrated colloidal dispersions, light coming from planes that are not in focus contribute to the image and wash out details from the focal plane, which results in blurry images. The solution of Minsky to improve imaging was two-fold: first, he limited the excitation (or reflection) light to that of a diffraction limited point by using a pinhole in combination with a high intensity light source and a high aperture lens. Second, he rejected out-of-focus light by inserting a pinhole aperture in the conjugate focal plane (hence the name confocal) of the sample. Later, the technique was improved further by using a laser as a light source. A schematic overview of the operating principle of the confocal laser scanning microscope, illustrating the spatial filtering effect, is shown in Fig. 3.1a.

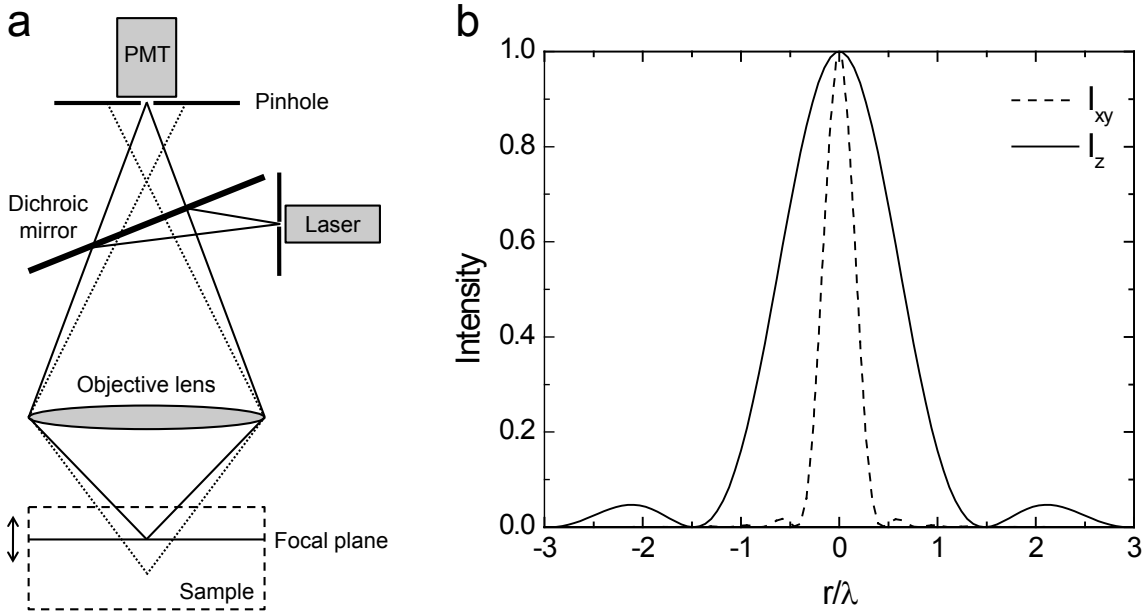


FIGURE 3.1. (a) Schematic overview of the operating principle of a confocal microscope. Laser light is directed by a dichroic mirror through the microscope objective and excites the fluorescent sample. The fluorescent light passes back through the objective and the dichroic mirror and reaches the photomultiplier tube (PMT) through a pinhole placed in the conjugate focal plane. (b) Point spread function perpendicular (I_{xy}) and parallel (I_z) to the optical axis. Intensity is shown as a function of distance r from the center, scaled with the wavelength λ of the laser source, for $n = 1.45$ and $NA = 1.4$.

2D images can be obtained by scanning point by point over a 2D plane. This can be realized by scanning the light beam (beam scanning) using e.g. a movable mirror, scanning the pinhole(s) or by moving the sample; all these techniques have been applied in confocal microscopes. The extension to imaging a 3D sample is made by moving the sample, or the focus, in the vertical direction as well. A 3D reconstruction of the sample can then be obtained by performing a series of 2D scans at different depths.

Compared to conventional microscopy, the use of both a point light source and point detector results in a 3D increase of resolution of about a factor 3 (see e.g. [63]). We are aware of the fact that the last few years several methods have been developed to significantly increase the resolution of both ‘conventional’ and confocal microscopy [70–72]. E.g. using so-called stimulated emission depletion confocal microscopy, a technique which reduces the point spread function using a doughnut shaped high intensity pulse, a 3D resolution well below 100 nm has been achieved using fluorescently labeled core-shell particles made in our lab [73]. Although quite exciting, these techniques were not used in this thesis and will therefore not be discussed.

The resolution of a confocal microscope is limited by diffraction of light. Since the particles are observed through a circular aperture, light gets diffracted and the intensity of single points in the sample is spread over larger areas in the resulting image. The amount of spreading is described by the point-spread function, which, in the focal plane, is given by the Airy function:

$$I_{xy}(v) = \left(\frac{2J_1(v)}{v} \right)^2 \quad (3.1)$$

where $J_1(v)$ is the first-order Bessel function, $v = 2\pi r NA/\lambda$ with λ the wavelength of the laser source, r the distance from the center point and NA the numerical aperture of the objective lens. A plot of this function is shown in Fig. 3.1b. The Airy function is strongly peaked around the center and the area within its first minimum is called the Airy disc. The maximum resolution of the microscope is determined by the size of the Airy disc, since two points should be separated by at least their Airy disc to be distinguishable (Rayleigh criterion). The size of the Airy disc is given by: $r = 0.61\lambda/NA$.

In the direction along the optical axis, perpendicular to the focal plane, the point-spread function is given by:

$$I_z(u) = \left(\frac{\sin\left(\frac{u}{4}\right)}{\frac{u}{4}} \right)^2 \quad (3.2)$$

with $u = 2\pi(NA)^2z/(\lambda n)$. Here, z is the distance along the optical axis and n the refractive index of the medium (1.45 for a refractive index matched silica system). In this case, the distance to the first minimum is $z = 2n\lambda/(NA)^2$. Figure 3.1b shows that the spread in z is much larger than that in the xy plane. Consequently, the resolution in z is also worse.

Filling in the numbers for our set-up, where $\lambda = 543$ or 488 nm, $NA = 1.4$ and $n = 1.45$, we find that the in-plane resolution is about 250 nm and the resolution along the optical axis about 750 nm (3 times less). Note, that resolution is not the same as the accuracy of determining where a particle is. There have not only been important improvements made in the resolution of confocal and other light microscopy methods, resulting in true light nanoscopy [72], but also position determination of particles and molecules is still increasing (see e.g. [74–76]).

3.1.2. Colloids for confocal microscopy

Since silica spheres have been used in CLSM studies for years, a lot of knowledge about the adaptation of the colloidal system for CLSM studies is available in literature. First, the refractive index of the particles and the solvent need to be matched to diminish scattering events that redirect fluorescent light and deteriorate the point spread function. For charge stabilized silica colloids this can be done by mixtures of dimethyl sulfoxide (DMSO) and water, or glycerol and water. Second, the rods need to be labeled with a fluorescent dye. Van Blaaderen *et al.* developed a method to label

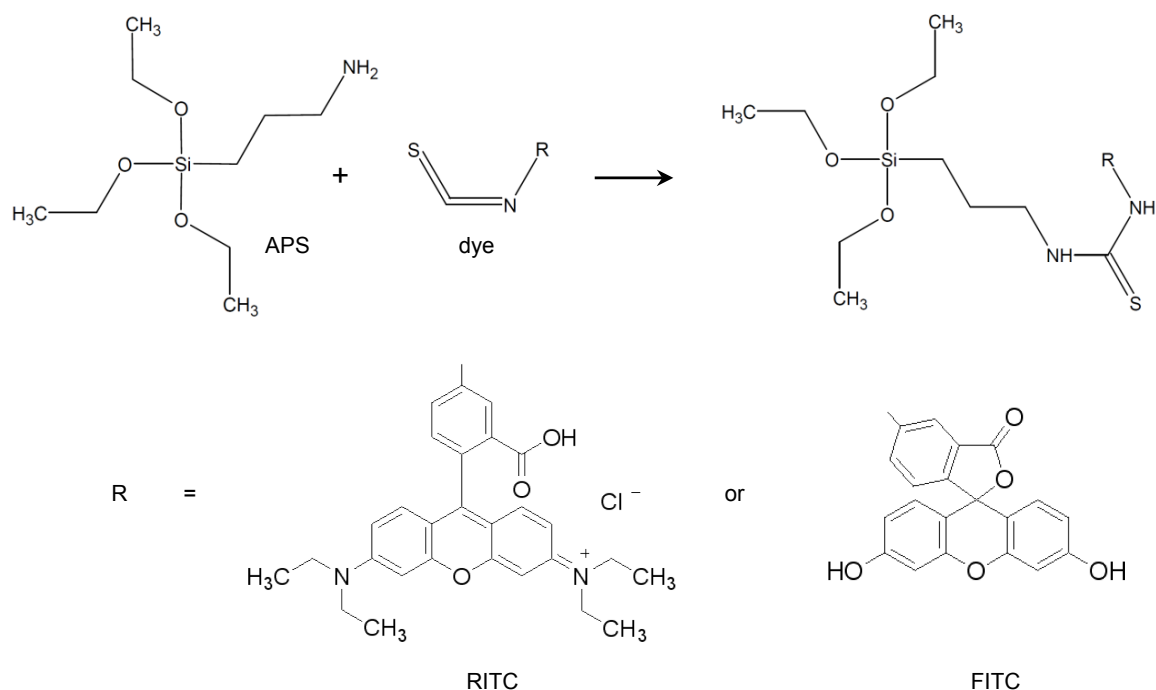


FIGURE 3.2. Top: reaction of APS with the isothiocyanate group of dye-molecules. Bottom: structure formulas of RITC and FITC.

spherical colloids with several fluorescent dyes, such as RITC and FITC [77, 78]. The dye-molecules were connected to a silane coupling agent, (3-aminopropyl)triethoxysilane (APS), so that a fluorescent molecule was formed with a structure similar to the silica precursor tetraethoxy silane (TEOS), but with one of the ethoxy groups replaced with an organic fluorescent group (Fig. 3.2). This way, covalent bonding of the dye-molecules to the silica-matrix was achieved, which resulted in homogeneously labeled spheres.

Fluorescent labeling alone, however, is often not enough to study colloidal rods on the single-particle level. The limited resolution of the microscope requires further processing of the rods. As described in the previous section, two neighboring rods need to be separated several hundreds of nanometers to achieve single particle imaging. For silica spheres this problem was solved by creating core-shell particles. These particles have a fluorescent core and a non-fluorescent shell to ensure sufficient spacing of the fluorescent parts.

3.2. EXPERIMENTAL

3.2.1. Fluorescent cores

Two different methods were used to prepare fluorescent rods. In the first method, fluorescent rods were prepared by adding a fluorescent dye that had already reacted with a coupling agent to the synthesis mixture. 25 mg (0.064 mmol) of fluorescein isothiocyanate (FITC, isomer I, $\geq 90\%$, Sigma) was dissolved in 5 ml of absolute

ethanol (Baker) by sonicating the mixture for a few minutes (Branson 2510 sonicator). After the addition of 35 μl (0.15 mmol) (3-aminopropyl)triethoxysilane (APS, $\geq 98\%$, Sigma-Aldrich), this mixture reacted overnight. Alternatively, 35 mg (0.065 mmol) of rhodamine isothiocyanate (RITC, mixed isomers, Aldrich) was added in stead of 25 mg of FITC. The molar ratio of dye:APS was in both cases 1:2.3, which is about the same as mentioned in literature for fluorescent spheres (1:1.9 in [77, 78]).

Rods with an average length L of 2.1 μm and an average diameter D of 300 nm were grown as described in Chapter 2, with a slightly increased water concentration. In this synthesis we used 300 ml of 1-pentanol ($\geq 99\%$, Sigma-Aldrich), 30 g of polyvinylpyrrolidone (PVP, average molecular weight $M_n = 40.000$, Sigma-Aldrich), 30 ml of ethanol, 9 ml of ultrapure water (Millipore system), 6.7 ml of ammonia (25%, Merck), 2.0 ml of 0.18 M sodium citrate (99%, Aldrich) in water, and 3.0 ml of tetraethyl orthosilicate (TEOS, $\geq 98\%$, Fluka). Directly after the addition of TEOS, the FITC/APS mixture in ethanol was added to the synthesis mixture. The mixture was left to react overnight and was then cleaned as described in Chapter 2. The molar ratio of APS:TEOS in the synthesis mixture was 1:90, which is 3 times higher than the ratio that is often used for fluorescent spheres (1:285 in [77]).

A second method to obtain fluorescent rods involved the addition of uncoupled APS to the synthesis mixture before formation of the rods. In this case, 300 ml of pentanol, 30 g of PVP, 20 ml of ethanol, 11 ml of water, 6.7 ml of ammonia, and 2.0 ml of 0.18 M sodium citrate in water were used. In stead of 3.0 ml of TEOS, a mixture of 3.0 ml of TEOS and 35 μl of APS was added to the mixture. After they had grown overnight, the rods were washed two times with ethanol, two times with water and two times with ethanol again. The rods were dispersed in 100 ml of ethanol and transferred to a closed round-bottom flask. After the addition of 25 mg of FITC to the rods in ethanol, the mixture was sonicated for about 1 minute and subsequently allowed to react overnight under magnetic stirring. The next day, the rods were washed with ethanol three times to remove all unreacted dye.

3.2.2. Fluorescent shells

A (45 nm) fluorescent silica shell was grown around silica rods of $L = 3.2 \mu\text{m}$ and $D = 320 \text{ nm}$ by dispersing all particles ($\sim 0.7 \text{ g}$) that had been prepared as described in Chapter 2 in 100 ml of ethanol. Under gentle magnetic stirring in a round-bottom flask, 5.0 ml of ammonia, 5.0 ml of water and 1.0 ml of TEOS were added to the rods in this order. Additionally, a mixture of 25 mg of FITC and 35 μl of APS that had reacted overnight in 5 ml of ethanol was added to the rods. After it had reacted in the closed flask for several hours, the mixture was centrifuged at 2000 rpm for 30 minutes (Hettich rotina 46s or Eppendorf 5810 centrifuge) and washed with ethanol three times.

When 35 mg of RITC was added in stead of 25 mg of FITC, the rods were washed in a mixture of ethanol and ammonia (5 ml of ammonia per 100 ml of ethanol) to keep them stable. After the growth of an additional non-fluorescent shell of ~ 50 nm, the rods were stable in ethanol. This extra layer was found to be necessary because RITC, being cationic, compromises the stability of the otherwise negatively charged silica. Without the extra silica layer the rods aggregated and sedimented quickly.

3.2.3. Multi-colored rods

Rods with two different dyes incorporated were grown in two reaction steps. One day before use, the dye was coupled to APS: 25 mg of FITC and 35 mg of RITC were each dissolved in 2.5 ml of ethanol in two separate flasks by sonication and heating the bottle with hot tap-water of about 70°C for 1-2 minutes. When all dye had dissolved, 20 μ l of APS was added to each solution. In the first step of the synthesis, 12 ml of water, 2.0 ml of 0.18 M sodiumcitrate in water, 25 ml of ethanol and 6.7 ml of ammonia were mixed with a solution of 30 g of PVP in 300 ml of pentanol. Then, 3 ml of TEOS and the 2.5 ml of RITC that was attached to APS and dissolved in ethanol was added. After 1 night, again 3 ml of TEOS and 2.5 ml of FITC/APS-complexes in ethanol were added. The next morning, the rods were washed with ethanol and water as described before.

3.2.4. Preparation for single particle imaging

Non-fluorescent shells were grown around the fluorescently labeled rods by dispersing ~ 1 g of them in 100 ml of ethanol and mixing them with 5 ml of ammonia, 5 ml of water and 1.5 ml of TEOS. The thickness of the shells depends on the dimensions of the core particles assuming no secondary nucleation occurred. It is known from literature that the same volume of silica grows around each core particle [54]. After reacting under gentle magnetic stirring in a closed round-bottom flask for a few hours, the rods were washed with fresh ethanol three times. This procedure can be repeated (with a variable amount of TEOS) to obtain the desired shell-thickness.

To obtain stable dispersions of silica rods in cyclohexyl chloride (CHC), rods were coated with 3-(trimethoxysilyl)propyl methacrylate (TPM) similarly to the procedure described in [79], or with octadecyltrimethoxysilane (OTMOS). For TPM coating, 0.7 g of rods was dispersed in 5.0 ml of ethanol and mixed with 3.0 ml of TPM (98%, Aldrich). After the addition of 1 ml of ammonia, the reaction was allowed to proceed overnight under magnetic stirring. The next day, the particles were washed with ethanol three times, after which the supernatant was removed as much as possible. The particles in the sediment were *not dried*, but redispersed in 1 ml of a 40 weight% solution of poly(12-hydroxy stearic acid) grafted on a backbone of PMMA in a mixture of ethyl- and buthylacetate (2:1 mass ratio), which acts as a stabilizer [80]. A drop of particles in stabilizer was added to approximately 3 ml of CHC (99%, Aldrich).

Larger inter-particle distances were achieved by coating the rods with OTMOS. To this end, rods with a length of 2.4 μm and a diameter of 580 nm were prepared as described in Chapter 2. These rods were coated with a fluorescent inner shell and non-fluorescent outer shell of around 100 nm. After washing with ethanol and removing unwanted short rods from the sample, the rods were dried at room temperature under vacuum for 1.5 hours. Subsequently, 50 mg of the dried sample and 5.0 ml of a solution of octadecyltrimethoxysilane (OTMOS, $\geq 90\%$, Fluka) in toluene (99.99%, Acros) (v/v=1/10) were mixed in a 20 ml glass vial. The sealed vial was sonicated for 4 hours at 30-50°C in a Branson 2510 sonicator. Then, the sample was centrifuged at 2000 rpm for 5 min and washed with toluene three times, two times with cyclohexane ($\geq 99.8\%$, Sigma-Aldrich) and finally two times with CHC. Finally, the rods were dispersed in 5.0 ml of CHC for further use.

3.2.5. Confocal microscopy

Sample imaging was performed on a Leica TCS SP2 confocal microscope. A 63 or 100 \times oil immersion objective (Leica) with numerical aperture 1.4 was used. RITC labeled rods were excited with a 543 nm laser line, FITC labeled rods with 488 nm. Images with a resolution of 512 \times 512 pixels were acquired.

The coordinates of the rods in confocal microscopy images were found using a code developed by Michiel Hermes (see Section 3.3.3 and [81]). For accurate identification of the rods' position and orientation, a minimum resolution of 10 pixels per particle diameter was required.

3.3. RESULTS AND DISCUSSION

3.3.1. Fluorescent labeling

Fluorescent labeling of silica by using a silane coupling agent, APS, has been successfully applied to spherical colloids [77,78]. The application of this technique is therefore an obvious step towards fluorescent rods. Figure 3.3 shows the result of the three methods that used APS as a coupling agent to bind the dye to the silica matrix. First, reaction products of APS and the isothiocyanate dyes were added at the same time in the synthesis procedure as the silica precursor TEOS. In contrast to the result for spheres, the dye did not get homogeneously distributed throughout the rods, but a clear gradient in fluorescence was measured from the head to the tail of the rod, as shown in Fig. 3.3a. Second, a mixture of APS and TEOS was used as a silica precursor during synthesis. The fluorescent dye was added after the rods had formed and been washed. Surprisingly, this resulted in the homogeneously dyed rods, as shown in Fig. 3.3b. These rods had approximately the same diameter as the rods shown in Fig. 3.3a (~ 300 nm).

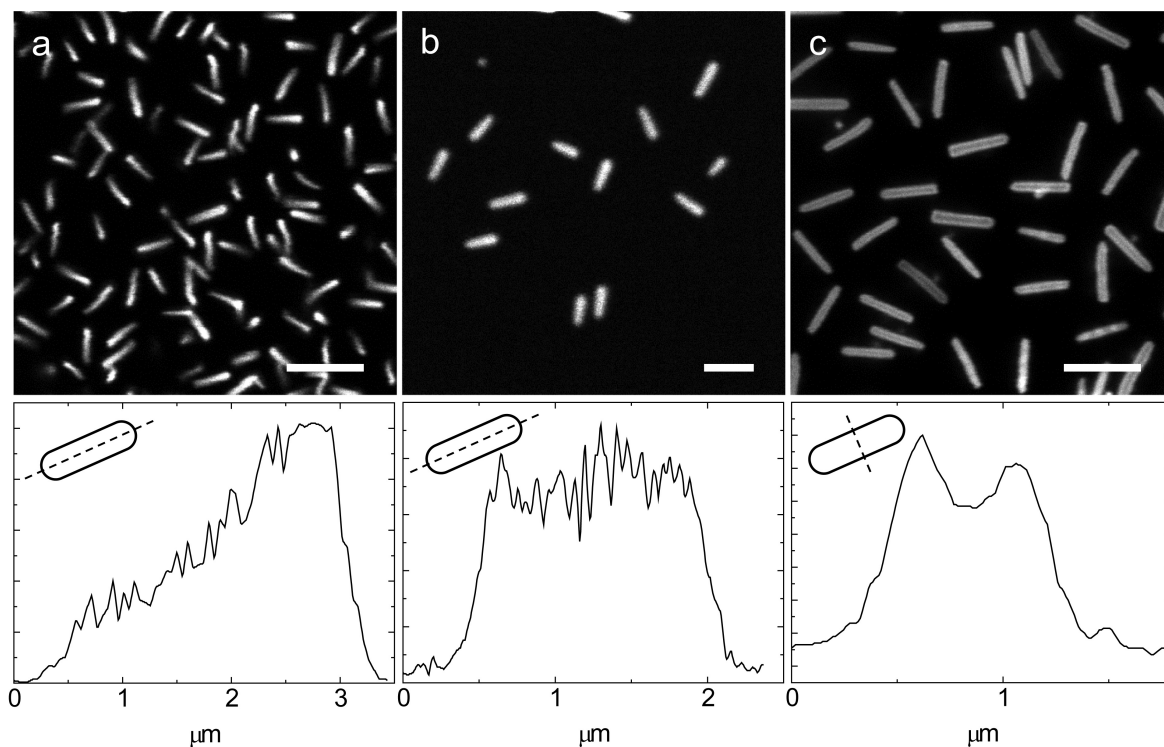


FIGURE 3.3. Rods with different fluorescent patterns in confocal images and corresponding graphs of intensity as a function of position in a rod. (a) Decreasing fluorescence towards the tail in rods when APS/dye-complexes were added at the start of rod-growth. (b) Homogeneously labeled rods when APS was built in during synthesis and FITC or RITC were added afterwards. (c) 30 nm thick fluorescent silica shells around a non-fluorescent core of the same diameter (~ 300 nm) as the rods in a and b. Scale bars indicate $5 \mu\text{m}$ for a and c, and $2 \mu\text{m}$ for b.

Third, a 30 nm shell of fluorescently labeled silica was grown around the 300 nm non-fluorescent cores, as shown in Fig. 3.3c. The three methods are discussed below.

Dye attached to APS. The addition of APS/dye-reaction products at the start of the synthesis resulted in particles with a dye-concentration decreasing from head to tail. An explanation for this phenomenon is offered by the growth mechanism of the rods, which is discussed in detail in Section 2.3.1. Summarized, a silica nucleus is formed at the interface of polymer-rich emulsion droplets of water in pentanol. Hydrolyzed TEOS molecules are dissolved in the emulsion droplet and grow onto the nucleus from the droplet-side only. Now, when APS/dye-reaction products are added to the synthesis mixture, they dissolve most likely directly in the emulsion droplets without hydrolysis of the APS units because of the more polar character of the dye molecules. TEOS, however, dissolves better in the continuous pentanol phase, and dissolves into water only after being hydrolyzed, which is a relatively slow process. So, while there is a

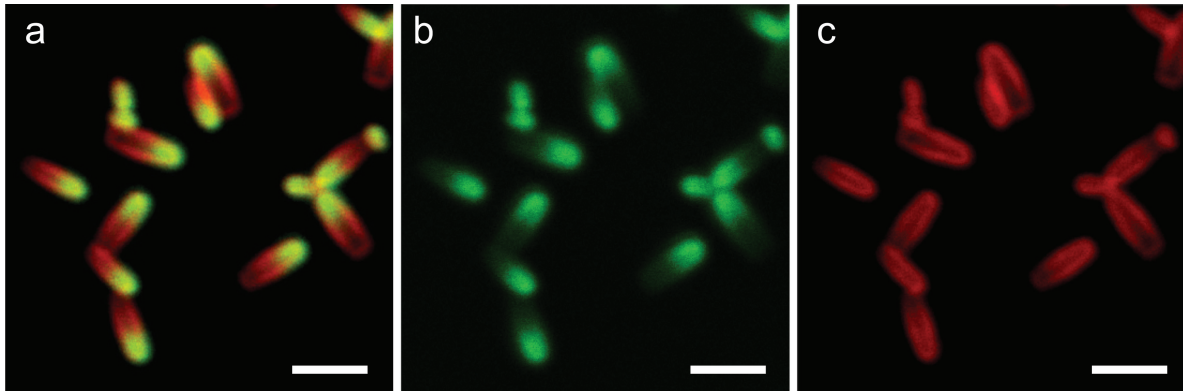


FIGURE 3.4. Rods with two different fluorescent dyes built in. (a) FITC and RITC signal combined in one image. (b) FITC signal only. FITC was added directly at the start of the synthesis. Fluorescence was mainly measured in the first half of the rods that had grown during the first day. (c) RITC signal only. RITC (and TEOS) was added after one day and was incorporated in shells around the already existing particle and the additionally grown second half of the rod. Scale bars indicate $2 \mu\text{m}$.

more or less constant feed of TEOS, the availability of dye is high at the start and decreases during growth, resulting in a concentration gradient of built-in dye molecules over the length of the rod.

Attempts to replenish the available APS/dye-reaction products during rod-growth, did not result in a more constant level of fluorescence. APS/dye-reaction products that were added later during the synthesis did not dissolve in the emulsion droplets, but grew mostly on the outer surface of the entire rod. This is shown clearly in Fig. 3.4, where two different dyes were used for the initial addition (FITC) and the addition after one day (RITC). The effect was already noticeable for APS/dye reaction products that were added one hour after the addition of TEOS, when the rod had just started growing. An explanation for the fact that dye attached to the coupling agent did not reach the water droplet when added later is probably caused by (partially) hydrolyzed TEOS molecules reacting with it and the outer silica before being able to reach the water. Further research needs to take place to further back this hypothesis. Long rods, for which a two-step synthesis is required, are best grown by adding only TEOS in the second step and no extra dye, to prevent the formation of a fluorescent shell.

An interesting feature of the rods with a gradient in fluorescence is the possibility it provides to distinguish between the round and the flat end of the rod. The same holds for the rods that were labeled with two different dyes shown in Fig. 3.4a. Using the particles with a gradient pattern, we examined the influence of the flat end on the orientation of the rods in a smectic phase. Figure 3.5 shows a SEM and a confocal image of rods in such a phase. From both images we can conclude that the orientation

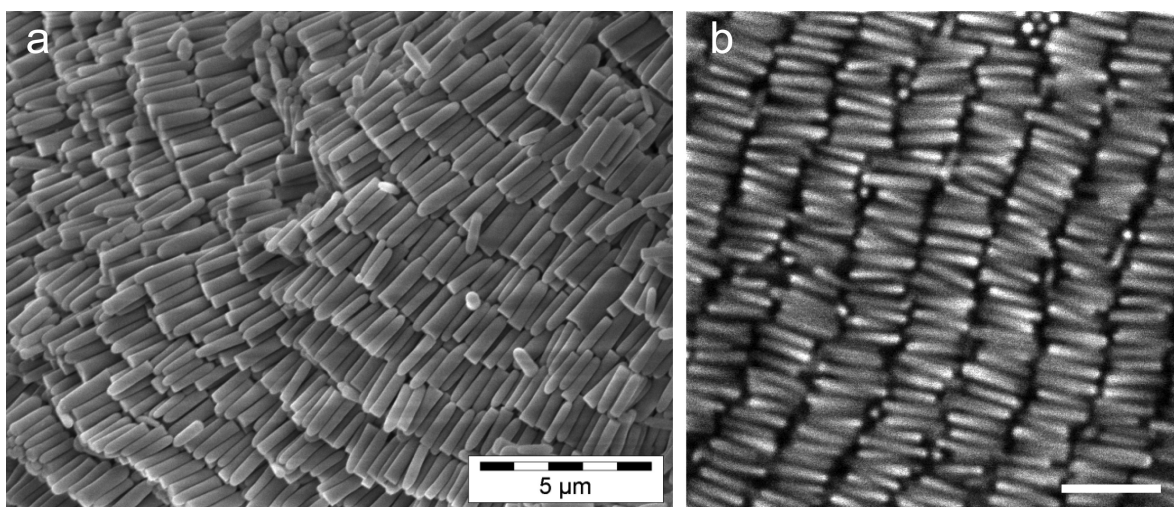


FIGURE 3.5. (a) Scanning electron microscopy (SEM) image of rods in a smectic or crystal phase. (b) Confocal microscopy image of rods with a gradient in fluorescence in a smectic liquid crystal phase. Both images show that the orientation of the rods within the layers is random. Scale bars indicate 5 μm .

of neighboring rods is random; the fraction of neighboring rods that point in the same direction is roughly equal to the fraction that points in opposite directions. The rods thus behave as if they have symmetric ends, at least with respect to their ordering in the liquid crystal phases observed with them so far.

Unbound APS. Instead of dye attached to APS, it is also possible to add uncoupled APS to the synthesis. Unlike APS that was coupled to a dye, uncoupled APS was apparently built in more homogeneously throughout the rods. The dye-molecule thus caused the gradient pattern described in the previous section and not the APS-molecule itself. In case uncoupled APS was added to the synthesis mixture, APS and TEOS both acted as silica precursor and the resulting particles consisted of a silica-matrix with more homogeneously distributed $-\text{C}_3\text{H}_6\text{NH}_2$ groups. The pores of the rods were sufficiently large to make the rods fluorescent by letting RITC or FITC molecules diffuse into the structure and bind to the free $-\text{C}_3\text{H}_6\text{NH}_2$ groups. The resulting rods have a homogeneous distribution of incorporated fluorescent dye-molecules, at least as far as can be observed with the limitations as opposed by the confocal resolution (Fig 3.3b). Rods in which no APS was incorporated also showed a weak fluorescence signal after dye-molecules were allowed to diffuse into them, but this signal was much weaker because most dye molecules were washed out during the washing steps to remove the dye from the solvent. This was not the case for dye-molecules that were covalently bound to the silica matrix. The method of incorporating APS first and subsequently letting dye diffuse in the particles does not work for Stöber silica spheres, since these particles are less porous (see Chapter 2 or [82]).

fluorescent pattern	(dis)advantages of the method
gradient (APS/dye added from start)	+ distinction between two ends – gradient makes confocal images hard to read
homogeneous (APS added from start)	+ most easy to find orientations and positions – limited control over dimensions due to instabilities
shell (APS/dye added after growth)	+ most control over dimensions rod – some aggregation during shell formation

TABLE 3.1. Summary of the results of the described labeling methods.

For quantitative data analysis it is necessary to determine the position and orientation of the rods, which is most easily done if the strongest fluorescence is in the center and along the backbone of the rods. Although the above described rods with a constant level of fluorescence are preferable for tracking algorithms, the control over the dimensions of such rods is limited. The addition of APS decreases the stability of the synthesis in such a way that the water content of the synthesis had to be increased from 8.4 to 11 ml to prevent the formation of curly rods. As a result, the APS-labeled rods became shorter than unlabeled rods. Therefore, the preparation of long rods ($L/D > 4$) using this method is more difficult. The disturbance of the synthesis mixture by APS that was coupled to a dye molecule was much less; in this case the water content needed to be raised to only 9.0 ml. Most likely these results are caused by the difference in the charge the growing particles end up with as a result from addition of the coupling agent.

Labeled shells. The third way of labeling the rods is the growth of a fluorescently-labeled shell after preparation of non-fluorescent rod-cores. The method of coating silica rods with a fluorescent shell is in this case analogous to the coating of spheres. Unfortunately, the problem of aggregation was much more pronounced for the coating of rods. In literature we found that aggregation is contributed to the presence of APS-molecules on the surface of the silica particles. These decrease the stabilizing negative surface charge of the silica layer by its basic amino groups, resulting in unstable particles [83–85]. Aggregation was reduced by decreasing the ammonia concentration or by dilution of the core suspension during shell growth. Additionally, aggregates were removed from the sample by repeated sedimentation after which only the particles in the top part of the supernatant were used. We noticed that aggregation was much more severe when RITC was used compared to FITC. Both RITC-coated rods and RITC-labeled spheres were not stable in pure ethanol. The addition of ammonia to unstable dispersions in ethanol restored colloidal stability, when the final concentration was higher than 0.5 M. An explanation for this observation is also offered by charge stabilization. The

FITC-molecule is negatively charged in ethanol, because part of its hydroxyl-groups are dissociated, and therefore does not disturb the negative surface charge of silica. RITC, on the other hand, is also a base working against the negative surface charge (Fig. 3.2). Additionally, the basic amino groups of unbound APS reduces the surface charge of the particles, which causes aggregation. We speculate that the addition of ammonia cancels this effect because it induces dissociation of the carboxyl-group and reduces ionization of APS. After the growth of an additional non-fluorescent shell, the RITC-labeled particles were found to be stable in pure ethanol again.

Despite the problems with aggregation, the above described method offers most control over length and diameter, because the cores can be grown without the addition of disturbing components such as APS or, to a lesser extent, APS/dye-reaction products. The fact that aggregation does not occur in the unbound APS or the APS/dye-reaction product method is probably due to PVP that acts as a steric stabilizer on the surface of the rods.

The main results of the dye labeling using the three methods are summarized in Table 3.1.

3.3.2. Single particle imaging

Fluorescent labeling alone is not enough to enable the study of colloidal rods on the single-particle level; the limited resolution of the microscope compared to the thickness of the rods (300 nm) requires further processing of the rods. The resolution of our confocal microscope, is limited to about 250 nm in the horizontal plane (see Section 3.1.1), which means that the fluorescent parts of the rods should be separated by at least 250 nm for single particle detection. The lower resolution in z , however, makes it necessary to increase this to at least 600 nm as was found experimentally for spheres [86]. In concentrated and/or strongly interacting samples, this can be achieved in two ways: the growth of unlabeled shells around the labeled cores, or an increase of the particles' double layer.

Figure 3.6 demonstrates the effect of separating the fluorescent cores of the rods. Figure 3.6a shows a concentrated sample of rods with a length L of 1.4 μm and a diameter D of 280 nm, that have a fluorescent shell only. At high concentrations the rods form the layers of a smectic phase (as discussed in more detail in Chapter 4). Since the distance between the labeled shells within the layers is too small, individual particles cannot be distinguished. The spacing between the layers, however, is apparently larger than 250 nm, according to the stripes that are visibly running from top to bottom in the image.

Rods with an extra, non-fluorescent shell around their dyed cores are shown in Fig. 3.6b. These rods of $L = 2.4 \mu\text{m}$ and $D = 640 \text{ nm}$ consist of a non-fluorescent core, a 30 nm fluorescent inner shell and a 190 nm non-fluorescent outer shell. The outer shell

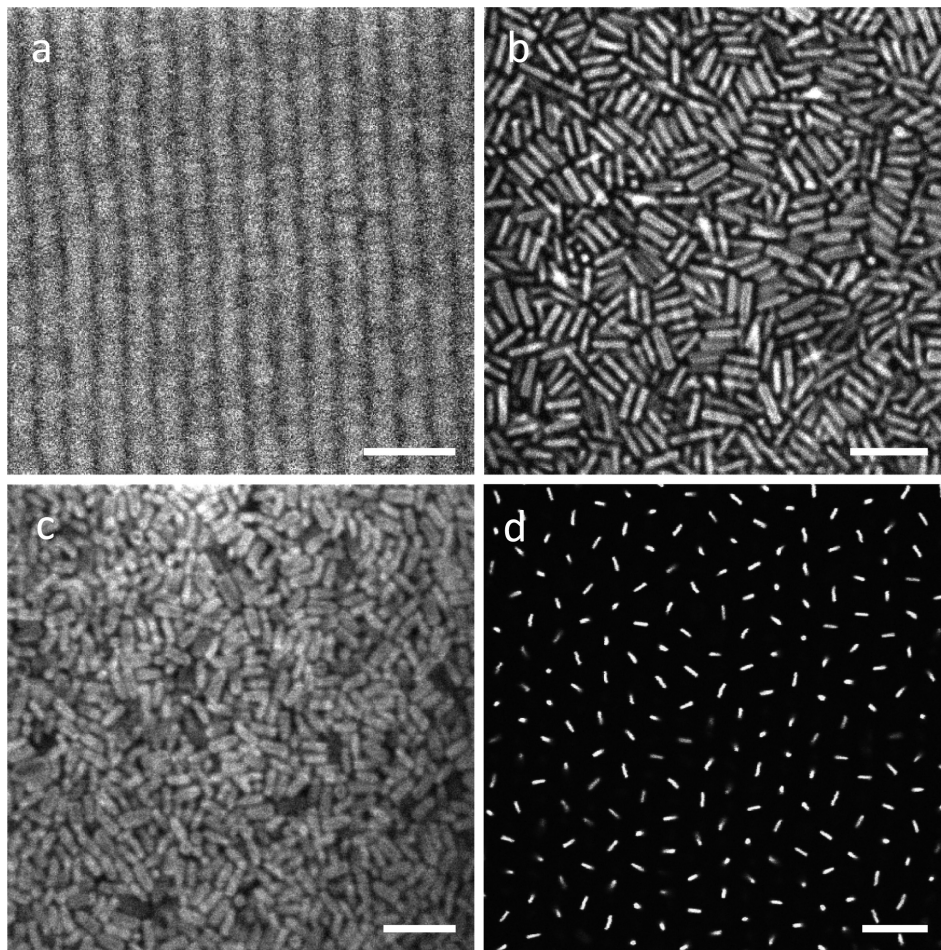


FIGURE 3.6. Confocal microscopy images of rods. (a) $L = 1.4 \mu\text{m}$ and $D = 280 \text{ nm}$ rods coated with a fluorescent silica shell only. Ordering in layers can be distinguished, but single particles are indistinguishable. (b) $L = 2.4 \mu\text{m}$ and $D = 640 \text{ nm}$ rods with a 190 nm thick non-fluorescent shell around their fluorescent shell. Single particles are clearly visible. (c) $L = 1.7 \mu\text{m}$ and $D = 550 \text{ nm}$ rods coated with a single fluorescent silica shell and TPM, dispersed in CHC to induce longer-ranged repulsions and larger inter-particle distances. (d) $L = 2.4 \mu\text{m}$ and $D = 580 \text{ nm}$ rods coated with OTMOS, dispersed in CHC with micron-sized double layers. Scale bars indicate $5 \mu\text{m}$ for a-c and $10 \mu\text{m}$ for d.

assures a 380 nm minimum distance between the fluorescent parts of the rods, which are therefore individually well visible. It should be noted, however, that beside the separation of the cores, the extra silica layers also decrease the aspect ratio of the rods and add mass to the particles. Therefore, it becomes harder to prepare high aspect ratio particles. Additionally, the gravitational height of the rods is decreased, sedimentation velocities are increased and dynamics is slow for larger particles. Figure 3.7 illustrates the problem. In Fig. 3.7a and b the core particles are compared to the particles with a

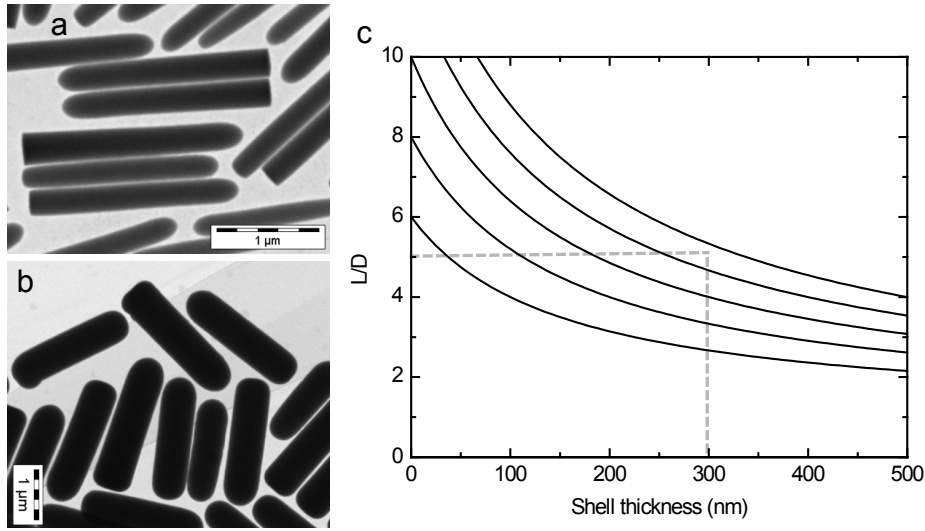


FIGURE 3.7. Effect of shell-growth on aspect ratio. (a) System of rods directly after synthesis ($L/D = 8.2$). (b) The same system after growth of a 220 nm shell ($L/D = 3.6$). (c) L/D as a function of shell thickness for rods with a diameter of 300 nm. The lines from top to bottom are initial L/D -ratios of 14, 12, 10, 8 and 6 respectively.

220 nm thick shell. Besides a clear decrease in aspect ratio, the flat end of the particle became more rounded, making the rod resemble a spherocylinder more. The decrease in aspect ratio of the rods is illustrated by Fig. 3.7c. The lines from top to bottom in the graph are initial L/D -ratios of 14, 12, 10, 8 and 6 respectively. For a minimum shell thickness of 300 nm, and a minimum L/D of 5, which is needed to allow for all liquid crystal phases, cores need to be prepared with an aspect ratio of 13. However, the preparation of rods with length of $3.9 \mu\text{m}$ and a diameter of 300 nm stretches the limits of the synthesis procedure. A method to reach single particle imaging without adding mass to the rods is increasing the double layer. The double layer for colloids in solvents with a low dielectric constant (ϵ) is much larger than in solvents with a high ϵ [31]. CHC is an example of such a solvent, with an ϵ of 7.6. Additionally, the refractive index of this solvent ($n = 1.46$) matches that of silica ($n = 1.45$) well. Moreover, the phase behavior of particles with an anisotropic shape and double layer large compared to their size have hardly been studied yet [87]. A stable dispersion in CHC was obtained by coating the rods with TPM and adding a steric stabilizer. A dispersion of rods with $L = 1.7 \mu\text{m}$ and $D = 550 \text{ nm}$ in CHC, coated with a fluorescent layer only, is shown in Fig. 3.6c. Individual particles are better visible than before (compare to Fig 3.6a), but are not very far apart yet. Larger double layers were achieved by coating the rods with OTMOS before transferring them to CHC. Figure 3.6d shows the micron-sized double

layers that were achieved this way. Since the extent of the double layer depends on the ion concentration in the solvent, the double layer can be tuned by adding or removing ions from the sample.

3.3.3. Identifying position and orientation of rods in CSLM data-stacks

Our system of silica rods was designed to perform quantitative real-space measurements. The final requirement to achieve this is an algorithm to identify the positional and orientational coordinates of the rods in a 3D data-stack. To this end, an algorithm was developed that is able to find the rods in 2D images, and an algorithm to find the rods in 3D stacks. Both algorithms consist of five steps, which are described below and will be detailed in an upcoming publication [81].

The first step to identify the positions and orientations of rods in 2D images or 3D stacks is filtering, which is done by smoothing it with a Gaussian filter and subtracting the background. The second step identifies the backbone, or main axis, of the rods. This step is different for two and three dimensions. In two dimensions this is done by first finding all pixels brighter than a value that can be set by hand, typically 0.2 times the maximum pixel value. Next, the code loops over all brighter pixels within a circle of radius 2 of the pixel in question. For these bright neighboring pixels ϕ is calculated; the angle between the x -axis and the vector between the bright neighboring pixel and the pixel in question. When the absolute value of the complex sum of $\exp(2\pi\phi)$ for all the bright pixels divided by the number of bright pixels is larger than 0.95, the pixel is called a backbone pixel. In three dimensions the algorithm also starts by looking at all pixels brighter than a value which can be set. Next the code loops over all brighter pixels within a sphere of radius 2 of the pixel in question. For these bright neighboring pixels the gyration tensor is calculated to obtain the least squares fit of a straight line through these pixels. To obtain the deviation from a straight line the largest eigenvalue of the gyration tensor is computed. If the deviation from a straight line is small (the eigenvalue is larger than a tunable value) the pixel is called a backbone pixel.

In the third step, the backbone pixels are grouped. Two backbone pixels are assigned to one rod when the distance between them is 3 pixels or less. The backbones are split when they contain pixels positioned further than half the expected rod radius from the straight line that connects the beginning and end point of the rods.

Next, in step four, a line is fitted through the group of pixels belonging to one rod. This produces a center, length and orientation, with strong pixel bias. To obtain more accurate results a second fit is performed on the filtered image pixels within one rod radius (this radius is one of the parameters that can be set) of the line resulting from the first fit. The center of the rod is obtained by calculating the center of mass of the pixels weighted with their intensity. The orientation is determined by calculating the eigenvector corresponding to the largest eigenvalue of the gyration tensor. The final

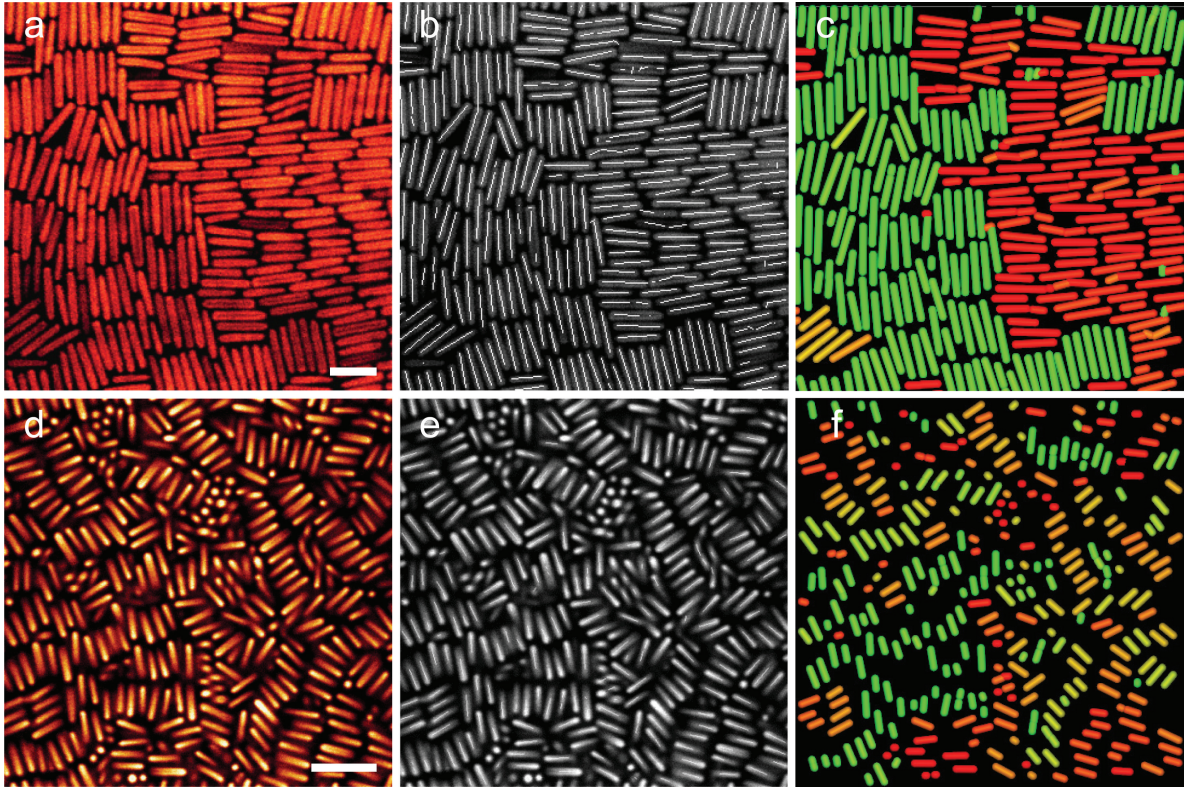


FIGURE 3.8. 2D rod identification results. (a) Confocal microscopy image of rods on the bottom glass plate ($L = 3.3 \mu\text{m}$, $D = 550 \text{ nm}$, 190 nm thick unlabeled shell). Scale bar indicates $3 \mu\text{m}$. (b) Overlay of backbones and confocal image. (c) Identified rods. The different colors denote different orientations. (d) Confocal image of rods with a decreasing intensity pattern in the bulk phase, about $2 \mu\text{m}$ from the bottom ($L = 2.6 \mu\text{m}$, $D = 630 \text{ nm}$, 175 nm thick unlabeled shell). Scale bar indicates $5 \mu\text{m}$. (e) Overlay of backbones and confocal image. (f) Identified rods.

length is determined by taking the product of the expected diameter of the rod and the ratio of the two eigenvalues of the gyration tensor or, in three dimensions, the ratio of the largest eigenvalue and the average of the other two eigenvalues.

Finally, in step five, it is possible to filter out rods containing not enough intensity, or rods of which the length estimated by the last two fitting steps is very different, or in three dimensions very short rods. It is preferable to do as little filtering as possible.

The 2D algorithm works well for dilute systems, as does the algorithm developed by Mohraz and Solomon for ellipsoidal PMMA particles, which only assigns backbones to the rods [24,88]. Since rods in a dilute system move fast compared to the scanning speed, 3D imaging of such a system is not possible without fixing the rods, for instance by polymerization of the medium [89,90]. However, a good indication of the orientation of the rods can be obtained from the analysis of 2D-slices of a 3D-system, even for

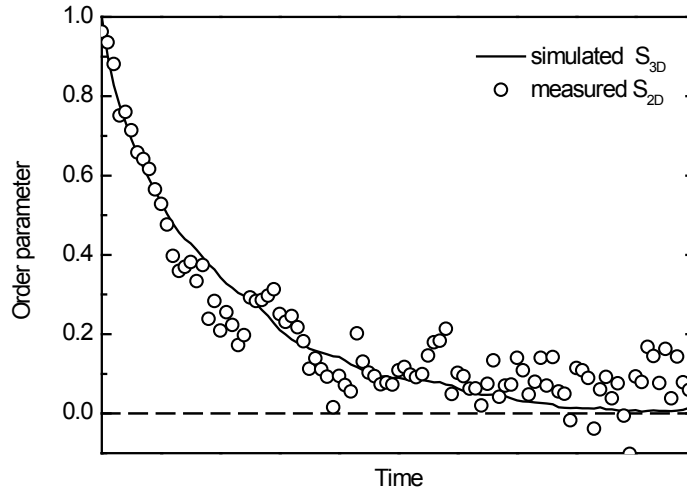


FIGURE 3.9. Order parameters in a 3D computer generated data set of an in plane, fully aligned nematic phase that relaxes in time to a disordered isotropic phase ($\phi = 0.3$). The open circles denote the 2D order parameter that was found by the rod identification algorithm, which agrees well with the actual 3D order parameter (solid line) that was calculated from the simulation data.

high volume fractions such as shown in Fig. 3.8. Imaging and identifying coordinates works best at the bottom glass plate (Figs. 3.8a-c), but also in the bulk at least the orientational coordinates can be found (Figs 3.8d-f). Additionally, Figs. 3.8d-f show that even for rods with a gradient pattern (which makes them appear to be partly out of the focal plane) the orientation can be determined. The lengths that were found for this kind of rods are not correct, of course.

To analyze how well the orientations found in 2D-slices compare to the actual orientations in the 3D-system, a 3D-set of computer generated coordinates was used. A 3D Molecular Dynamics simulation with an initial configuration of 4000 $L/D = 5$ rods that were perfectly aligned in the plane of the 2D slices that were taken, was run for 50 time steps. For this set of data, the 3D nematic order parameter S_{3D} was calculated:

$$S_{3D} = \frac{3}{2} \langle \cos^2 \theta \rangle - \frac{1}{2}, \quad (3.3)$$

with θ the angle between the long axis of the rod and the nematic director. Because the volume fraction was 0.3, the equilibrium phase for these rods is the isotropic phase. Therefore, during equilibration of the system, the nematic order parameter decreased from 1 to 0 (Fig. 3.9). To assess whether the orientational coordinates found by the 2D identification algorithm correspond to the calculated order parameters, a confocal data stack was simulated. The simulation data were re-scaled so that the volume fraction was 0.1, the box-size $256 \times 256 \times 256$ voxels and the diameter of the rods 4.5 pixels. Then, the computer generated data were convoluted with a 3D Gaussian fit to the point

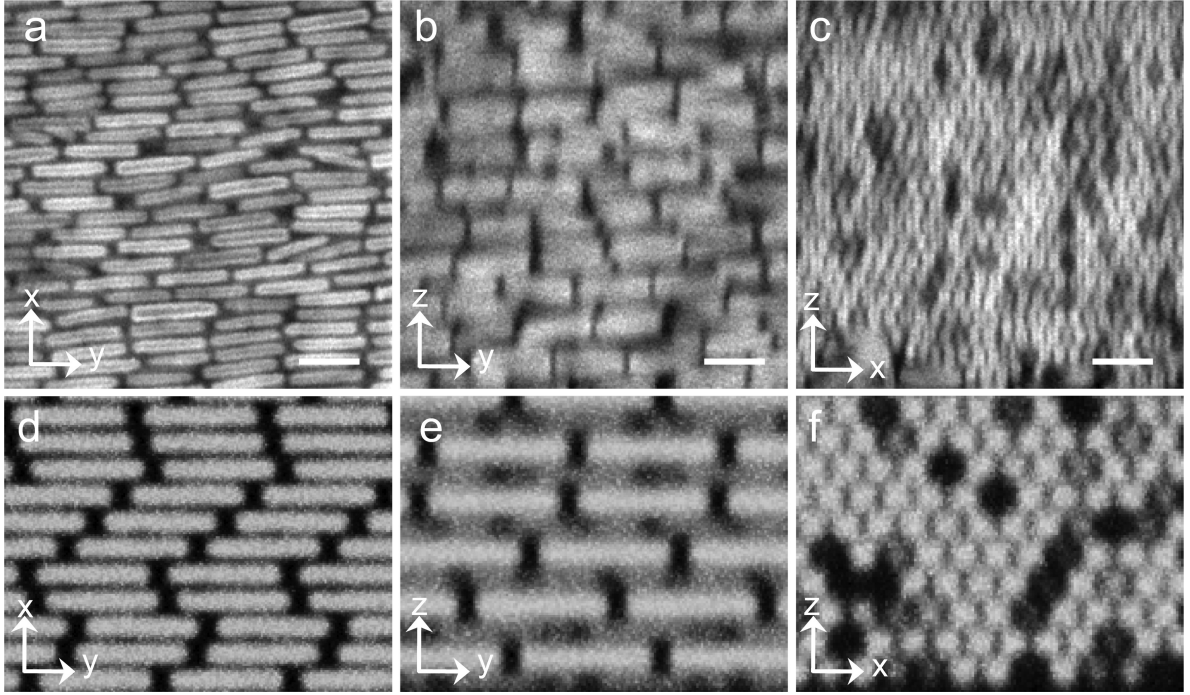


FIGURE 3.10. Effect of an anisotropic point spread function. Simulated ‘experimental’ data (d-f) of a hexagonal columnar phase constructed from a computer generated data set compared to real experimental confocal microscopy data (a-c). See text for details on how the simulated data were created. Due to the lower resolution in z , the diameter of the rods appears larger in z than in the x and y direction. Scale bars indicate $3 \mu\text{m}$.

spread function ($\sigma_x = \sigma_y = 0.2D$ and $\sigma_z = 0.4D$). After the addition of some random Gaussian noise ($\sigma = 0.02D$), a 2D slice of the sample resembled the real experimental data well. Using the simulated experimental data, the orientation of the rods was determined with our algorithm and the 2D order parameter S_{2D} was calculated:

$$S_{2D} = \langle \cos(2\theta) \rangle. \quad (3.4)$$

The values for S_{2D} that were obtained for the rods in the nematic phase that relaxed to the isotropic phase are depicted as open circles in Fig. 3.9. This figure shows that the 2D order parameter determined from 2D slices gives a good indication of the actual 3D order parameter of the system, at least when the director lies in the imaging plane of highest resolution. Analysis as a function of the orientation of the rods compared to the imaging plane is in progress.

A comparison between simulated experimental data and real experimental data is shown in Fig. 3.10. This figure shows three side views of an experimental (a-c) and a simulated (d-f) hexagonal columnar phase that was constructed as described before. The point spread function had $\sigma_x = \sigma_y = 0.15D$ and $\sigma_z = 0.3D$ and the Gaussian noise $\sigma = 0.01D$. The effect of the anisotropy of the point spread function in the z -direction

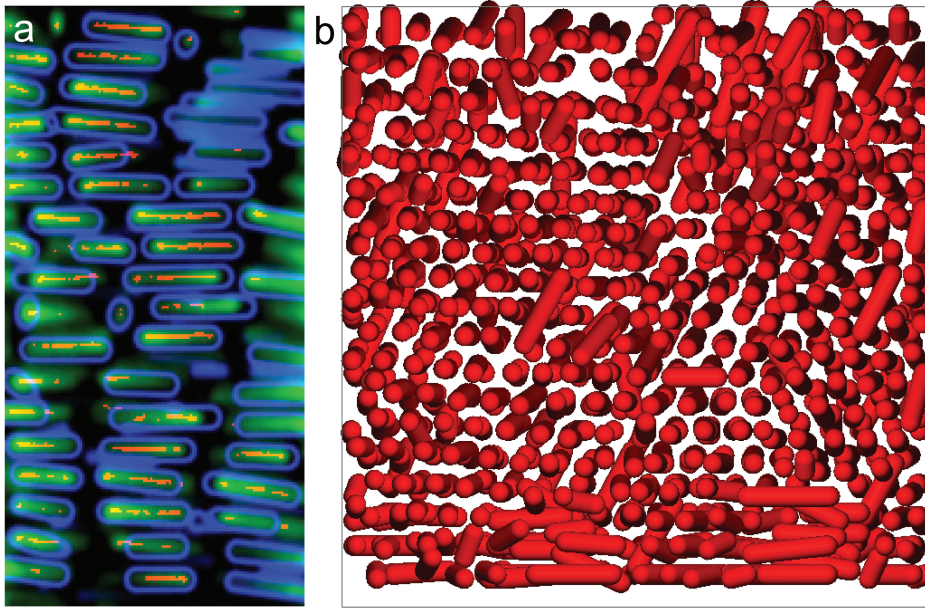


FIGURE 3.11. 3D rod identification results for rods of $L = 2.6 \mu\text{m}$ and $D = 630 \text{ nm}$ in a smectic phase. (a) Overlay of the experimental image (green), assigned backbone (red) and contour (blue) of the found rod. (b) 3D rendering of the coordinates found in a confocal microscopy data-set.

compared to the xy -plane is clearly visible in Fig. 3.10b/e, where the diameter of the rods in the yz -plane appears broader than in the xy -plane (Fig. 3.10a/d).

Figure 3.11 shows that the algorithm in principle works for 3D data-stacks in dense sediments. This has not been shown for the algorithm of Mohraz and Solomon. However, the identification of rods in 3D data-stacks is not optimal yet. On the experimental side it is essential that the core of the rods is labeled (and not a shell) and that a sufficiently thick ($> 200 \text{ nm}$) unlabeled shell is grown. Furthermore, a high scanning speed (1000 Hz, bidirectionally scanned) needs to be used to prevent the rods from moving too much during scanning. The stack that is shown in Fig. 3.11 consisted of images of 256×128 pixels ($14.88 \times 7.44 \mu\text{m}^2$) with a distance of $0.104 \mu\text{m}$ between the images in the z -direction. It was taken in a dense sediment in a smectic phase.

3.4. CONCLUSIONS

In order to study the systems with CLSM, silica rods were made fluorescent and adapted to satisfy the resolution limits of a ‘conventional’ confocal microscopy system. Rods with different fluorescent patterns were prepared. Due to the asymmetric growth-mechanism of the rods, rods were created with a decreasing gradient in concentration from head to tail. These rods make it possible to distinguish between the rods’ round head and flat tail. A homogeneous distribution of dye molecules was achieved by the incorporation of APS-molecules that were subsequently bound to dye-molecules that

diffused into the rods. Finally, fluorescent shells were grown successfully after rod growth was finished in an ethanol/water/ammonia mixture, similarly to shell-growth around silica spheres. Each of these methods has its own advantages and disadvantages (Table 3.1).

The limited resolution of the confocal microscope requires separation of the fluorescent cores. Single particle imaging was achieved by creating core-shell rods that had a fluorescent core and a non-fluorescent shell. Alternatively, the rods could be coated with TPM and octadecyl groups and dispersed in a low ϵ ($4 < \epsilon < 10$) solvent to facilitate the possibility to obtain micron-sized or larger double layers.

The quantitative analysis of CLSM data is facilitated by a new tracking algorithm. This code finds the position and orientation of the rods, which were used to calculate order parameters. Although analysis as a function of the orientation of the rods compared to the imaging plane is still needed, it was found that the orientational order parameter determined from 2D slices gives a good indication of the 3D order parameter of the system, at least when the director lies in the imaging plane of highest resolution.

3.5. ACKNOWLEDGEMENTS

We would like to thank Johan Stiefelhagen for fruitful discussions on fluorescent labeling. Bing Liu is acknowledged for the synthesis of the rods coated with OTMOS. Furthermore, we would like to thank Michiel Hermes for developing the tracking algorithm and Thijs Besseling for testing the code.

Part 2

Phase behavior of rods in external fields

4

Phase behavior of colloidal silica rods studied in real and reciprocal space

ABSTRACT

A novel experimental hard-rod-like model system was used to study the phase behavior of colloidal silica rods with aspect ratios ranging from 3.6 to 8.0. Besides the expected nematic and smectic liquid crystalline phases for the higher aspect ratios, we found a smectic-*B* phase at high densities for all systems. By combining real-space confocal laser scanning microscopy and small angle X-ray scattering methods, a phase diagram depending on concentration and aspect ratio was constructed, which shows good qualitative agreement with the simulation results for the hard spherocylinder system. Additionally, real-space measurements on the single-particle level provided preliminary information on defects and dynamics.

4.1. INTRODUCTION

The phase behavior of anisotropic particles is richer than that of spherical particles. In addition to the gas, liquid, crystal or glass phases that were observed for spheres, anisotropic particles such as rods form liquid crystal phases: additional phases between the liquid and crystal phase that possess orientational and positional order in less than the three dimensions of a full crystal. The first theoretical explanation for the formation of the nematic phase was provided by Onsager in 1949 [25]. He argued that the transition from the isotropic to the nematic phase for long, hard rods could be purely entropy based. Later, computer simulations showed that not only nematic, but also smectic and crystalline phases can occur in systems of hard spherocylinders (HSC) [26,27]. Figure 4.1 shows that the formation of liquid crystal phases depends on the concentration and aspect ratio of the rods. Short rods, with aspect ratio smaller than 4.1, behave comparable to spheres; only liquid and crystalline phases were found by computer simulations. At slightly larger aspect ratios a smectic phase was found between the isotropic and crystal phases and for aspect ratios higher than 4.7, the nematic phase was also found to be stable. Besides concentration and aspect ratio, the shape of the particles is also an important parameter. Ellipsoids, for example, only show a nematic liquid crystal phase, while for spherocylinders a nematic and a smectic phase was found, as summarized in [91].

The experimental verification of the simulation results requires a system of hard rods. Research has shown that colloidal spheres are a good model system for the hard sphere system if the always present and attractive van der Waals interactions can be sufficiently suppressed [8]. Equivalently, we expect our system of silica rods to be a good candidate for the hard rod system. However, there are some differences between our rods and a perfect HSC-system. Firstly, our experimental system of rods as described in Chapter 2 is initially bullet-shaped. Nevertheless, the rods resemble the shape of a spherocylinder more and more after coating with several extra shells to make them suitable for confocal laser scanning microscopy (CLSM) (see Chapter 3). Secondly, experimental colloidal systems always have an inherent polydispersity which influences their phase behavior. For HSC-systems it was shown that a smectic phase can only form if the length polydispersity is below 18% [92]. If the polydispersity is higher, a columnar phase is formed rather than a smectic phase at high volume fractions. Thirdly, a colloidal dispersion of silica rods is a charge-stabilized system. It is known that charges increase the effective diameter of needles [93], and also colloidal charges and weak-screening conditions lead to a decreased aspect ratio of charged rods [87]. Additionally, theoretical studies showed that charge tends to stabilize the positionally ordered phases, especially the columnar phase, and decrease the nematic and smectic phase [94,95].

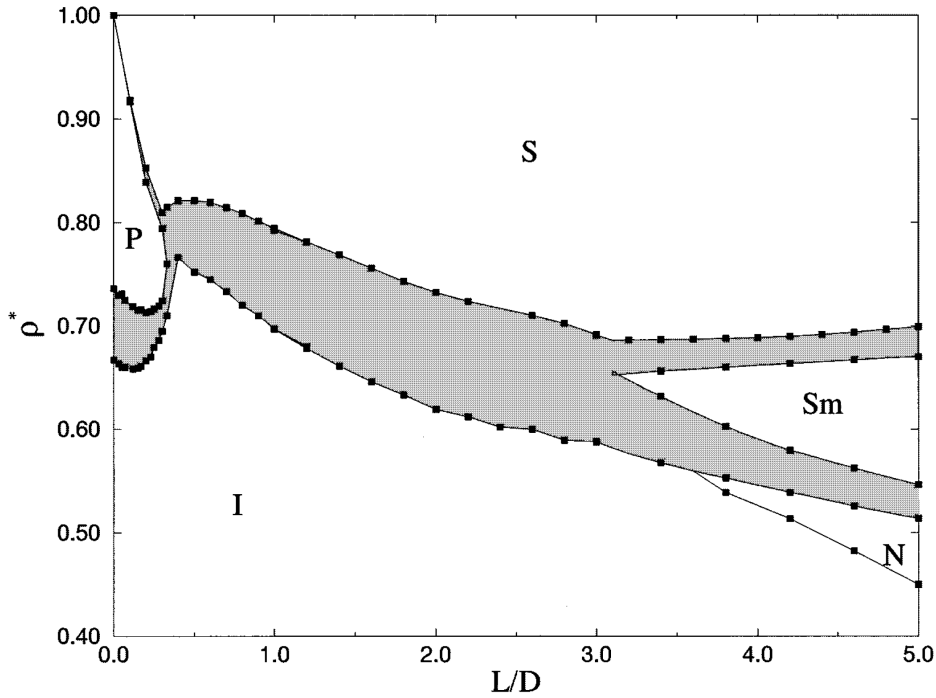


FIGURE 4.1. Phase diagram for hard spherocylinders, computed by Bolhuis and Frenkel [96]. Here, L denotes the length of the cylindrical part of the spherocylinder, D is the diameter and ρ^* the density relative to close packing. Since we take L the full length of the rod, the corresponding experimental L/D is the value in the graph + 1.

Despite the differences between the experimental system and model, it was shown for equivalent systems of charged spheres that the effective increased diameter due to charge can be used to map results on phase behavior on the hard sphere system [65]. The mapping of charged rods onto a hard rod system can be done similarly.

In contrast to other rod-like colloidal systems, our system allows for real-space measurements on the single particle level. Experimentally, research on rod-like particles has been limited to the many-particle level and reciprocal space for a long time. Even though it is possible to distinguish smectic phases of, for instance, *fd*-virus using light microscopy, the individual particles can only be imaged this way when a doped system is used (in which 1 on every 30000 particles is labeled) [97, 98]. Imaging all individual particles is not possible in this system using light microscopy. Studies involving mineral liquid crystals, like boehmite or goethite are also based on many-particle effects such as birefringence and scattering [99–102]. The first real-space data on the single-particle level were reported by Maeda *et al.* in 2003 [45]. They showed the process of self-ordering for several aspect ratios of rods. Although their observations already provide a lot of extra information compared to scattering experiments, the range of the information is limited by the systems that were used. The systems that

were studied by Maeda consisted of rods with high refractive indices. The resulting strong scattering makes it hard to obtain 3D data for these systems. In our system, however, the refractive index can be matched to that of the solvent, which enables 3D analysis using confocal microscopy.

In this chapter, we describe the phases that were found in sediments of rods using small angle X-ray scattering (SAXS) and real space CLSM measurements. By combining the results of both methods a phase diagram was constructed depending on aspect ratio and volume fraction. Furthermore, we show real-space measurements on the single-particle level that provide detailed information on defects and dynamics in concentrated phases.

4.2. SEDIMENTATION OF RODS

In the experiments described in this chapter, we generally start with a relatively dilute dispersion of rods (around 10 vol%). In time, the rods sediment and the concentration of the rods on the bottom of the capillary increases. The time-scale of the sedimentation process depends on the mass and friction factor γ of the rods. γ can be found in the expressions for the translational D_t and rotational D_r diffusion coefficients since the diffusion coefficient is equal to $\frac{k_B T}{\gamma}$. For dilute suspensions, the expressions for the diffusion coefficients of finite rods, modeled as cylinders are [103]:

$$D_t = \frac{k_B T (\ln(\frac{L}{D}) + v)}{3\pi\eta_0 L} \quad \text{and} \quad D_r = \frac{3k_B T (\ln(\frac{L}{D}) + \delta_\perp)}{\pi\eta_0 L^3}. \quad (4.1)$$

In these expressions $k_B T$ is the thermal energy, L the total head-to-tail length of the rod, D the diameter and η_0 the viscosity of the solvent. The factors v and δ_\perp are used to include end-effects, which should be corrected for in the case of short rods ($2 < L/D < 30$) [104]:

$$v = 0.312 + 0.565 \frac{D}{L} - 0.100 \left(\frac{D}{L}\right)^2 \quad (4.2)$$

$$\delta_\perp = -0.662 + 0.917 \frac{D}{L} - 0.050 \left(\frac{D}{L}\right)^2. \quad (4.3)$$

For a typical silica rod, with a length of 3.3 μm and a diameter of 550 nm, the time needed to diffuse a distance of D is about 1 second. The time needed to rotate over an angle π is about 1 minute. Using the expression for D_t , the sedimentation velocity of the rods can be obtained via the Svedberg equation:

$$v_{sed} = \frac{V_{rod} D_t g (\rho_c - \rho_s)}{k_B T}, \quad (4.4)$$

where g is the gravitational constant, ρ_c the colloid's density and ρ_s the density of the solvent. The volume of the rod, V_{rod} , is approximated by the volume of a cylinder with

one hemispherical cap:

$$V_{rod} = \frac{1}{4}\pi D^2(L - \frac{1}{6}D). \quad (4.5)$$

For our typical rod, the thus calculated sedimentation velocity is 12 $\mu\text{m}/\text{min}$. The expression for v_{sed} (Eq. 4.4) only holds for very dilute dispersions ($\varphi < 0.0001$). However, from the work of Dogic *et al.* we know that for infinitely long rods the sedimentation velocity rapidly decreases with increasing concentration [105].

When the sedimenting system has reached an equilibrium, two regimes can be distinguished: a dilute top region and a more concentrated bottom region. In the dilute regime, the equilibrium sedimentation profile is barometric, and the volume fraction of the colloidal particles decays exponentially with height: $\varphi = \varphi_0 \exp(-z/l_g)$, where φ_0 is the volume fraction at $z = 0$. The decay constant is the gravitational length $l_g = k_B T/mg$ (for our systems listed in Table 4.1). At higher volume fractions the increased gravitational pressure on the particles in the sediment is balanced by an osmotic pressure gradient:

$$\frac{d\Pi(z)}{dz} = g(\rho_s - \rho_c)V_{rod} \varphi(z), \quad (4.6)$$

with $\Pi(z)$ the osmotic pressure and $\varphi(z)$ the volume fraction of rods at a height z in the sediment. Equation 4.6 is only valid when the particle concentration can be assumed to be constant on length-scales several times larger than those over which the particles interact. From Eq. 4.6 follows that the volume fraction in the final sediment varies as a function of height. If the variation in volume fraction induced by the gravitational field is sufficiently wide to include the boundaries of one or more equilibrium phase transitions, then (liquid) crystal phases are expected in the sediment. Due to polydispersity and charge on the colloids, an extended equilibrium sedimentation profile is expected for experimental systems [106].

Using Eq. 4.6, the number of layers can be estimated that is necessary to reach the pressure needed for the bottom layer to undergo a phase transition, as was done for spheres in reference [65]. To do so, we assume that the volume fraction of the entire sediment is constant. Equation 4.6 then becomes:

$$\Pi = g(\rho_s - \rho_c)V_{rod} \rho d N, \quad (4.7)$$

with ρ the density of the sediment, d the thickness of one layer and N the number of layers. Coexistence pressures and densities were calculated by computer simulations, and can be found for instance in reference [96]. For a system of our typical rods, the coexistence pressure for the isotropic to nematic transition is $2.8 \cdot 10^{-2} \text{ N/m}^2$, with a coexisting density of $0.45 \rho_{cp}$ (ρ_{cp} is the density at close packing). According to Eq. 4.7, 6.8 layers of the coexisting density are needed for the bottom layer to become nematic. Equivalently, 7.4 layers are needed for nematic to smectic transition ($\Pi = 3.6 \cdot 10^{-2} \text{ N/m}^2$, $\rho = 0.53 \rho_{cp}$) and 9.5 layers for the smectic to crystalline transition

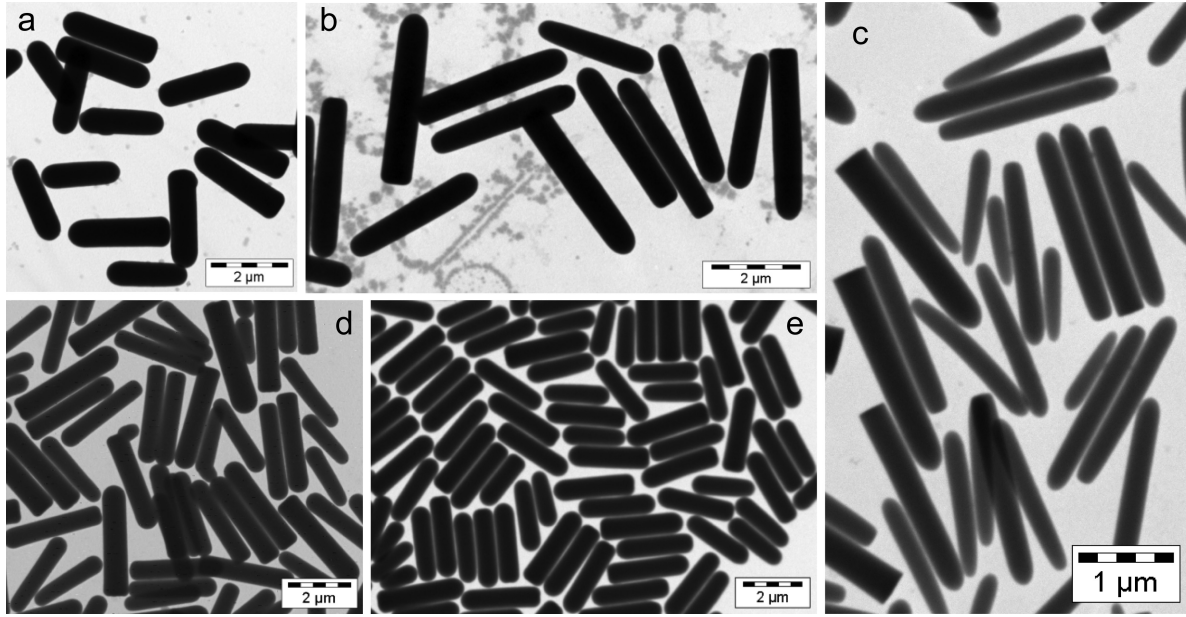


FIGURE 4.2. TEM images of the systems of silica rods that were used in this chapter. (a) B31. (b) B35. (c) B36. (d) N51. (e) B48. The dimensions of the rods are listed in Table 4.1.

($\Pi = 5.8 \cdot 10^{-2} \text{ N/m}^2$, $\rho = 0.68 \rho_{cp}$). This rough approximation is helpful to estimate the experimental conditions required for the formation of different phases.

4.3. EXPERIMENTAL

4.3.1. Dispersions

The properties of the systems that were used for the SAXS and CLSM measurements are summarized in Table 4.1. All rods, which are shown in Fig. 4.2, were prepared as described in Chapter 2 and 3. The systems B31 and B35 consist of a non-fluorescent core, a 30 nm fluorescein isothiocyanate (FITC) labeled inner shell and a 190 nm non-fluorescent outer shell. The rods of B36 were not coated after synthesis. Systems B48 and N51 consist of a rhodamine isothiocyanate (RITC) labeled core and a 175 or 150 nm non-fluorescent shell, respectively.

For the diffusion measurements in the smectic phase, a system of rods with length $L = 1.4 \mu\text{m}$, diameter $D = 280 \text{ nm}$ and polydispersities of $\sigma_L = 6\%$ and $\sigma_D = 10\%$ was used. This system was coated with a 20 nm FITC-labeled layer only. For single particle observation, a system of FITC labeled rods of $L = 2.2 \mu\text{m}$, $D = 340 \text{ nm}$, $\sigma_L = 10\%$ and $\sigma_D = 15\%$ was mixed with a system of unlabeled rods of $L = 2.1 \mu\text{m}$, $D = 250 \text{ nm}$, $\sigma_L = 9\%$ and $\sigma_D = 17\%$. The ratio of labeled to unlabeled particles was 1:100.

Particle size distributions were determined by transmission electron microscopy (TEM), using a Technai 10 or 12 electron microscope (FEI company). The average length $\langle L \rangle$ and diameter $\langle D \rangle$ of the rods, as well as their standard deviation δ , were measured

	L	σ_L	D	σ_D	L/D	φ	l_g
B31	2.37	10%	640	7.5%	3.6	0.10	0.7
B35	3.3	10%	550	11%	6.0	0.10	0.7
B36	1.9	15%	235	17%	8.0	0.128	6.5
B48	2.6	8.5%	630	6.3%	4.1	0.10	0.7
N51	2.66	10%	530	6.3%	5.0	0.105	0.9

TABLE 4.1. Properties of the systems of colloidal rods that were used in this chapter. Here, L is the length of the rods in μm , D the diameter in nm, σ the polydispersity, φ the volume fraction and l_g the gravitational height in μm .

using iTEM imaging software. The polydispersity is defined as $\sigma_L = \delta_L / \langle L \rangle$. For each sample 50 to 100 particles were measured.

The solvent mixture of all systems consisted of dimethylsulfoxide (DMSO, $\geq 99.9\%$, Sigma-Aldrich) and ultrapure water (Millipore system). The particles were dispersed in DMSO first, after which water was added until the refractive index was matched by eye. This resulted in a 10/0.85 volume ratio of DMSO/water ($n = 1.47$).

4.3.2. Confocal microscopy

Confocal microscopy measurements were performed with a Leica SP2 or a Nikon C1 confocal, of which the Nikon was used to study samples that were positioned in a vertical position (gravity along the length of the capillary). The dispersions were studied in capillaries of 1 or 2 mm wide and 0.1 mm high with glass walls of about 100 μm thick (Vitrotubes). The capillaries were sealed with candle wax first and two-component epoxy glue (Bison Kombi rapide) on top of that. This way the capillaries stayed sealed for months.

The coordinates of the rods in confocal microscopy images in which the rods were oriented perpendicular to the plane of view (so that they look like spheres in the image, see for instance Fig. 4.10) were obtained by a method similar to that of Crocker and Grier [107]. For the calculation of the radial distribution function, the code of Crocker, Grier and Weeks was used as can be found on <http://www.physics.emory.edu/~weeks/idl/>.

4.3.3. X-ray experiments

Small angle X-ray scattering (SAXS) measurements were performed at the DUBBLE beamline of the European Synchrotron Radiation Facility (ESRF, Grenoble, France). Flat glass capillaries (Vitrocom) with internal dimensions of $0.1 \times 1 \times 100 \text{ mm}^3$ were filled with several dispersions of rods (see Table 4.1). The glass thickness of these capillaries is about 100 μm . The capillaries were closed by melting the ends and covering them with two-component epoxy glue (Bison Kombi rapide) to ensure full closure. After

filling, the capillaries were kept in a vertical position to allow the establishment of a sedimentation equilibrium profile. The samples were prepared in a period of three weeks before measuring. For these measurements the microradian resolution setup was used as described in [108]. Here, a CCD detector (Photonic Science Ltd) with pixel size $9 \times 9 \mu\text{m}$ was placed at a distance of 7.4 m from the sample. The selected wavelength of the X-rays was 0.095 nm. The intensity profiles shown in Figs 4.5 etc. were calculated by integrating over a circular sector containing the area of interest in the scattering patterns.

X-ray microscopy experiments were performed at the Micro-optics Test Bench, beam-line ID06 (ESRF). The X-rays were generated with an undulator, the source size was about $20 \mu\text{m}$. The distance from the source to the sample was 56 m. An energy of 12 keV was selected with a double crystal monochromator using Si(111) crystals. Two sets of compound refractive lenses (CRL) were used as a condenser and an objective in the microscopy setup [109–111]. The condenser consisted of 19 Be parabolic CRLs with an apex radius of $200 \mu\text{m}$ and was placed at a distance of 54.3 m from the source. The objective consisted of 50 Be CRLs with an apex radius of $50 \mu\text{m}$ and was placed at a distance of 56.2 m from the source. The magnification of the setup was around 17 and the depth of field around 2 mm. The image was recorded by a CCD detector with $\sim 0.28 \mu\text{m}^2$ pixel size.

4.4. RESULTS AND DISCUSSION

4.4.1. General observations for sedimenting rods

Silica rods that are dispersed in a DMSO/water mixture sediment because the density of silica is higher than that of the solvent (1.9 g/ml compared to 1.1 g/ml). The time-scale at which the sediment is formed depends on the dimensions of the rods. The general observations described in this section were done using a typical system of rods with $L = 1.9 \mu\text{m}$ and $D = 420 \text{ nm}$ in a 6 cm high capillary with an initial volume fraction of 0.2. Photographs of this sample are shown in Fig. 4.3. In these photographs the sediment on the bottom of the capillary is shown after several sedimentation times. The dark area at the bottom is caused by a drop of glue, which covers the lowest 5 mm of the capillary and deflects the light from the white-light source that illuminates the sediment from behind. The fact that the dark area seems to extend to higher parts of the sample after 16 and 18 days is probably caused by a difference in the angle of illuminating and/or photographing the sample.

From Fig 4.3 we calculated the sedimentation velocity v_{sed} by measuring the position of the interface (indicated by the upper dashed line) in time. Following Eq. 4.4, a theoretical v_{sed} of $6.5 \mu\text{m}/\text{min}$ was calculated in the dilute limit for hard rods. Experimentally, we measured a decreasing v_{sed} of $0.20 \mu\text{m}/\text{min}$ for day 11 to 14, to $0.17 \mu\text{m}/\text{min}$ for the next two days and $0.06 \mu\text{m}/\text{min}$ for day 16 to 18. The lower

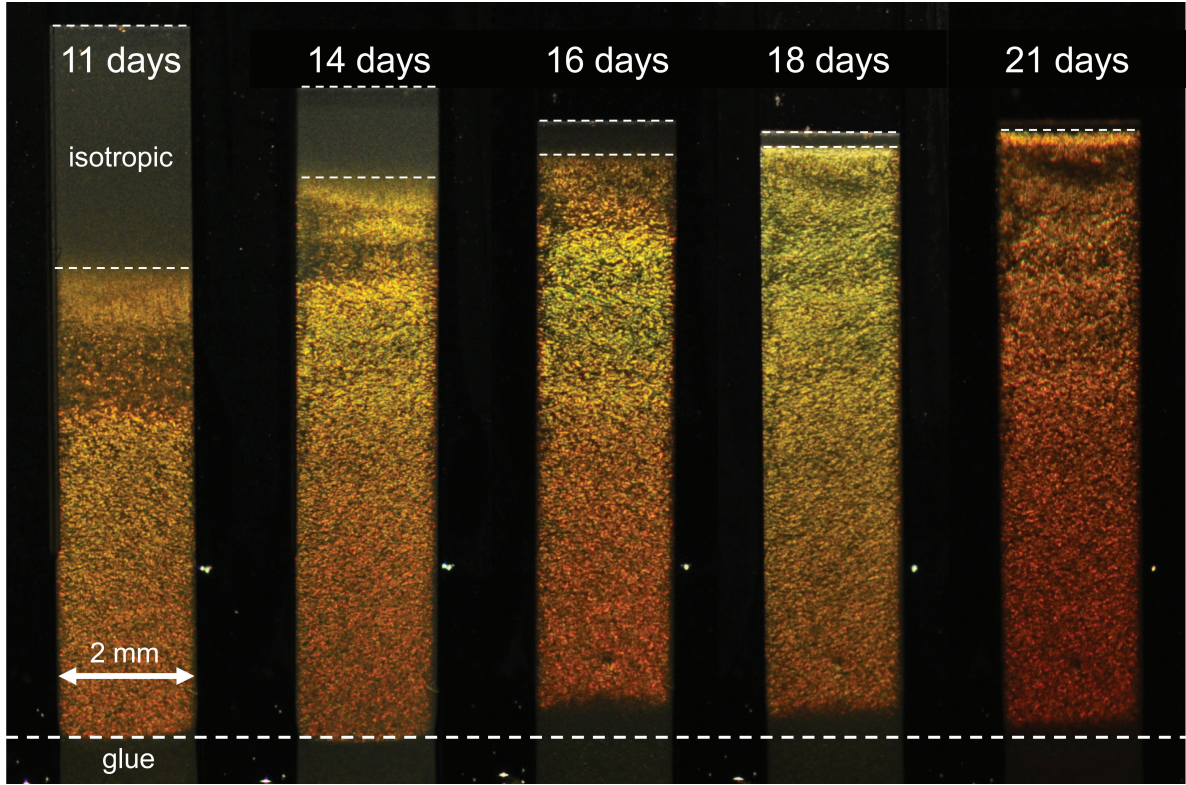


FIGURE 4.3. A sedimenting sample of $L = 1.9 \mu\text{m}$, $D = 420 \text{ nm}$ rods followed in time. Photographs were taken while illuminating the sample with white light from behind. After several days, a Bragg-reflecting ordered region formed in the bottom of the sample. In time, this region grew, while the interface between suspension and supernatant came down, indicating that rods are still sedimenting. After about 20 days the ordered region almost touched the interface, which stayed stable for the next weeks.

experimentally measured v_{sed} as well as its decrease in time is caused by the increasing volume fraction in the sediment [105].

The second dashed line from above in Fig. 4.3 denotes the interface between a region that shows Bragg reflections (layered phase) and a region that does not (isotropic phase). Bragg reflections occur when there is a periodicity present in the sample, so they are an indication of order. The first Bragg reflections were observed after 5 days of sedimentation. The formation of this ordered phase was initially faster than the sedimentation velocity (0.36 compared to $0.20 \mu\text{m}/\text{min}$ from day 11 to 14). The following days this region grew until it filled almost the whole sediment (after 21 days). Note that the density of Bragg reflecting areas in this phase changed in time; the top part of the Bragg reflecting area after 11 days showed less reflections than the same part of the sample after 14 days. The formation of ordered region thus continued for several days.

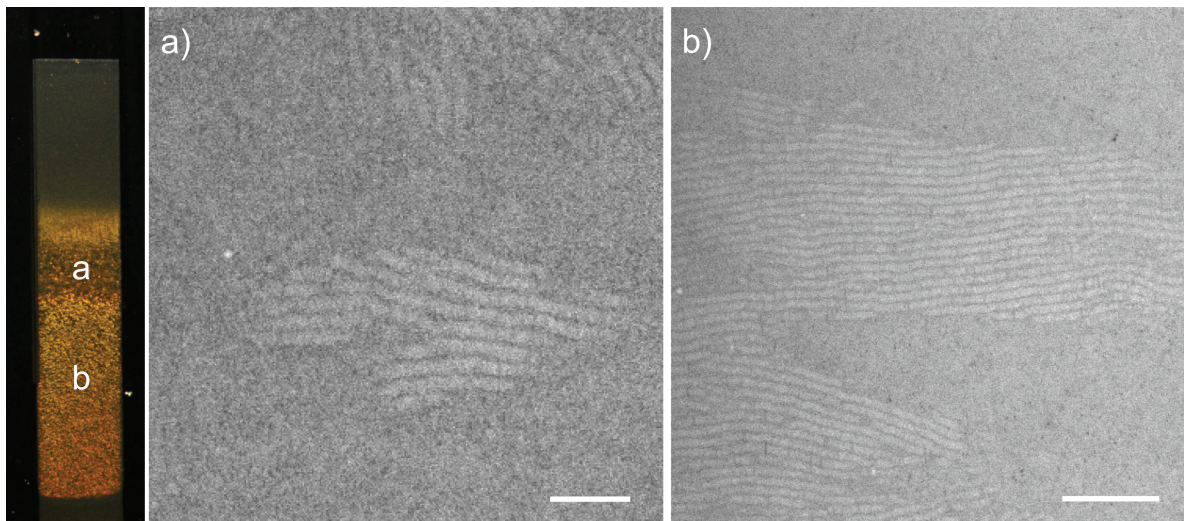


FIGURE 4.4. Confocal microscopy images of the Bragg reflecting areas shown in Fig. 4.3. (a) Top part of the sediment with small layered domains. Scale bar indicates $10\ \mu\text{m}$. (b) Bottom part of the sediment with large layered domains. Scale bar indicates $20\ \mu\text{m}$.

The origin of the Bragg reflections was found by confocal microscopy (Fig. 4.4). In the area of little Bragg reflection, small layered domains were found with dimensions of 20 to $50\ \mu\text{m}$ in diameter and around 5 layers deep. Towards the bottom, where we see more and stronger Bragg reflections, these areas increased to hundreds of microns and around 20 layers deep. The Bragg reflections thus result from the layered structures inside the sample. The fact that these do not span the whole capillary is due to the increasing concentration and multiple crystallization nuclei. Sedimentation is so fast that rotational and translational diffusion that facilitate ordering are hindered by the increasing density of the sample.

4.4.2. Sediments of rods studied by SAXS and CLSM

The phases in sediments of rod-like colloids with aspect ratios ranging from 3.6 to 8.0 were studied in more detail by SAXS and CLSM. Based on the computer simulations for the HSC-system, a smectic liquid crystalline phase is expected for rods with an aspect ratio higher than 4.1 , and a nematic phase for aspect ratios higher than 4.7 . Whether or not these phases are formed depends furthermore on the volume fraction of rods in the sample. Since the volume fraction in a sediment of rods ranges from high on the bottom to low on top, multiple phases can be observed in one capillary [112].

The sediment of the system with the largest aspect ratio ($L/D = 8.0$) shows an isotropic phase of about $0.5\ \text{mm}$ high, followed by $3\ \text{mm}$ of nematic phase and a smectic phase in the bottom $11\ \text{mm}$. SAXS patterns of these phases are shown in Fig. 4.5a-c. The scattering pattern of the isotropic phase shows weak signs of a preferable orientation. This is caused by the size of the beam, which is roughly equal

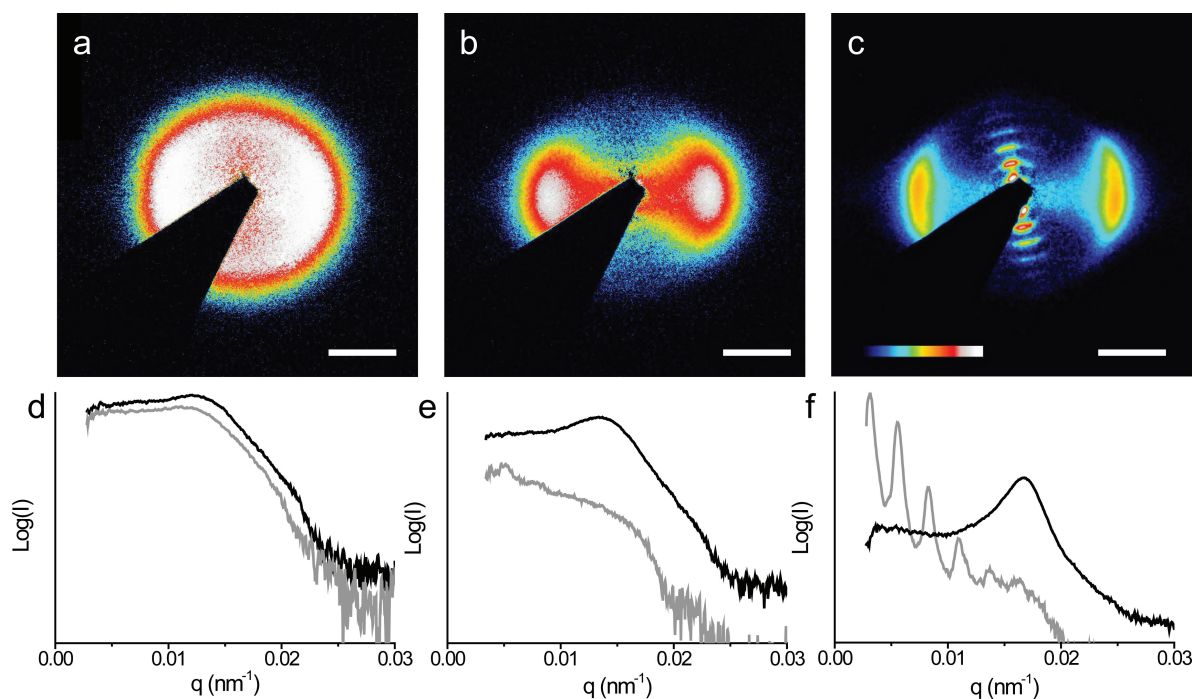


FIGURE 4.5. SAXS measurements of a sediment of $L/D = 8.0$ rods. (a) Scattering pattern of the isotropic phase on a log-scale at a height of 14 mm from the bottom of the sample. (b) Scattering pattern of the nematic phase at a height of 12 mm. (c) Scattering pattern of the smectic- C phase at a height of 9 mm. (d) Intensity profile of the pattern shown in a in the horizontal (black) and vertical (grey) direction. (e) Intensity profile of the pattern shown in b. (f) Intensity profile of the pattern shown in c. Scale bars of a, b and c indicate 0.01 nm^{-1} . The colored bar shows the calibration from 0 (black) to high (white) intensity on a log-scale.

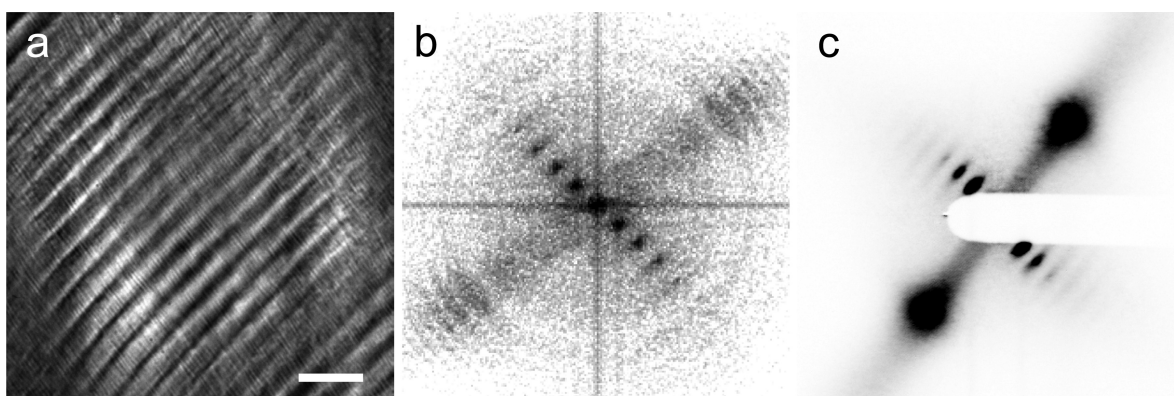


FIGURE 4.6. (a) Hard X-ray microscopy image of $L/D = 8.0$ rods in a smectic- C phase. Scale bar indicates $10 \mu\text{m}$. (b) Fourier transform of the image shown in a. (c) Scattering pattern of the same sample.

to the height of the isotropic phase. Therefore, part of the nematic phase was also hit while imaging the isotropic phase. For the nematic phase, the intensity profile of the SAXS pattern shows one broad peak that corresponds to the liquid-like ordering of the sample on the diameter scale (Fig. 4.5e), while no correlations were found in the length direction of the rods. Intensity profiles of the SAXS patterns of the smectic phase show very sharp peaks, up to the sixth order, due to diffraction from the layers of this phase that have a spacing of $2.4 \mu\text{m}$. Within the layers, one broad and much weaker peak shows the liquid-like ordering of the rods (Fig. 4.5f). In this sample, the peaks originating from correlations in length are not oriented exactly perpendicularly to the peaks originating from correlations in diameter. This implies that the system formed a smectic-*C* phase, in which the rods within the layers are oriented at an angle of about 12° with respect to the layer's normal. It is unclear whether this is caused by gravitational compression or something else.

Since the $L/D = 8.0$ rods were not fluorescently labeled, there are no real-space confocal microscopy images of this system available. A good impression of what the system looks like in real-space is given by hard X-ray microscopy. Figure 4.6 shows an X-ray microscopy image and its fourier transform, which shows good correspondence with the SAXS pattern that was measured at the same spot shown in Fig. 4.6c. Also in this sample, an angle of $\sim 12^\circ$ was measured between the orientation of the rods and the layers.

For slightly shorter rods ($L/D = 6.0$), all three liquid crystal phases were found as well (Fig. 4.7), but in this case also a phase that shows order within the layers was observed. In the bottom 11 mm of this sample a layered phase was found that shows stronger correlations within the smectic layers than the rods of $L/D = 8.0$. Three peaks were found at relative distances of 1, 1.8 and 2.8. These peaks suggest hexagonal ordering of the rods within the layers. For a perfect 2D hexagonal lattice, peaks are expected at relative distances of 1, $\sqrt{3}$, 2, $\sqrt{7}$ and 3. An explanation for the experimentally found distances is offered by the merging of the $\sqrt{3}$ -peak and the third order peak due to broadening, as well as the $\sqrt{7}$ and fifth order peak. The hexagonal pattern was also observed in a study on *fd*-virus [113]. The merging of the peaks is probably caused by the polydispersity of the sample, causing small variations in inter-particle distances. Because of its hexagonal order, we identify this phase as a smectic-*B* phase.

On top of the smectic-*B* phase, a 3 mm high smectic-*A* phase was found (Fig. 4.7c,g,l). The peaks in the intensity profile of this phase are broader than those of the phase below, representing the more liquid-like ordering of this phase. The peaks that result from periodicities along the length of the rods are less well defined than those in the sample of longer rods. This corresponds well to the real-space measurements of this sample depicted in Fig. 4.7l, which show that the layers are not ordered very nicely on top of each other.

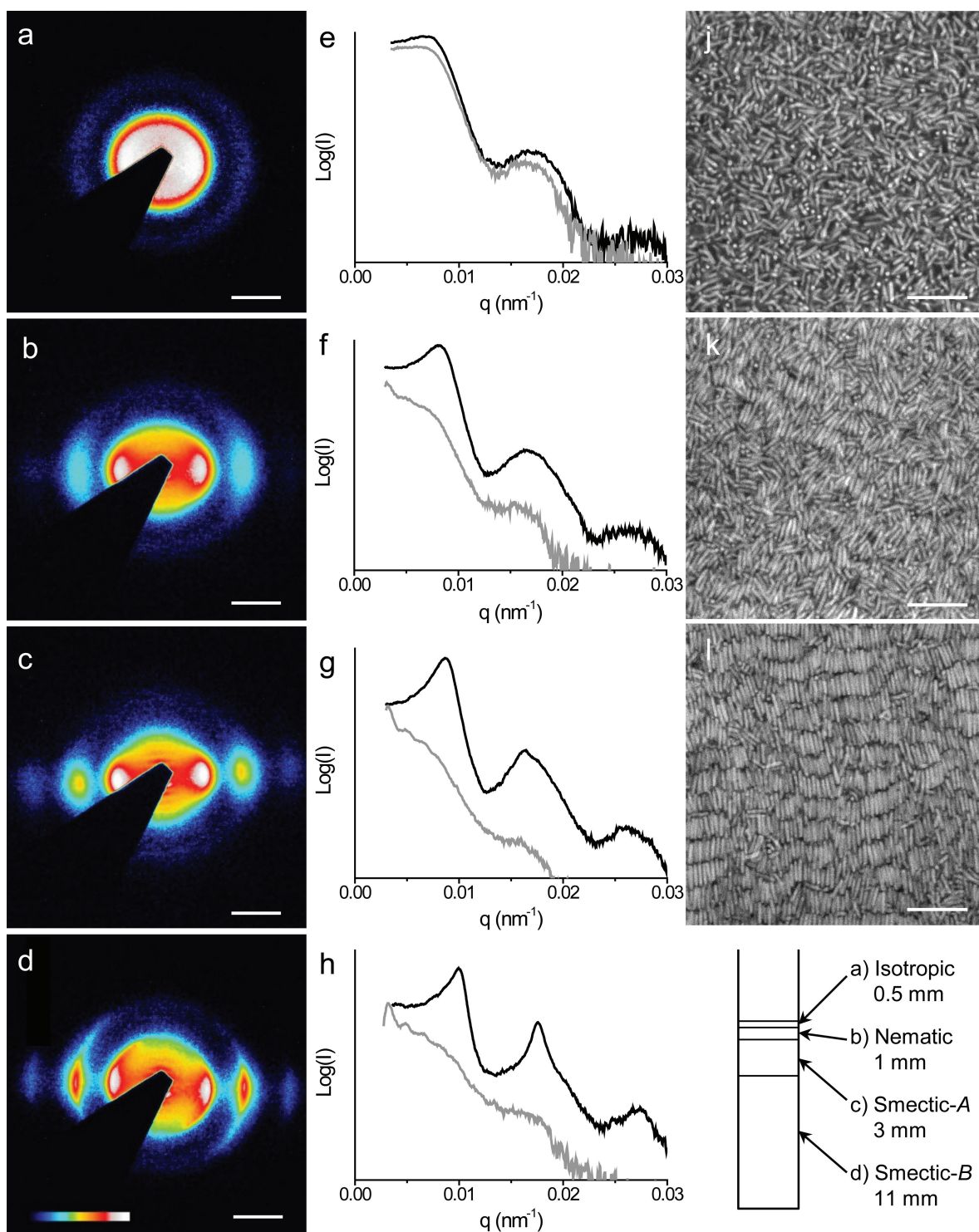


FIGURE 4.7. SAXS measurements of a sediment of $L/D = 6.0$ rods. (a-d) SAXS patterns on a log-scale of the isotropic, nematic, smectic-A and smectic-B phase, respectively. Scale bars are 0.01 nm^{-1} . (e-h) Intensity profiles of the patterns shown in a-d in the horizontal (black) and vertical direction (grey). (j-l) Confocal microscopy images of the isotropic, nematic and smectic phase of the same sample. Scale bars indicate $10 \mu\text{m}$. The colored bar shows the calibration from 0 (black) to high (white) intensity on a log-scale.

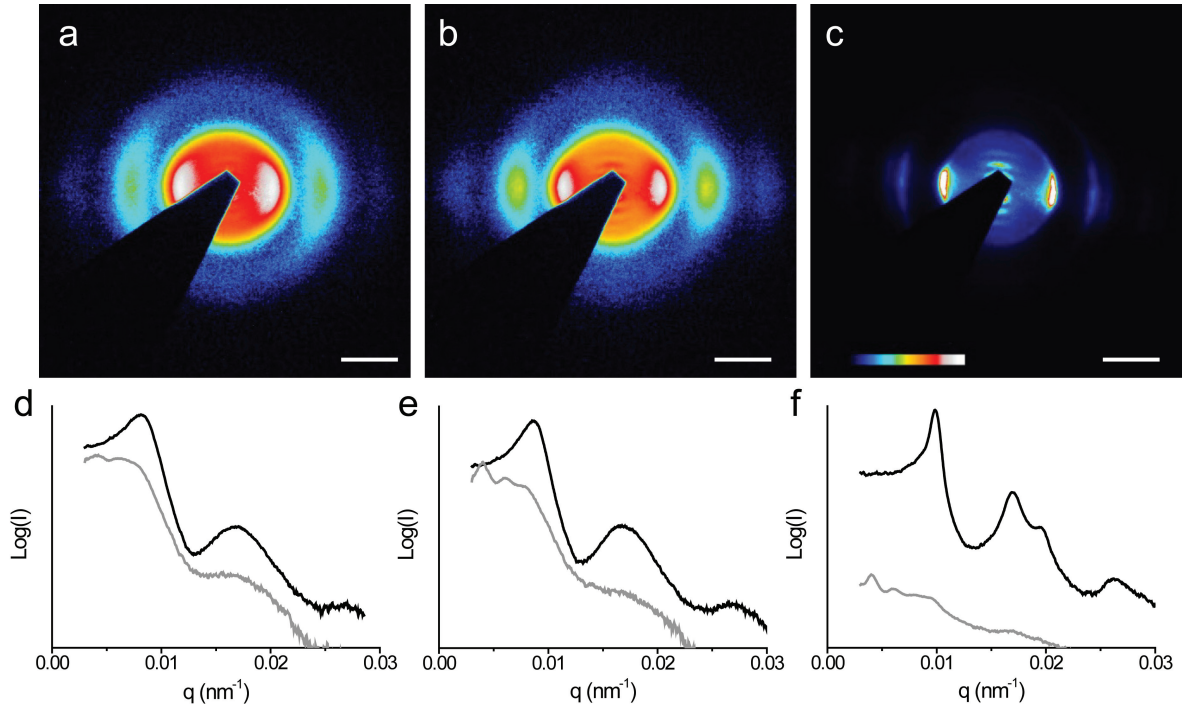


FIGURE 4.8. SAXS measurements of $L/D = 5.0$ rods. (a-c) Scattering patterns of the nematic, smectic and smectic- B phase, respectively. (d-f) Intensity profiles of the patterns shown above in the horizontal (black) and vertical direction (grey). Scale bars indicate 0.01 nm^{-1} . The colored bar shows the calibration from 0 (black) to high (white) intensity on a log-scale.

Higher up in the sample, a 1 mm high nematic phase was found (Fig. 4.7b,f,k). This phase also shows more correlations than the nematic phase of the longer rods: two peaks were found that correspond to correlations on the diameter scale. Compared to the layered phases of this sample, the peaks are broader, which indicates that there are more variations in inter-particle distances and liquid-like order. The real-space confocal microscopy image of the nematic phase (Fig. 4.7k) shows the origin of the second peak: the rods showed a beginning of ordering into rows. Peaks that are caused by periodicities along the length of the rods are absent, which distinguishes the nematic from the smectic phase.

In the about 0.5 mm high isotropic phase that was found above the nematic all liquid crystalline order disappeared, represented by the isotropic scattering and the broad peaks of Fig. 4.7a and e. Very weak correlations are still present, as indicated by the small second order peak, but these cannot be found in the real-space image (Fig. 4.7j).

The more monodisperse system with $L/D = 5.0$ shows even stronger signs of hexagonal ordering (Fig. 4.8). The scattering pattern of this phase shows strong, sharp peaks for correlations within the layers that are spaced at relative distances of 1 (for the first

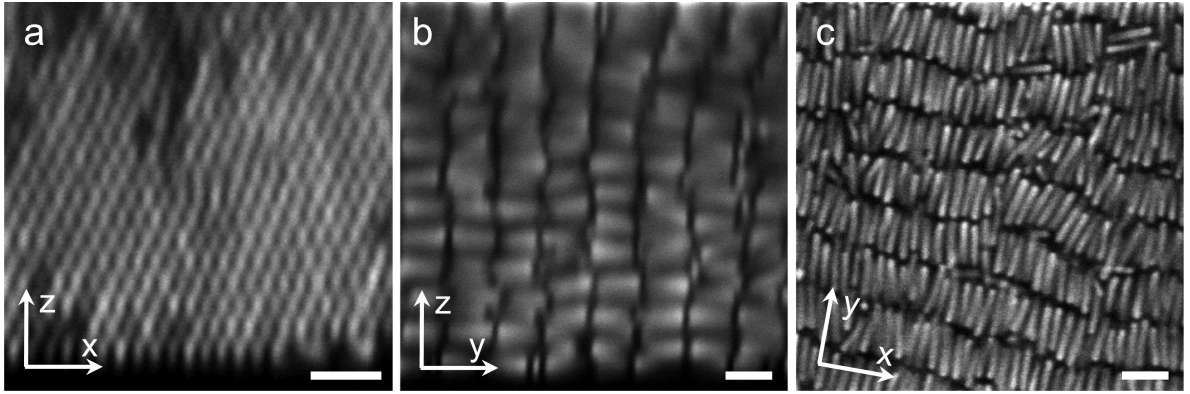


FIGURE 4.9. Confocal microscopy images of hexagonally ordered layers in a sediment of $L/D = 5.0$ rods through different planes. Scale bars indicate $3 \mu\text{m}$.

peak), $\sqrt{3}$, 2, $\sqrt{7}$ and 3, which indicates that the rods are hexagonally ordered within the layers. This is confirmed by confocal microscopy images of the phase. Figure 4.9 shows the hexagonal layers from the top and two sides. Due to the lower resolution of the confocal microscope in the z -direction, the rods seem stretched in this direction (see Section 3.3.3). The hexagonal order within the layers is clearly visible in Fig. 4.9a. A cut through the xy -plane shows disorder in the stacking of the layers themselves, which is expressed in broad and small peaks originating from correlations on the length-scale of the rods in the SAXS pattern. Although these observations hint towards a crystalline phase, no peaks due to correlations between the hexagonal patterns of subsequent layers were found, which excludes that the structure is fully crystalline. Therefore, we identified the structure as a smectic- B phase. Higher up in this sample we found first the smectic and finally the isotropic phase, but not a nematic.

For the system of rods with the shortest aspect ratio ($L/D = 3.6$), hexagonally ordered rods were found in domains that extended tens of microns, as shown in Fig. 4.10a. The degree of hexagonal order in these layers is shown in Fig. 4.10b, which shows the 2D radial distribution function of the rods compared to that of a perfect 2D hexagonal lattice. The experimental peaks were scaled to fit the first peak of the theoretical $g(r)$ and extend over 10 particle diameters, comparing well to the $g(r)$ of the perfect lattice. The average distance between the centers of the rods was 910 nm, while the diameter measured by TEM was 640 nm. The difference is caused partly by the negative charge on the silica rods, causing repulsive interactions, and partly by the fact that these measurements were not performed at the densest packing. The degree of hexagonal order in the sample was quantified by the 2D local hexagonal bond orientational order parameter Ψ_6 [114]:

$$\Psi_6(r_j) = \frac{1}{N} \sum_k \exp(i6\theta(r_{jk})) \quad (4.8)$$

where k runs over all N neighboring particles of particle j and $\theta(r_{jk})$ is the angle

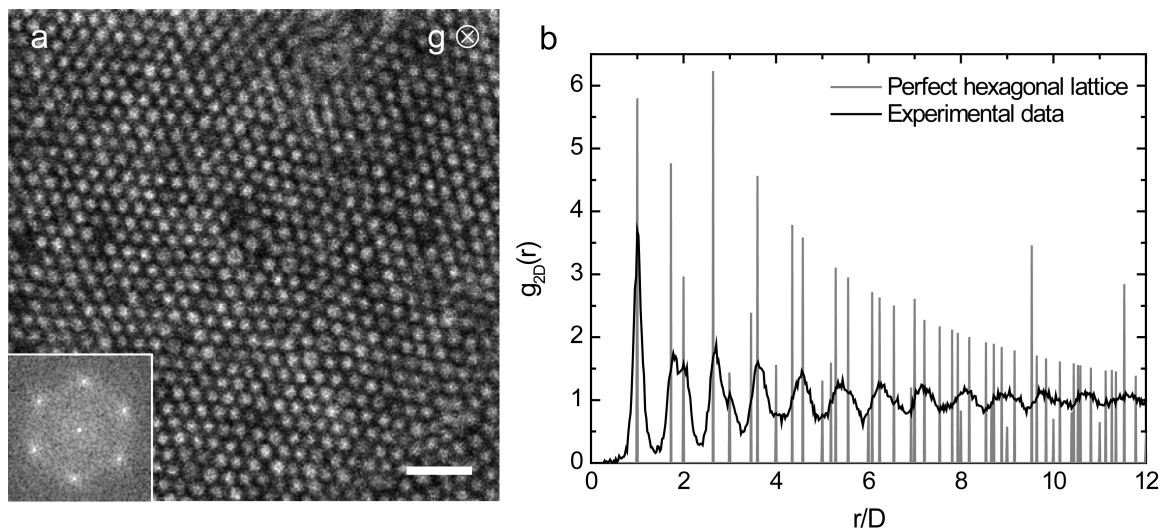


FIGURE 4.10. (a) Confocal microscopy image of short rods ($L/D = 3.6$) sedimented in a flat capillary. Large areas of hexagonally ordered rods are visible. In the inset a fourier transform of the image is shown. Scale bar indicates $5 \mu\text{m}$. (b) 2D Radial distribution function of a hexagonally ordered sheet of rods in black. The equivalent for a perfect hexagonal lattice is shown in grey.

between the vector between particles j and k and a fixed reference axis. The value of $|\Psi_6|$, which is a number between 0 (no order) and 1 (perfectly crystalline), gives the degree of hexagonal order in the image. In the crystalline sheets that were found in sediments of short rods, Ψ_6 was around 0.75. Confocal images of larger areas are needed to determine whether the ordering in these samples is really hexagonal or hexatic. Figure 4.10a further shows the fourier transform of the confocal image, in which six peaks corresponding to hexagonal ordering are visible. This image corresponds well to the SAXS patterns of the sample, which shows six peaks spaced at approximately 60 degrees up to two scattering orders (Fig. 4.11). Although in most of the sample the layers were oriented with rods parallel to the wall of the capillary, we were able to find some domains with the rods perpendicular to the wall, as in Fig. 4.11a. The crystalline phase continued higher up in the sample until the scattering pattern of an isotropic phase was seen. Smectic- A or nematic phases were not observed in the $L/D = 3.6$ sample.

4.4.3. Phase diagram

The measurements that were described in the previous section can be summarized in a rough phase diagram (Fig. 4.12). To estimate the volume fractions of the phases that were observed, inter-particle distances L_s and D_s were determined at different heights in the capillary from the SAXS measurements. Subsequently, the volume fractions of the

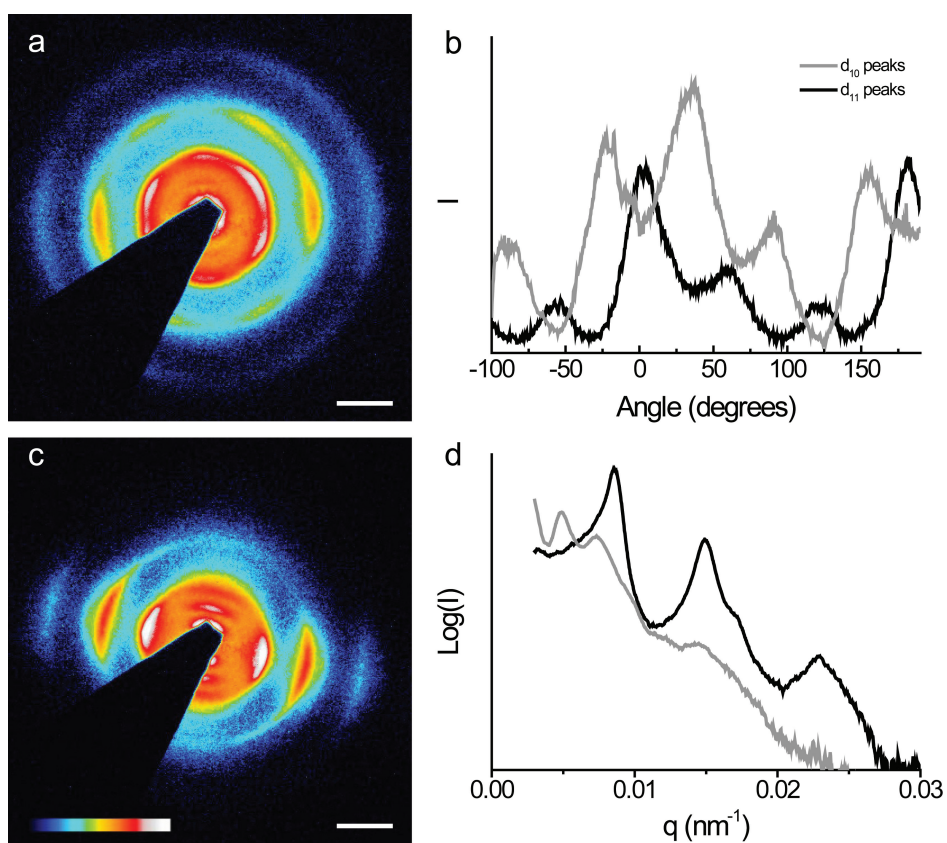


FIGURE 4.11. SAXS pattern of hexagonally ordered rods in two orientations. (a) Rods perpendicular to the capillary wall. (b) Rods parallel to the capillary wall. (c) Intensity profile of the hexagonal peaks integrated over the circles shown in a. (d) Intensity profiles of the pattern shown in b. Scale bars indicate 0.01 nm^{-1} . The colored bar shows the calibration from 0 (black) to high (white) intensity on a log-scale.

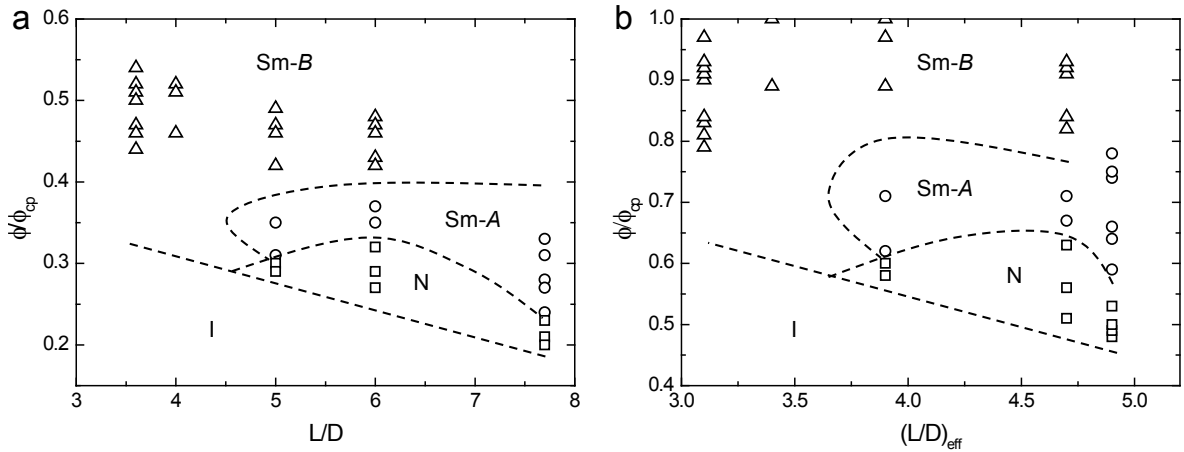


FIGURE 4.12. (a) Experimental phase diagram for rods depending on aspect ratio and density. The volume fractions of the smectic- B phase are depicted as triangles, circles denote the smectic- A phase and squares the nematic phase. Lines were drawn as a guide to the eye. (b) Phase diagram corrected for repulsions due to charges by taking an effective diameter and length into account.

different phases were calculated as follows. In the smectic- B phase, the volume fraction was calculated by dividing the volume of the rods that was measured by TEM (Eq. 4.5) by the available volume per particle measured by SAXS: $\frac{1}{2}\sqrt{3}D_s^2L_s$. For the smectic- A phase there is no hexagonal order between the rods and the available volume per particle was estimated by $D_s^2L_s$. In case of a nematic, the extra distance along the length of the rods was assumed to be equal to the calculated difference for the diameter. In order to compare this experimental data with computer simulations, the volume fractions were normalized with respect to the volume fraction at close packing φ_{cp} . Since there were no correlations found between neighboring layers, we assumed $\varphi_{cp} = \frac{\pi}{2\sqrt{3}}(1 - \frac{D}{6L})$ (hexagonally close-packed rods in one layer). The resulting experimental phase diagram is shown in Fig. 4.12a.

Our experimental results show many similarities with the phase diagram that was computed by Bolhuis and Frenkel (Fig. 4.1 and reference [96]). Isotropic phases were found at low volume fractions, and for higher volume fractions, nematic and smectic phases were found. At the highest volume fractions, however, Bolhuis and Frenkel found a crystalline phase, while we identified our phase as a smectic- B phase. These phases are actually very much alike. The difference between the two is the presence (for the crystal) or absence (for the smectic- B) of correlations between subsequent layers [9]. Since we did not find proof of correlations between the layers, we refer to the structure as smectic- B . The formation of a smectic- B in stead of a full crystalline phase is probably caused by the polydispersity of the systems used (around 10%). Also similar to the simulations, the isotropic-nematic phase boundary of the experimental phase

	Hard rod dimensions			Effective rod dimensions		
	L	D	L/D	L_{eff}	D_{eff}	$(L/D)_{eff}$
B31	2.37	640	3.6	2.56	830	3.1
B35	3.3	550	6.0	3.49	740	4.7
B36	1.9	235	8.0	2.1	430	4.9
B48	2.6	630	4.1	2.8	830	3.4
N51	2.66	530	5.0	2.86	730	3.9

TABLE 4.2. Hard rod dimensions as measured by TEM and effective rod dimensions as measured by SAXS. Here, L is the length of the rods in μm , D the diameter in nm, and L/D the aspect ratio.

diagram shows the same trend with respect to the aspect ratio: the volume fraction at which the transition occurs decreases with increasing aspect ratio. Furthermore, smectic and nematic phases were found only at aspect ratios of 5 and higher, which is in correspondence with the simulations that predicted nematics for $L/D > 4.7$ and smectics for $L/D > 4.1$.

A large discrepancy between experiments and simulations was found in the volume fraction of the phases. The experimentally determined volume fractions are significantly lower than those calculated by computer simulations. This is caused by the fact that the experimental system is not a perfect hard rod system. The silica particles are negatively charged and therefore experience repulsive interactions. In literature, it was shown for silica spheres that an effective increased diameter can be used to map the results onto a hard sphere phase diagram [65]. Here, we did the same for rods. The effective diameter D_{eff} was determined by measuring the minimum inter-particle distances between the rods at the bottom of the sediment, where we assume the rods to be close packed. The effective length was assumed to be $L + D_{eff} - D$, where L and D are the hard-rod dimensions, measured by TEM. The hard-rod and effective dimensions are listed in Table 4.2 and the corrected phase diagram is shown in Fig. 4.12b. For this corrected phase diagram, the volume fractions correspond well with the simulations, but the effective aspect ratio's do not. Nematic and smectic phases occur now for aspect ratios of 3.9 and higher. Apparently, this method of correcting for the double layer, that worked well for spheres, does not map our results onto the HSC phase diagram exactly.

In literature, other examples of short rods forming smectic phases exist. Maeda *et al.*, for example, observed isotropic-smectic transitions for selenium and β -FeOOH rods of $L/D = 3.5 - 8.0$ [45,115]. Their observations for these low aspect ratios correspond well with our observations, including hexagonal ordering of the rods with $L/D = 3.5$ and side-by-side ordering in clusters before forming a smectic(-B) phase. Nematic phases,

however, were only observed for $L/D = 10 - 35$ in this study. Maeda *et al.* did not correct for repulsions or polydispersity in their work, which they claim could be the cause of the difference with the simulations, which predicted nematics from $L/D = 4.7$. In our experience, the nematic phase was hard to find by real-space measurements, because it occurs only in a small range of densities. Guided by the SAXS-measurements and being able to image 2D slices in dense sediments by confocal microscopy, we were able to find a thin layer of rods in a nematic phase (Fig. 4.7k) where they might have been missed by Maeda *et al.*, who used a standard optical microscope.

Other well known liquid crystal systems that show nematic phases, such as TMV or *fd*-virus all have larger aspect ratios than the rods studied in this chapter ($L/D < 8$). Also for boehmite rods, nematic phases were only observed for larger aspect ratios [42]. For goethite particles, nematic phases were observed for $L/D = 3.5$, but these particles are much thinner in the third dimension ($L/T \sim 10$, with T their thickness) [116].

4.4.4. Influence of the flat wall

In experimental studies of colloidal dispersions boundary effects, such as the flat wall of the cell that contains the dispersion, are always present. For spheres, it was found that the presence of a flat wall can lead to layering and eventually prefreezing of a liquid phase [117,118]. Also, the effect of a flat wall on crystallization has been studied intensively [65,119]. The effect of a flat wall on the ordering of *rods* was examined using computer simulations [120,121]. Here, it was found that a thick nematic film forms on the wall in the isotropic phase.

For our system of hard rods, we experimentally confirmed that the rods tend to align with their long axis parallel to the flat surface. In capillaries that were positioned with their flat wall to the bottom, we found that the rods always lay flat on the bottom. This resulted in layered phases that were always oriented with their layers perpendicular to the bottom plane. The influence of flat and patterned substrates on the orientation of rods is described in more detail in Chapter 7. In standing capillaries, for which the flat wall was positioned in the vertical direction, the rods were found to orient again parallel to the flat wall, pointing down this time. This orientation was found in both the confocal and the scattering data, e.g. in Fig. 4.7. Additionally, we found that the influence of the wall extended tens of microns into the sample, after which domains of random orientations of the formed phase were observed.

4.4.5. Defects in smectic phases

The appearance of the smectic-*B* phases that were found varied strongly as a function of the aspect ratio of the rods. Although there was clear hexagonal order within the layers of $L/D = 3.6$ rods, the stacking of these layers themselves was less well defined. Figure 4.13a shows that the layers formed by short rods are often single layers oriented in random directions, although sometimes a few layers are stacked. Confocal microscopy

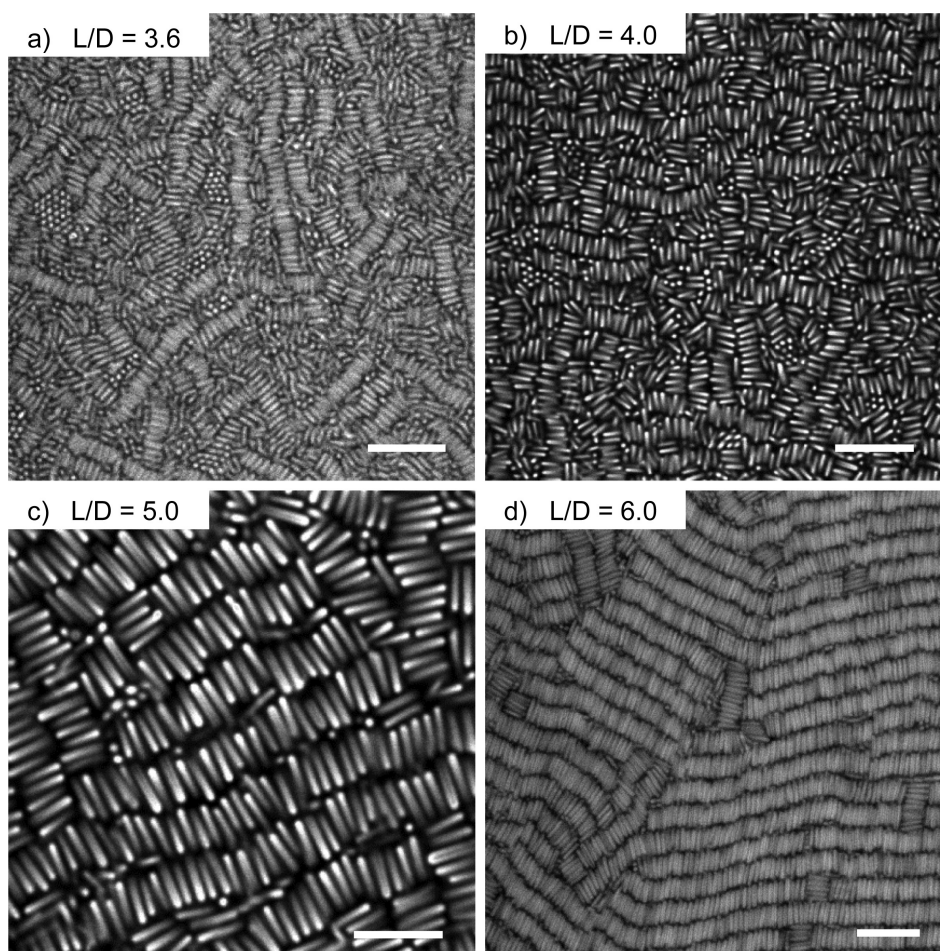


FIGURE 4.13. Typical confocal microscopy images in sediments of systems of different aspect ratios. (a) Short rods $L/D = 3.6$ form hexagonally ordered layers, without clear stacking of the layers. (b-d) Stacking improves for higher aspect ratios. Scale bars indicate $10\ \mu\text{m}$ for a,b,d and $5\ \mu\text{m}$ for c.

images show that this stacking improved with increasing aspect ratio (Fig. 4.13). This is probably caused by the fact that systems of rods with higher aspect ratios already formed layers at lower volume fractions, in smectic-*A* phase. After crystallization towards a smectic-*B* at higher densities, the configuration of those layers remained.

For high aspect ratios (> 6), layer formation went very smoothly and large domains were formed that extended over the whole sample. Defects that were found in these samples include mainly edge dislocations and splay distortions (Fig. 4.14a). In samples of shorter rods, defects were observed more frequently. Also, the domains found in these samples were smaller than for long rods. Since these rods can be studied on the single particle level, it is easier to find defects. Figure 4.14b shows three types of defects. The first type, inside circle 1, is that neighboring domains or defect layers are positioned perpendicularly with respect to each other. Inside circle 2 the ending of a layer is shown, called an edge dislocation. Both types of defects have been described for other liquid

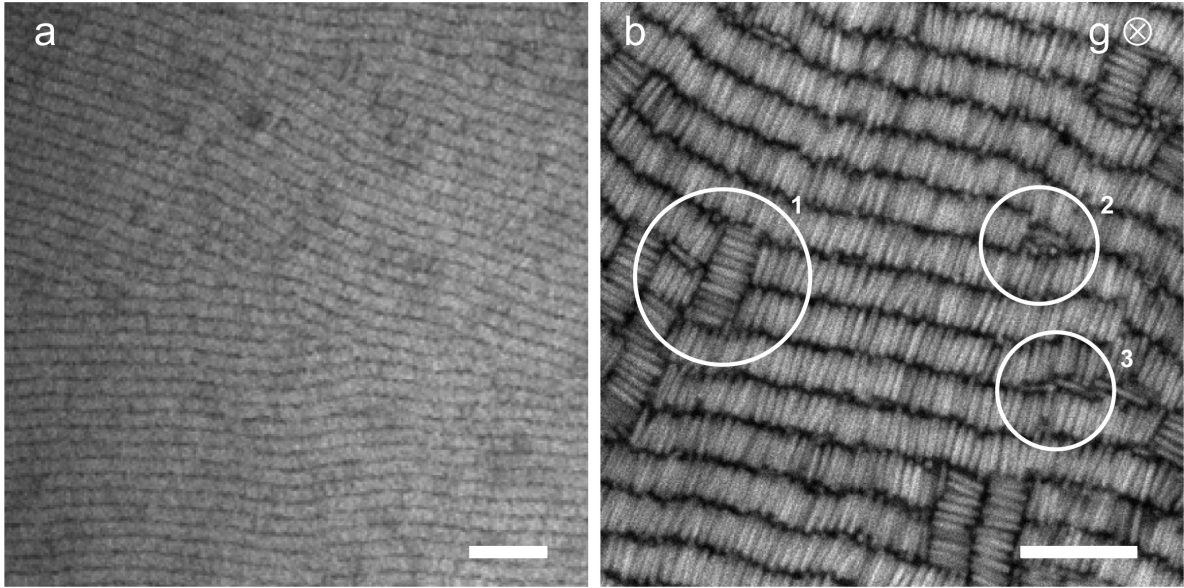


FIGURE 4.14. Confocal microscopy images showing several types of defects. (a) Edge dislocations and splay distortions in a sample with rods of aspect ratio 8.7. Scale bar is $20 \mu\text{m}$. (b) Sediment of $L/D = 6$ rods. 1) Small domain oriented perpendicular to its neighbor-domains. 2) Edge dislocation. 3) Transverse-interlayer (TI) particles. Scale bar indicates $10 \mu\text{m}$.

crystal systems [122]. The third type of defect, however, has not been observed before experimentally. This type of defect, that is called a transverse interlayer (TI) particle, is described as a rod that is positioned in between the layers of a smectic and oriented with its long axis parallel to the layers. The existence of TI-particles was predicted by computer simulations in 1995 already [123, 124], but no experimental confirmation of the phenomenon has been reported up to now. In the simulations it was found that the abundance of TI-particles depends on the smectic layer spacing λ . The simulations were done for $\lambda = 1.03$, while in our experiments $\lambda \sim 1.2$. This might explain why we found more TI-particles than expected; we found on the order of a few percent of the rods to be TI particles, while the simulations result in a fraction on the order of 10^{-5} .

4.4.6. Dynamics in the smectic-*A* phase

Beside the previously described structural aspects of the different liquid crystal phases, there are also dynamical differences. The diffusion of rods in liquid crystalline phases is greatly affected by the increased structural order. Computer simulations showed that in nematic phases the long-time self-diffusion coefficient along the director D_{\parallel} is higher than the one perpendicular to the director D_{\perp} [125]. $D_{\parallel}/D_{\perp} = 2 - 4$ near the isotropic-nematic transition and increases with increasing concentration. In a smectic, however, D_{\parallel} decreases dramatically, even below D_{\perp} . Below, we describe some preliminary observations on dynamics in a smectic phase.

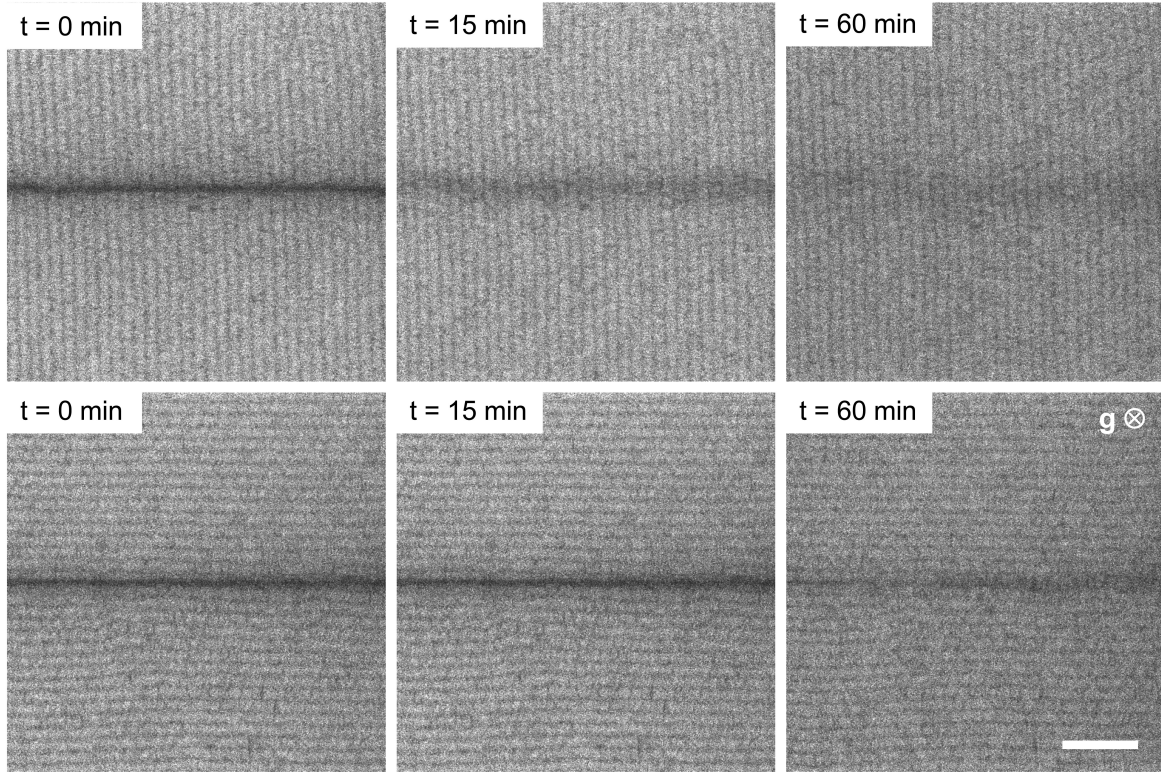


FIGURE 4.15. Diffusion of bleached particles with aspect ratio 5.0 within smectic planes (upper row) and from plane to plane (lower row). Scale bar indicates $10 \mu\text{m}$.

A dynamic difference between the smectic-*A* and the crystalline phase is that long-time self-diffusion only occurs in smectics and not in crystals. To determine whether the layered phase formed by rods with a length of $1.4 \mu\text{m}$ and a diameter of 280 nm is a smectic-*A* phase, we studied the diffusion of the rods. Due to their small diameter, single particle imaging of these rods was not possible, but the layers of the structure are clearly visible in Fig. 4.15. A $50 \times 50 \mu\text{m}^2$ plane was bleached perpendicular to the orientation of the layers by scanning this plane 10 times in short succession (Fig. 4.15 top row). In time, the bleached particles diffused to the non-bleached area and vice versa, resulting in a spread of the dark area in the images. Since there is clearly diffusion of rods, the layered phase is indeed a smectic. When a plane parallel to the layers (in other words: one of the layers) was bleached, the spreading was slower and the boundary between the bleached and non-bleached area stayed much sharper. These observations confirm the simulation results on hard spherocylinders by Löwen, who found that $D_{\perp} > D_{\parallel}$ in smectics [125]. Intuitively, this is easy to understand since the rods are ordered liquid-like inside the layers and diffusion is therefore easy. In the direction perpendicular to the layers the structure is ordered, which makes diffusion harder. However, exactly the opposite was found in diffusion studies on the *fd*-virus, where self-diffusion takes place

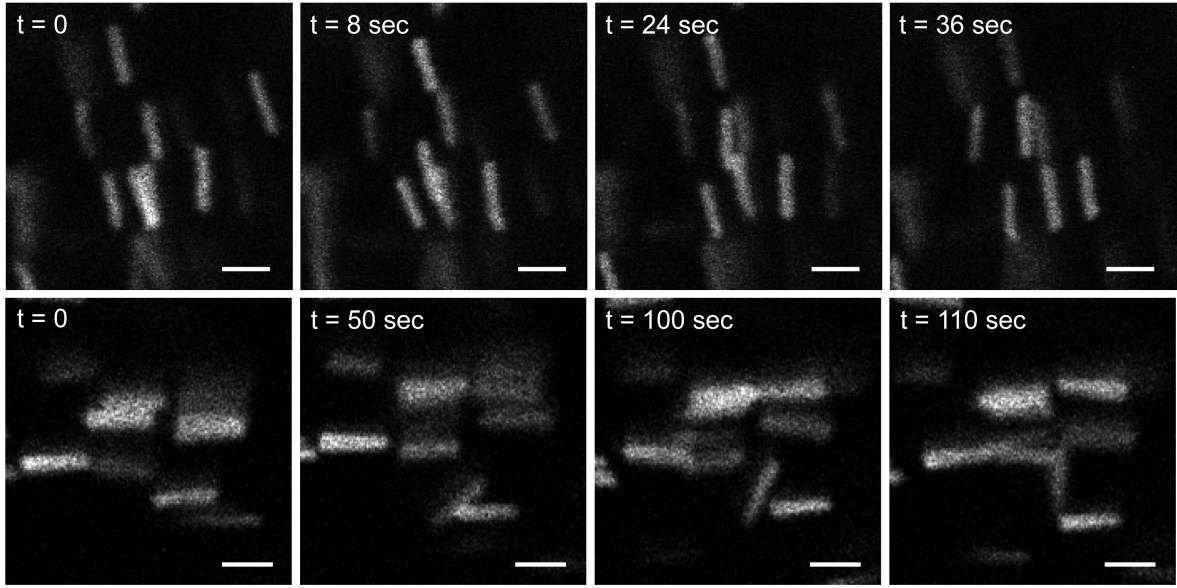


FIGURE 4.16. On a single particle level: diffusion from one smectic plane to another (upper row) and formation of an transverse-interlayer particle (lower row). Scale bars indicate $2 \mu\text{m}$.

preferentially in the direction perpendicular to the smectic layers and occurs by quasi quantized steps of one rod length [126, 127]. Possibly this is caused by the flexibility of the virus particles.

In a rough estimation from Fig. 4.15 we found $D_{\perp} \sim 0.2 \mu\text{m}^2/\text{s}$ in our system. From measurements just below the isotropic/smectic transition we found $D_{\perp} \sim 0.5 \mu\text{m}^2/\text{s}$. In comparison, diffusion coefficients on the order of $1 \mu\text{m}^2/\text{s}$ were measured in the isotropic phase of both fd-virus and silica coated boehmite rods [98, 128, 129]. In nematic phases of silica coated boehmite rods, the diffusion coefficient was $D = 0.1 \mu\text{m}^2/\text{s}$ and the D_{\parallel}/D_{\perp} ratio was only 2. For nematic phases of fd-virus, however, Lettinga *et al.* measured an increased D_{\parallel} and a decreased D_{\perp} with a ratio of D_{\parallel}/D_{\perp} increasing up to 20 for better aligned nematics. Since layering should only influence D_{\parallel} , we can compare our preliminary experimental result for D_{\perp} to that of the nematic phase, which is of the same order of magnitude.

Diffusion on the single particle level for thin rods was studied using a mixture of labeled and unlabeled rods. The labeled rods were thicker than the unlabeled rods in this case (340 and 250 nm). Sedimentation of a sample with a 1:100 ratio of labeled:unlabeled rods and an initial volume fraction 0.17 resulted in the formation of a smectic phase. In this doped system, it is possible to observe single particles with small diameters in the smectic phase. Besides diffusion within the layers, we also found more rare events like hopping from one layer to another and the transformation from normal rod to TI-particle (Fig. 4.16). The hopping from one layer to another was

studied in more detail by computer simulations [130,131], as well as by experiments on fd-virus [126].

In future experiments, we plan to focus more on measuring the dynamics to distinguish and characterize the different phases and determine whether they are metastable/glassy or not.

4.5. CONCLUSIONS

The phase behavior of rod-like silica particles was determined for aspect ratios smaller than 8 using SAXS and CLSM. The results were summarized in a phase diagram, which corresponds well with computer simulations on HSC-systems. In correspondence with the simulations, no liquid crystalline phases were found for silica rods with small effective aspect ratios. Nematic and smectic phases were found for aspect ratios of 5.0 and higher, while simulations predict nematics for $L/D > 4.7$ and smectics for $L/D < 4.1$. Instead of forming a fully crystalline phase, the rods ordered into a hexagonally ordered smectic- B phase at high volume fractions, probably due to their polydispersity. The experimentally found volume fractions of the different phases were significantly lower than those calculated by the simulations, which is caused by the negative charge on the rods. The resulting double layer increased the effective dimensions of the rods and decreased volume fraction.

Using real space techniques several types of defects in the smectic phase were found. The amount of defects decreased with increasing aspect ratio. Because the rods were imageable on the single particle level, the existence of transverse interlayer particles was observed experimentally for the first time. Also, dynamical processes such as diffusion within and between layers as well as the transition from in-layer to transverse-interlayer particle were observed. The order of magnitude of the diffusion coefficient, determined by these preliminary measurements corresponds with measurements on other rod-like colloidal systems.

4.6. ACKNOWLEDGEMENTS

We would like to thank Andrei Petukhov, Dmitry Byelov and Bart de Nijs for their help with the SAXS measurements. Furthermore, we would like to acknowledge Dmitry Byelov for the X-ray microscopy measurements.

Phase behavior of rods in an external electric field

ABSTRACT

We studied the effect of external electric fields on the behavior of colloidal rods in dilute and concentrated dispersions. In the dilute regime, the rods aligned themselves with the applied field due to an induced dipole moment. By measuring the distribution of orientations of the rods with confocal microscopy, the polarization of the rods was determined. The results can be described with a theoretical model for the polarization of ellipsoids. In more concentrated dispersions, external electric fields were used to influence the phase behavior of the rods. Para-nematic phases were induced this way, as well as well-aligned smectic phases with a decreased number of defects. At high field strengths, a new crystal structure was observed that consisted of strings of rods ordered in a hexagonal pattern in which neighboring rods were shifted by a third of their length in height.

5.1. INTRODUCTION

Colloids have proven their importance as model systems for understanding phase behavior and phase transitions [6, 132]. As a result of the unique combination of displaying the same phase behavior as atoms and molecules, but having longer time and length scales, colloids are experimentally much more accessible than atoms and molecules. Besides providing fundamental knowledge on phase behavior, the study of colloidal systems has led to numerous applications such as coatings, electronic ink and photonic crystals [29, 133, 134]. The ability to control the properties of colloidal suspensions is essential for their use in these applications. Electric fields, for example, are a perfect tool to gain control, since they are known for their ability to change the structural, rheological, dielectric and optical properties of colloidal suspensions [31, 135]. Understanding of the behavior of colloids in electric fields is thus very important to be able to influence the properties in a controlled way.

Up to now, experimental studies on colloids in electric fields have mainly focused on spheres. Nevertheless, recent results on anisotropic particles such as ellipsoids and dimers were also reported [39, 49, 136]. There is also earlier work on anisotropic particles in electric fields addressing the so-called electro-optical effect in which the electric field changes the light scattering of a dispersion [137–139]. Experimental work on colloidal rods in electric fields to change the phase behavior is much more limited. For instance, Kang *et al.* studied concentrated dispersions of *fd*-virus in electric fields [140, 141]. This group also contributed to the theoretical understanding of rods in external fields by considering the electric field induced ion distribution around the rods [142]. Computer simulations on rods in electric fields were done by Rotunno *et al.* [143]. In this work, the induced dipole moment of spherocylinders was modeled by two charges placed at the ends of the cylindrical part of the particle. The phase diagram of these rods, that obtain a dipole moment directed exclusively along their long axis, includes a new crystal phase that has not been seen before experimentally.

Rod-like molecules and particles are known for their liquid crystalline phase behavior, which has been studied extensively for molecular systems [9], but also a lot is known for colloidal systems [91, 97, 144]. The recent development of a new monodisperse colloidal system of rods, as described in Chapter 2, makes it possible for the first time to study highly concentrated dispersions on the single particle level. Using this system, we studied the influence of electric fields on the phase behavior of rods. We used high frequency fields in this work to exclude the contributions of the electric double layers and ion fluxes to the polarizability, leaving only dielectric polarization. This resulted in the observation of a new crystal structure that has not been seen before experimentally and confirms the simulation predictions of Rotunno *et al.*. In addition to finding the new phase predicted in the computational work, we were able to influence the

direction and range of ordered regions in the smectic phases described in Chapter 4. Also, para (i.e. induced by the field) smectic phases were induced for suspensions of rods with a low aspect ratio, for which no liquid crystal phases are expected based on computer simulations without a field [96]. Furthermore, in order to characterize the polarizability of our particles and connect our experiments to the simulations and theory quantitatively, we first studied the aligning effect of an electric field on single rods.

5.2. COLLOIDAL RODS IN EXTERNAL ELECTRIC FIELDS

Colloids that are placed in an external electric field obtain an induced polarization that can often be approximated well with that of an induced dipole when the dielectric constant of the particle differs not too much from that of the surrounding solvent and the field strengths are not too strong [145]. While for spherical colloids the induced dipole moment can be calculated analytically, the anisotropic shape of rods in general requires a numerical approach.

In this chapter, we will compare our results with the polarization of ellipsoids for which the result is known analytically, as described for instance in references [39, 146]. Venermo and Sihvola showed in their numerical study on the dielectric polarizability of circular cylinders that this polarizability does not differ much from the polarizability of ellipsoids of the same volume and aspect ratio [146]. They show that for aspect ratios between 0 and 10 the difference in polarization for ellipsoids and cylinders is less than 10%. Therefore, we also expect the ellipsoid model to describe our rods reasonably well, even though the shape of the rods is not actually ellipsoidal. The dipole moment of an ellipsoid in the direction of the i th axis is:

$$p_i = \alpha_i \varepsilon_s V E_i \quad \text{with} \quad \alpha_i = \frac{\varepsilon_c - \varepsilon_s}{\varepsilon_s + (\varepsilon_c - \varepsilon_s) N_i}, \quad (5.1)$$

where ε_s is the dielectric constant of the solvent, ε_c the dielectric constant of the colloid, V the volume, E_i the applied electric field and N_i the depolarization factor. If the semi-axes of the ellipsoid are given by a_x , a_y and a_z , the depolarization factor is:

$$N_x = \frac{a_x a_y a_z}{2} \int_0^\infty \frac{ds}{(s + a_x^2) \sqrt{(s + a_x^2)(s + a_y^2)(s + a_z^2)}}. \quad (5.2)$$

For the other depolarization factors (N_y and N_z), interchange a_x , a_y and a_z . For prolate spheroids, as our rods, with $a_x > a_y = a_z$, the depolarization factors become:

$$N_x = \frac{1 - e^2}{2e^3} \left(\ln \frac{1 + e}{1 - e} - 2e \right) \quad \text{and} \quad N_y = N_z = \frac{1}{2} (1 - N_x), \quad (5.3)$$

with $e = \sqrt{1 - a_y^2/a_x^2}$ the eccentricity of the ellipsoid. To estimate the dipole moment of our rods using this model, we take the volume and aspect ratio of the ellipsoid equal

to that of our rods. The energy U of an ellipsoid with an effective dipole moment p in an electric field E is given by:

$$U(\theta) = -p \cdot E, \quad (5.4)$$

where θ is the angle between the major axis of the particle and the field direction. Using the ellipsoid model, it is found, as expected, that single rods most favorably orient with their rotational symmetry axis along the applied electric field, such as shown in Fig. 5.2a.

At higher concentrations, the dipolar rods start interacting with each other through their electric fields. As we know from electrostatics, it is energetically favorable for dipoles to lie head-to-toe and unfavorable to lie side-by-side. To model these configuration for rods, we introduce a simplified model to estimate the interaction between two polarized rods. Here, the dipole moment of the rod is represented by two equal charges q that are placed at a distance $L - D$, with L the end-to-end length of the rods and D their diameter (see Fig. 5.1). The polarization of one of the rods due to the field of the other rod is neglected by this model. To determine q , we equate the dipole moment found by the ellipsoid model to that of the two charges: $p = q(L - D)$. The energy difference between two rods that are placed side-by-side and two rods that are placed head-to-toe, $\Delta U = U_{sbs} - U_{htt}$, can then be calculated using Coulomb's law:

$$\Delta U = \frac{q^2}{4\pi\epsilon_s\epsilon_0} \left(\frac{3}{D+x} - \frac{2}{L+x} - \frac{2}{\sqrt{(D+x)^2 + (L-D)^2}} + \frac{1}{2L-D+x} \right), \quad (5.5)$$

with x the separation between the rods to accommodate an electric double layer. Since ΔU is positive, the rods are expected to form strings at higher field strengths, similarly as observed for spheres [30,31] (Fig. 5.2b). What happens in a more concentrated system is a more difficult problem because of the long range of the dipolar interactions [145]. For instance, only a lengthy calculation for spheres in the dipolar approximation can show why a body centered lattice has a lower dipolar energy configuration as compared to e.g. a face centered cubic lattice. Such calculations have hardly been performed yet for anisotropic particles and in order to obtain the free energy also the entropy of the structure has to be evaluated [147, 148]. In a certain region of concentrations and field strengths, a special crystal structure is predicted [143], shown in Fig. 5.2c.

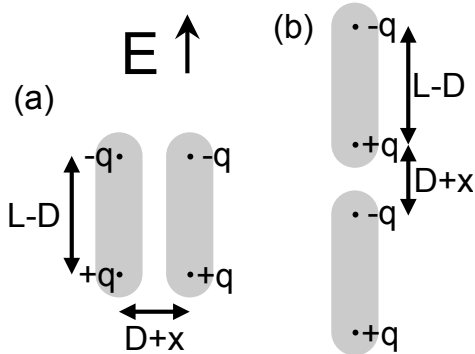


FIGURE 5.1. Dipoles represented by two equal charges placed at a distance $L - D$. The separation between the rods is x . (a) Side-by-side configuration. (b) Head-to-toe configuration.

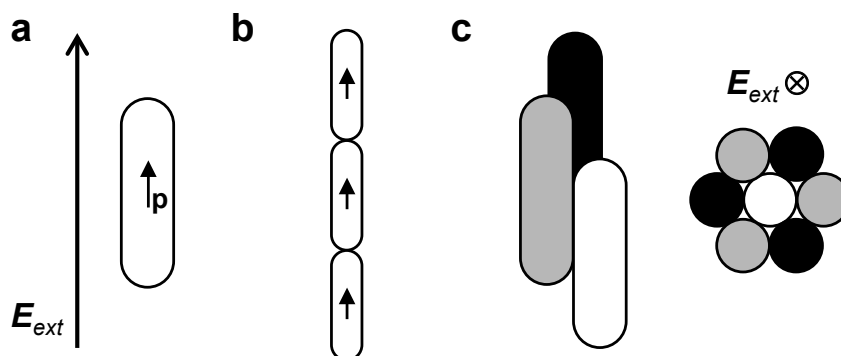


FIGURE 5.2. Induced dipoles in rods. (a) Single rods point their induced dipole moment p parallel to the field direction at low field strengths. (b) Dipole-dipole interactions cause the rods to line up head-to-toe at higher field strengths. (c) At high density and high field, strings order hexagonally and form a new crystal structure in which neighboring particles are positioned at different heights.

In this structure, the rods are ordered in strings which are positioned close together on a hexagonal lattice. Due to the dipole-dipole interactions neighboring rods are not positioned side-by-side, but shifted a distance $(L + x)/3$ in the z direction.

5.3. EXPERIMENTAL

5.3.1. Dispersions

The systems that were used to study dilute systems in an electric field are listed in Table 5.1. Two of these systems were used to study the effect of the electric field on phase behavior: one system of short, and one of long rods, with aspect ratios of 3.6 and 6.0 respectively. The rods were prepared as described in Chapter 2. Systems B35 and B31 consisted of non-fluorescent core particles with a 30 nm FITC-labeled fluorescent inner shell and a 190 nm non-fluorescent outer shell. The rods of B47 had a FITC-labeled core and a 150 nm non-fluorescent shell. Systems N51 had a rhodamine isothiocyanate (RITC) labeled core and a 150 nm non-fluorescent shell. B47 and N51 had a fluorescent pattern that faded from head to toe.

The solvent mixture consisted of dimethylsulfoxide (DMSO, $\geq 99.9\%$, Sigma-Aldrich) and ultrapure water (Millipore system). The particles were dispersed in DMSO first, after which water was added until the refractive index was matched by eye. This resulted in a 10/0.85 volume ratio of DMSO/water with an index of refraction of 1.47 and a viscosity of 1.92 cP (at 20°C).

	L (μm)	σ_L	D (nm)	σ_D	L/D	V (μm^3)
B35	3.3	10%	550	11%	6.0	0.74
B31	2.37	10%	640	7.5%	3.6	0.69
B47	2.1	9.5%	620	6.6%	3.4	0.57
N51	2.66	10%	530	6.3%	5.0	0.55

TABLE 5.1. Dimensions of the systems of rods as measured by TEM. Here, L is the end-to-end length of the rods, D the diameter, σ the polydispersity and V the volume.

5.3.2. Sample cells

Three types of sample cells were used: one to apply a field directed perpendicular to gravity and two to apply a field directed parallel to gravity. The first consisted of two 50 μm diameter T2 thermocouple alloy wires (Goodfellow) running on opposite sides through a 0.1×1 mm glass capillary. The distance between the wires was around 0.7 mm. The capillaries were sealed with a layer of candle wax, followed by a layer of two-component epoxy (Bison).

For the experiments with a relatively low electric field parallel to gravity, 0.1×1 mm capillaries were used, with glass walls of 0.1 mm thick, that were coated with 3 nm of chromium and 7 nm of gold, subsequently. The capillary was positioned on top of two 50 μm wires to keep it horizontal, of which one was connected with a standard electronic wire. A second contact was made by putting a 50 μm wire on top of the capillary, connecting it to the capillary by silverpaint (SPI-paint) and wrapping it around a standard electronic wire. The same type of cell was used for the experiments with dilute systems in an electric field. In this case the two gold-coated sides of a square 0.2×0.2 mm capillary were placed on the side, so that an electric field perpendicular to gravity was created.

A high electric field, parallel to gravity, was applied using cells that consisted of two conductive and transparent indium tin oxide (ITO) coated glass slides (30-60 Ω , Diamond coatings limited), which were separated by glass spacers (No. 00 cover slides by Menzel-Gläser, thickness around 100 μm). The conductive sides of the ITO-slides were on the inside of the cell, in direct contact with the dispersion, and all parts were glued together with UV-glue (Norland No. 68). Electrical contacts were made by gluing 50 μm diameter wires to the conductive side of the ITO slides with silverpaint. The thin electrical wires were wrapped around standard electronic wire to enable connection to the electrical set-up. The cells were sealed with UV-glue.

For configurations in which several layers of material are positioned between the electrodes, which is the case when the electrodes are on the outside of the capillary, the

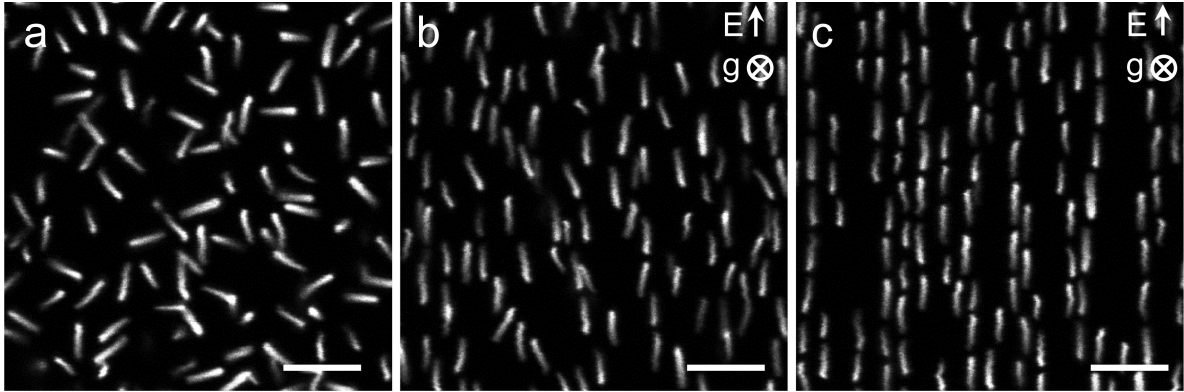


FIGURE 5.3. Dilute dispersions of rods of system N51 in a 1 MHz electric field. (a) Rods oriented in random directions when no field was applied. (b) Rods oriented along the field direction at low field-strengths ($E \sim 0.05 \text{ V}/\mu\text{m}$). (c) At higher field-strengths ($E \sim 0.1 \text{ V}/\mu\text{m}$) dipole-dipole interactions caused the rods to position head-to-toe in strings. Scale bars indicate $5 \mu\text{m}$.

electric field inside any of these layers can be calculated by:

$$E_i = \frac{V}{\varepsilon_i} \left(\frac{\varepsilon_1 \varepsilon_2 \varepsilon_3}{d_1 \varepsilon_2 \varepsilon_3 + d_2 \varepsilon_1 \varepsilon_3 + d_3 \varepsilon_1 \varepsilon_2} \right), \quad (5.6)$$

with V the applied voltage, ε_i the dielectric constant of the material the field strength is calculated in, ε_{1-3} the dielectric constants of layers 1-3 and d_{1-3} the thickness of layer 1-3. In our cells, which consist of two layers of glass ($d = 0.1 \text{ mm}$, $\varepsilon = 3.5$) and one layer of solvent (DMSO/water, $d = 0.1 \text{ mm}$, $\varepsilon = 50$), the field inside the solvent can thus be calculated by $E = 3.4 \cdot 10^{-4} V$ ($\text{V}/\mu\text{m}$). When the electrodes are in direct contact with the solvent E is simply V/d (d the distance between the electrodes).

5.3.3. Electric field

A function generator (Agilent, type 33220A or 33120A) was used to generate a sinusoidal signal with a frequency of 1 MHz and an amplitude of 3.0 V. The generated signal was sent to the sample via a wide band amplifier (Krohn-Hite, 7602M), which was used to control the field strength in the sample cell. The field strength was measured by an oscilloscope (Tektronix, TDS3012B or TDS3052) and is given in $V_{RMS}/\mu\text{m}$ in this chapter.

5.4. RESULTS AND DISCUSSION

5.4.1. Dilute dispersions of polarizable rods in electric fields

When silica particles are dispersed in a mixture of DMSO and water, the high contrast in dielectric constant between the colloid ($\varepsilon_{SiO_2} \sim 4.5 \varepsilon_0$) and the solvent ($\varepsilon_{DMSO/water} \sim 50 \varepsilon_0$ [149]) induces a dipole moment when an electric field is applied. For rods, the strength of the dipole moment depends on their orientation with respect

	L (μm)	D (nm)	L/D	A (m^2/V^2)	B (m^2/V^2)
B35	3.3	550	6.0	7.50×10^{-8}	1.28×10^{-7}
B31	2.37	640	3.6	7.31×10^{-8}	1.16×10^{-7}
B47	2.1	620	3.4	6.08×10^{-8}	9.47×10^{-8}
N51	2.66	530	5.0	5.62×10^{-8}	9.35×10^{-8}

TABLE 5.2. Variables A and B in the interaction energy between a dipolar rod and an electric field for four different systems calculated for $\varepsilon_s = 50$ and $\varepsilon_c = 4.5$. The corresponding equation for the interaction energy: $U/(k_B T) = (A \cos^2(\theta) + B \sin^2(\theta))E^2$.

to the field direction. Furthermore, the behavior of rod-like particles in an electric field depends on the strength of their dipole moments, which can be influenced by changing the strength of the applied external electric field. In our experiments we used an electric field with a frequency of 1 MHz to prevent polarization of the double layer. The behavior of a dilute dispersion of rods at different electric field strength regimes is shown in Fig. 5.3. While the rods were randomly oriented when no electric field was applied (Fig. 5.3a), they oriented with their long axis parallel to the field direction at low field strength ($E \sim 0.05$ V/ μm , Fig. 5.3b). When the field was increased to $E \sim 0.1$ V/ μm , string formation was observed (Fig. 5.3c).

The alignment of rods with an external electric field can be explained by considering the interaction energy of the polarized rod with the field. Using the ellipsoid model it is possible to calculate the dipole moment of the rod as a function of θ (the angle between the rods long axis and the field direction). The resulting interaction energy for rods with the field is given by $U/(k_B T) = (A \cos^2(\theta) + B \sin^2(\theta))E^2$, which is minimized when $\theta = 0$. The values for A and B of the systems that were used in this chapter were calculated from Eq. 5.1-5.4 and are listed in Table 5.2. Note that the α 's are negative for silica rods in DMSO/water. The difference in energy between the orientations parallel and perpendicular to the field for system B35 is about $5.3k_B T$ for $E = 0.01$ V/ μm according to this model, and grows quadratically with increasing field strength.

The alignment of rods with an external electric field was examined in more detail by measuring the orientation of rods in a dilute dispersion ($\varphi = 0.0025$) for several field strengths. The degree of alignment of the experimental system as a function of the applied electric field was calculated using the two-dimensional nematic order parameter S_{2D} from 2D confocal images like that in Fig. 5.3b:

$$S_{2D} = \frac{1}{N} \left\langle \sum_{i=1}^N \cos(2\theta_i) \right\rangle \quad (5.7)$$

where θ_i is the angle between the i^{th} rod's long axis and the nematic director, which

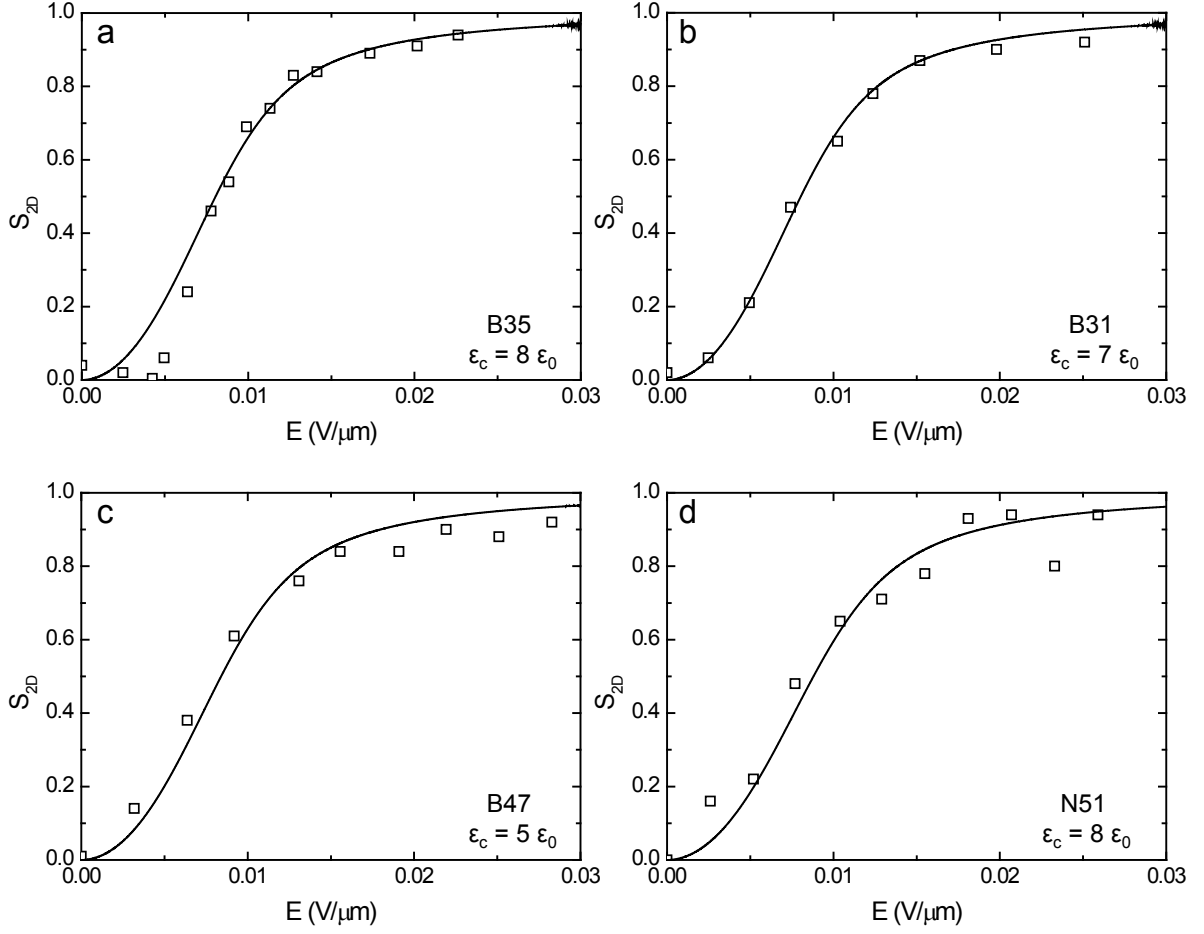


FIGURE 5.4. Nematic order parameter as a function of the applied electric field in dilute dispersions of four different systems. The open squares are experimental data, the line is a fit to the order parameter calculated for ellipsoids using ε_c as a fitting parameter.

in this case corresponds to the electric field direction. Note that θ_i is the projection of the actual angle in the imaging plane. S_{2D} takes on an average value between 0 for a completely disordered (isotropic) phase, and 1 for a phase perfectly oriented in the plane of view. Since the measured S_{2D} corresponds well with the actual nematic order parameter of the system (see Section 3.3.3), we also expect the model for the polarization of ellipsoids to fit our data well. To do so, we calculated S_{2D} using the orientational distribution function $P(\theta)$ of the ellipsoid model:

$$S_{2D} = \int_0^{\pi/2} P(\theta) \cos(2\theta) d\theta \quad \text{with} \quad P(\theta) = \frac{\exp(-U(\theta)/k_B T)}{\int_0^{\pi/2} \exp(-U(\theta)/k_B T) d\theta}, \quad (5.8)$$

where $k_B T$ is the thermal energy. To map the curve onto our experimental results, we fixed the dielectric constant of the solvent at $50\varepsilon_0$ and took the dielectric constant of

	V (μm^3)	p_{\parallel} (C m)	$\Delta U_0/k_B T$	$\Delta U_{0.2}/k_B T$
B35	0.74	-2.98×10^{-23}	22	15
B31	0.69	-2.85×10^{-23}	35	23
B47	0.57	-2.49×10^{-23}	35	23
N51	0.55	-2.14×10^{-23}	18	12

TABLE 5.3. Dipole moment p_{\parallel} for rods oriented parallel to an electric field of $E = 0.1 \text{ V}/\mu\text{m}$ and the corresponding difference in energy between two rods placed side-by-side and two rods placed head-to-toe, when two rods touch (U_0) and with a distance of 200 nm between the rods ($U_{0.2}$).

the particles as a fitting parameter. Figure 5.4 shows that this model corresponds well with our experimental results. The estimation for the dielectric constants for the silica rods that were obtained by the fitting procedure varies from 5 to $8\epsilon_0$ for all systems. These values correspond well with literature, where we find a dielectric constant of $4.5\epsilon_0$ for pure silica [149]. Since our rods are slightly porous (see Chapter 2), their dielectric constant may be expected to be higher because the pores are filled with DMSO/water with an ϵ of ~ 50 . Even though our rods are bullet-shaped, the ellipsoid model thus seems to describe their polarization reasonably well.

When the field was increased to $E \sim 0.1 \text{ V}/\mu\text{m}$, the rods formed strings. String formation can be explained by considering the interactions between the induced dipolar rods. We estimated the strength of these interactions using the simplified model described in Section 5.2. When the strings formed, the rods were aligned with the field and therefore we take $\theta = 0$ in the calculation of the dipole moment. Using our simplified model (Eq. 5.5), the difference in energy between two rods positioned side-by-side and two rods positioned head-to-toe can now be calculated (Fig. 5.1 and Eq. 5.5). Table 5.3 shows that the difference in energy between the two configurations at $E = 0.1 \text{ V}/\mu\text{m}$ is of the order of $20 - 30k_B T$ when the rods touch (U_0). The rods in our experimental system, however, are slightly negatively charged so that they carry an electric double layer, which increases their effective diameter with about 200 nm when they are close-packed. Taking this extra distance into account decreases the interaction energy to about $10 - 20k_B T$ ($U_{0.2}$). In a more dilute sample, D_{eff} will be even larger and the interaction smaller. The field that is needed to cause string formation is thus higher in a more dilute sample, where the distance between the rods is large.

5.4.2. Concentrated dispersions of short rods in low electric fields

In Chapter 4 we showed that short rods with an aspect ratio of 3.6 crystallize directly from the isotropic phase into hexagonally ordered domains that are primarily single layers without regular stacking. These rods are too short to form nematic

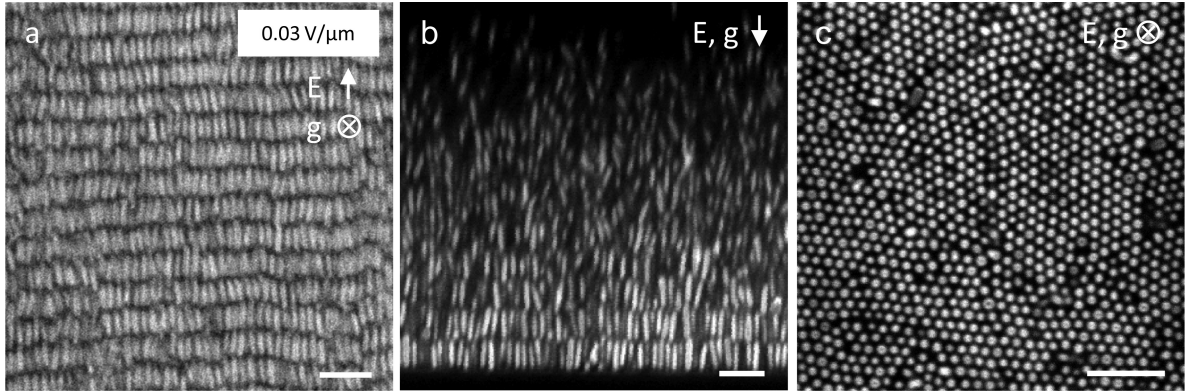


FIGURE 5.5. Short $L/D = 3.6$ rods (B31) after sedimentation in a $0.03 \text{ V}/\mu\text{m}$ electric field, starting from a volume fraction of 0.1 in a $100 \mu\text{m}$ high capillary formed a para-smectic phase. (a) Electric field perpendicular to gravity: the rods aligned with the field and formed layers. (b) Electric field parallel to gravity: the rods aligned with the field and ordered in layers. (c) Within the layers, the rods show hexagonal ordering (second layer from the bottom). Scale bars indicate $5 \mu\text{m}$.

or smectic liquid crystal phases, as was confirmed by computer simulations on hard spherocylinders [96]. However, with the application of electric fields we have a tool at our disposal to induce orientational order in this system of sedimenting rods. The formation of a para-nematic phase was trivial in this case: the rods aligned when a field of $0.03 \text{ V}/\mu\text{m}$ was applied and a para-nematic phase was formed (Fig. 5.3b). We noticed that the field needed to align particles in the concentrated sediment of a sample was lower than the field needed to align rods in the dilute top-part of a sample. In a field of $\sim 0.03 \text{ V}/\mu\text{m}$, sediments aligned, while the top-part showed an isotropic phase that aligned at a field of $\sim 0.05 \text{ V}/\mu\text{m}$. This effect can be explained by the fact that in the dilute phase, alignment is caused only by the interaction between the induced dipole and the field. In the sediment, however, increased density will add a gain in translational entropy to the dipole-field interactions when the rods align, which means that a lower electric field is required to align the rods.

Interestingly, it was found that the combination of the induced orientational order caused by the field and the increase in density due to sedimentation resulted not only in alignment of individual rods, but also in the formation of a regularly layered structure such as shown in Fig. 5.5. Within the layers, the rods showed hexagonal ordering, but no correlations between neighboring layers were found. Therefore, the structure was identified as a smectic- B phase.

When the field was increased to $0.07 \text{ V}/\mu\text{m}$, dipole-dipole interactions started to contribute significantly, which expressed itself in a repulsive interaction between the ends of neighboring rods. This resulted in a distortion of the layered structure and

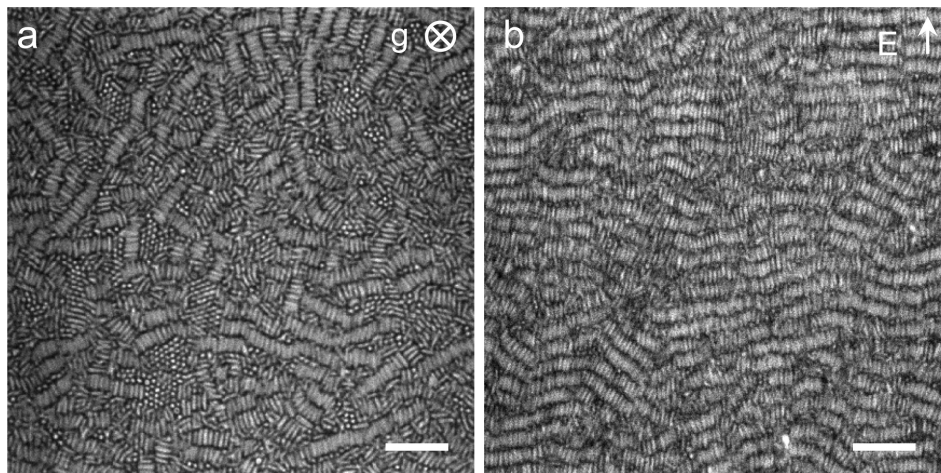


FIGURE 5.6. Short $L/D = 3.6$ rods after sedimentation. (a) Without application of an external electric field. (b) Two days after a $0.03 \text{ V}/\mu\text{m}$ electric field had been switched off. Scale bars indicate $10 \mu\text{m}$.

a transition, probably via a hexagonal columnar phase which we need to investigate further, to the C_3 -symmetric crystal structure described in Section 5.2. Because this structure is more easily visualized with long rods, it will be discussed in more detail in the next section.

After the field of $0.07 \text{ V}/\mu\text{m}$ had been turned off, the rods lost part of their long range orientational and positional order. During this process, the system first went back to the smectic phase that it formed at low fields ($0.03 \text{ V}/\mu\text{m}$), to finally end up in a state that looked similar to a sample that had sedimented without ever having been exposed to an electric field (hexagonally ordered domains of one layer thick, without regular stacking of these layers, Fig. 5.6a). Although the system lost part of its order two days after an electric field had been switched off, the sample still possessed considerably more order than a sample that had not been exposed to an electric field at all (see Fig. 5.6b). Nevertheless, it is remarkable that long range ordering in smectic layers is apparently unstable at this volume fraction.

5.4.3. Concentrated dispersions of long rods in low electric fields

In contrast to the short rods, particles with an aspect ratio of 6 do show nematic and smectic liquid crystal phases when they sediment (see Chapter 4, Fig. 4.7). Even though the electric field is not needed to induce orientational order and a layered structure in this case, it was found to be helpful to control the direction of alignment and to reduce defects. We observed alignment of particles in the sediment parallel to the field for electric fields of $0.02 \text{ V}/\mu\text{m}$. Similarly to the experiments with the shorter rods, a layered structure with rods pointing in the field direction was formed when the field was applied during sedimentation. Additionally, it was possible to form the same phase when the field was employed after the rods had sedimented. In this case the rods rotated

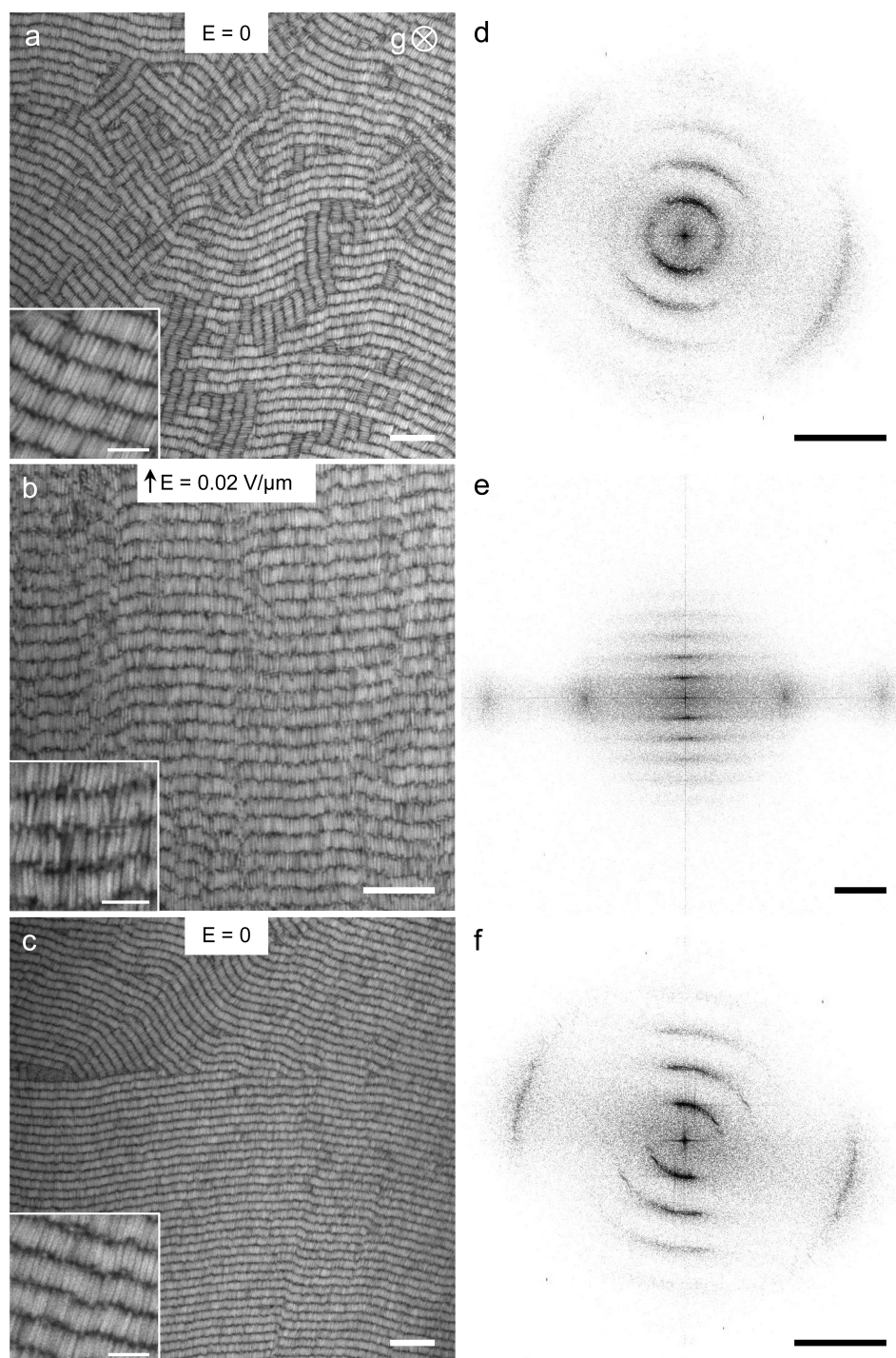


FIGURE 5.7. Applying a field to a sediment of $L/D = 6$ rods, the initial volume fraction was 0.05 in a $100 \mu\text{m}$ high capillary. The images were taken at different positions in the sample, but at approximately the same height (a few microns from the bottom). (a) After 1 night of sedimentation without electric field. (b) 30 minutes after turning on a $0.2 \text{ V}/\mu\text{m}$ field. (c) 5 days after the field had been turned off. (d-f) Fourier transforms on a logarithmic intensity scale of the images on the left. Scale bars indicate $15 \mu\text{m}$ for a-c, $5 \mu\text{m}$ for the insets and $3 \mu\text{m}^{-1}$ for d-f.

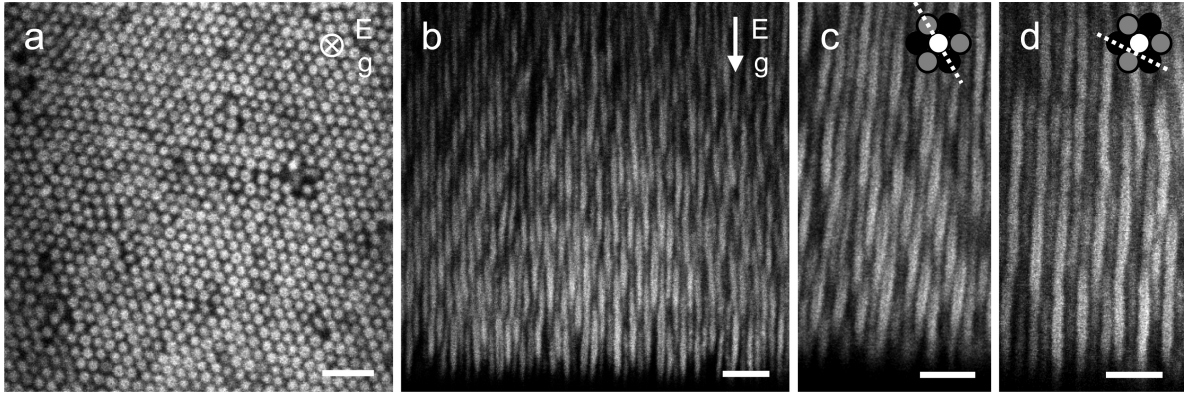


FIGURE 5.8. Long $L/D = 6$ rods in a $0.06 \text{ V}/\mu\text{m}$ field parallel to gravity. (a) Hexagonal ordering in the xy -direction. (b) Parallel to the field direction the rods shifted one third of their length up or down with respect to their neighbors. (c) and (d) Cuts at different angles through the crystal. Scale bars indicate $5 \mu\text{m}$ for a and $3 \mu\text{m}$ for b-d.

to align with the field within 20 minutes and the sample changed from having multiple domains to only one orientation (Fig. 5.7). The Fourier transforms of the images show the improved order when a field is applied. When the electric field was switched off after 1 night, the general orientation of the rods remained in the (former) field direction, but several defects were formed (Fig. 5.7c). A possible explanation for the formation of defects is provided by the inter-layer spacing. In a field of $0.02 \text{ V}/\mu\text{m}$, the inter-layer spacing was $1.24 L$, which decreased to $1.16 L$ when the field strength was zero. An explanation for the difference is provided by weak dipole-dipole interactions (on the order of $0.5k_B T$ for two rods side-by-side at these field strengths), which cause the ends of the rods in one layer to repel each other slightly. As a result, the rods shift in position with respect to their neighbors and stick out partly above or below the layer, making it effectively broader. When the field is turned off, dipole-dipole interactions disappear and the system relaxes back to its original inter-layer spacing. However, since there was more space between the layers when the field was on, this allowed for defects to form. Figure 5.7c shows that these defects are mainly splay distortions and edge dislocations.

In fields higher than $0.03 \text{ V}/\mu\text{m}$ (up to $0.14 \text{ V}/\mu\text{m}$), the strength of the electric field induced interactions increased to the extent that ordering into layers was no longer favorable. However, the hexagonal ordering in the radial direction remained (Fig. 5.8a). In this field strength regime, it was energetically most favorable to shift neighboring rods one third of their length up or down. The resulting configuration of rods is a C_3 -symmetric crystal structure, which has also been found in the computer simulations by Rotunno *et al.* [143]. Figure 5.8 provides experimental proof for the C_3 -symmetric crystal, by showing several cuts through the structure. When the field was reduced

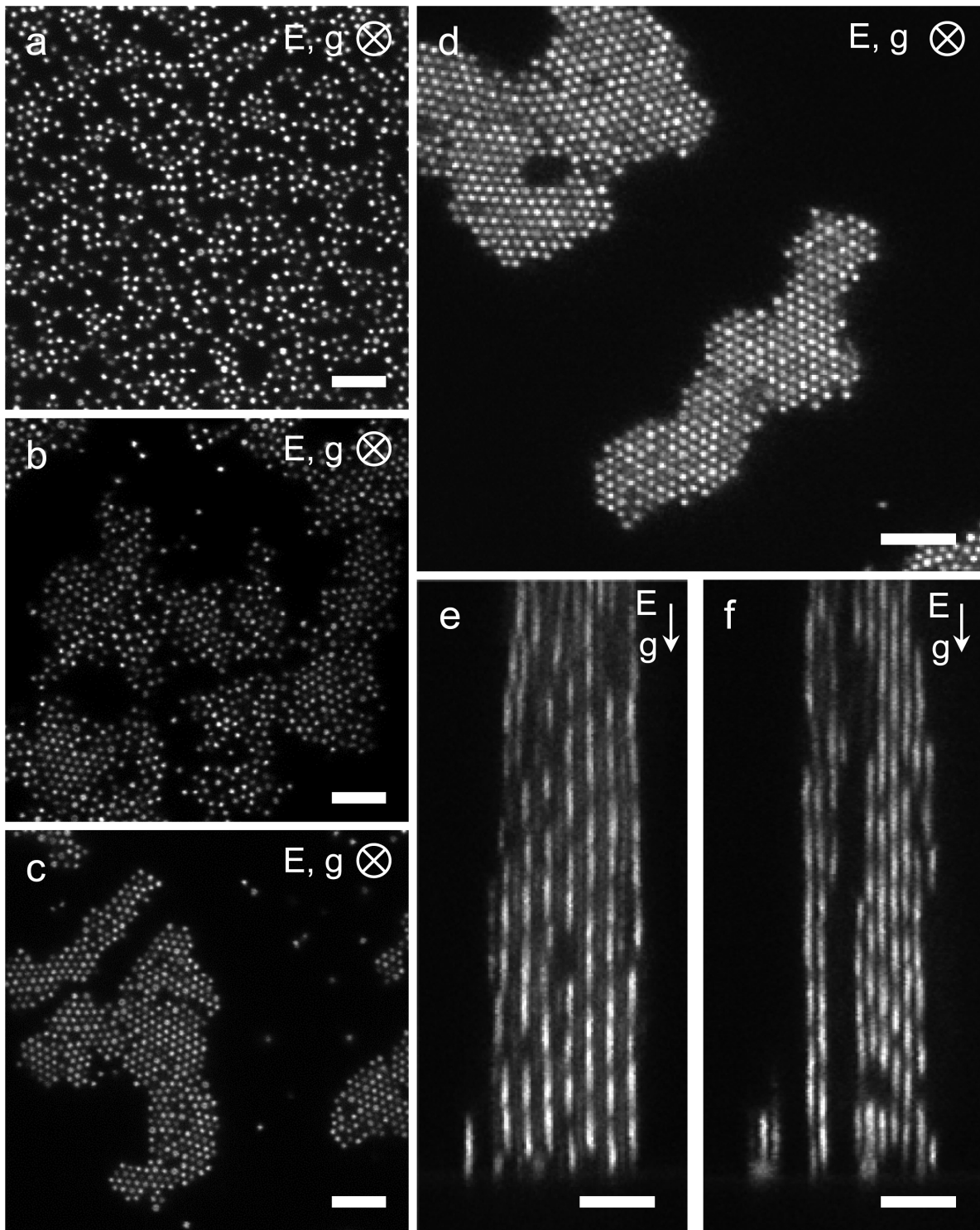


FIGURE 5.9. Short $L/D = 4$ rods in a field parallel to gravity, $10 \mu\text{m}$ above the bottom. Gap width is $\sim 120 \mu\text{m}$. (a) 1.5 min after switching a $0.18 \text{ V}/\mu\text{m}$, 1 MHz field on. (b) 18 min after the field was turned on. (c) Increasing the field to $0.25 \text{ V}/\mu\text{m}$. (d) A few minutes later. (e) Side-view of the sample showing the crystalline structure of the columns. (f) Cut through the crystal showing the $L/3$ jump in z -position of neighboring rods. Scale bars indicate $5 \mu\text{m}$.

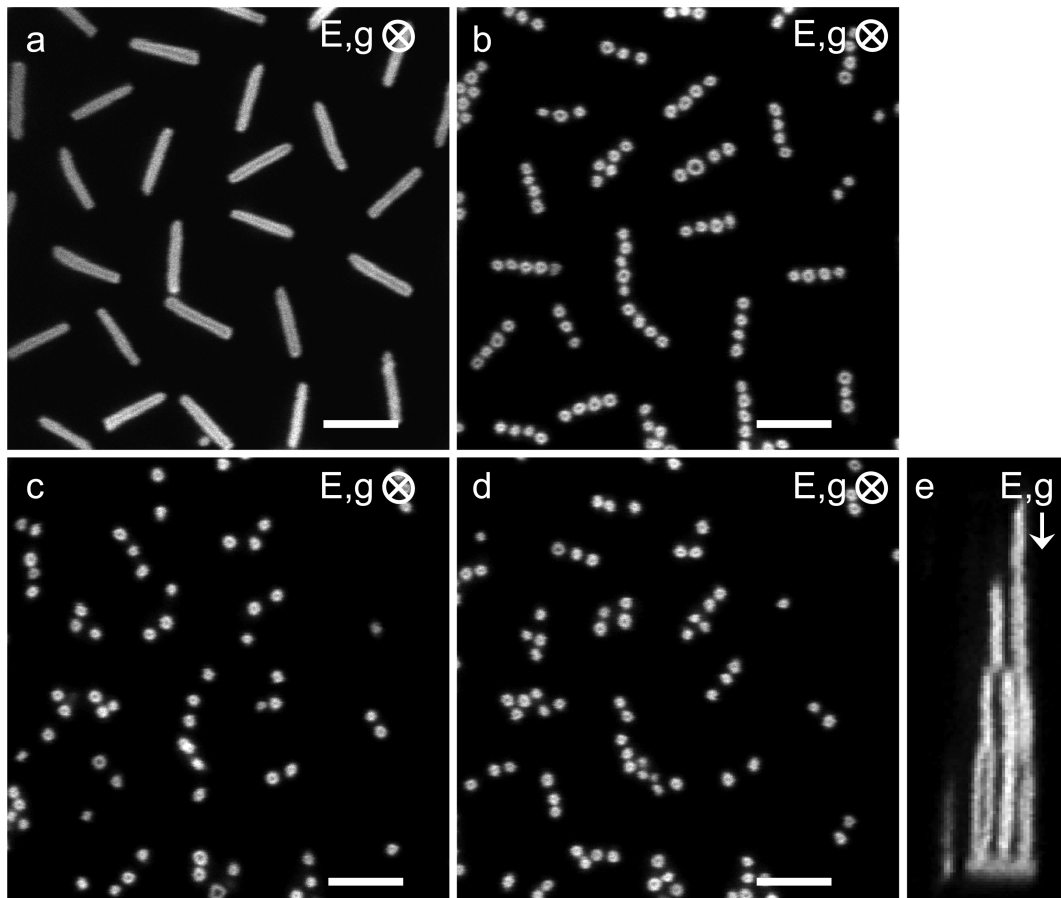


FIGURE 5.10. Long $L/D = 6$ rods in a $0.5 \text{ V}/\mu\text{m}$, 1 MHz field parallel to gravity. The spacing between the electrodes was approximately $15 \mu\text{m}$. (a) Rods on the glass bottom plate oriented parallel to the electrode surface (flat). (b) First layer of rods standing straight on the flat rods. (c) Second layer of rods. (d) Third layer. (e) View of rods standing on a flat one from the side. Scale bars indicate $5 \mu\text{m}$.

to $0.02 \text{ V}/\mu\text{m}$, the system relaxed back into the layered structure that is shown in Fig. 5.7b.

5.4.4. Rods in high electric fields

At field-strengths higher than $0.14 \text{ V}/\mu\text{m}$, dipole-dipole interactions became so strong that the rods formed strings from the bottom upwards rather than sedimenting to the bottom of the sample, as shown in Fig. 5.9 for rods with $L = 2.6 \mu\text{m}$ and $D = 630 \text{ nm}$. The gravitational height of these rods was $l_g = 0.7 \mu\text{m}$, meaning that it would cost about $4k_B T$ in gravitational energy to place one rod on top of another. The energy of two rods in the head-to-toe configuration at this field strength is about $-12k_B T$ compared to two rods infinitely far apart, according to our simplified model, which is sufficient to overcome the loss in gravitational energy and explains the string formation.

Together with string formation, vacancies appeared in the xy -plane, and the rods grouped together in time (Fig. 5.9a-b). In contrast to spheres in high fields [30], the rods did not form sheets in fields of $0.18 \text{ V}/\mu\text{m}$. It is not sure at this moment if this is true for all volume fractions. Since dipoles placed side-by-side are repulsive, the sideways attraction can only be favorable if the rods are shifted along their length. Indeed, the groups of rods slowly ordered into the C_3 -symmetric crystal structure. At higher field strengths ($0.25 \text{ V}/\mu\text{m}$), the formation of the crystal structure occurred faster due to stronger interactions. Figure 5.9d shows that eventually all rods became part of C_3 -symmetric crystal columns. Unfortunately, we did not succeed in applying electric fields higher than $\sim 0.25 \text{ V}/\mu\text{m}$ in sample cells with an electrode gap of $120 \mu\text{m}$. At higher fields, temperature differences caused flow in the sample. Attempts to prevent this included the coating of the electrodes with a thin (100 nm) layer of silica to prevent any current running through the sample. Also, a glycerol/water mixture and DMSO without water were tried as a solvent. None of these were successful, though.

Similar to experiments with spheres, the structures that were formed in these high electric fields, depended on the distance between the electrodes. At large gap widths, the previously described C_3 -symmetric crystal columns were formed, while at small gap widths structures such as shown in Fig. 5.10 were observed. In the case of spheres, this dependence on gap width was explained by image charges which cause a break in symmetry of the dipolar interactions [30]. On the bottom of samples that had a field higher than $0.18 \text{ V}/\mu\text{m}$ applied, rods were lying flat on the electrode surface and acted as templates for particles that were positioned above them (see Fig. 5.10). Even at field strengths as high as $0.5 \text{ V}/\mu\text{m}$, these flat rods did not align with the electric field, but still performed translational and rotational Brownian motion on the surface, which indicates that they were not attached to the glass plate. We expect that this phenomenon can also be explained by image charges, because it was only seen when the electrodes were on the inside of the cell.

5.5. CONCLUSIONS

By analyzing the orientational distributions of individual rods in an external electric field, the field response of our particles could be measured conveniently in real space without having to resort to multiple particle effects. The measured curves correspond well with the polarization of ellipsoids, a model that can be solved analytically. At higher particle concentrations, the electric field was found to align liquid crystal phases and even form phases not present without the field.

For short rods ($L/D = 3.6$) at higher volume fractions, the induced orientational order caused by the electric field led to the formation of para-nematic and -smectic phases at high volume fractions that would not have formed without the application of an electric field. Long rods ($L/D = 6$) that do spontaneously form equilibrium nematic

and smectic phases were forced to orient in one direction, which led to the formation of a smectic phase with only one orientation throughout the sample. The application of the electric field additionally decreased the number of defects in smectic phases of long rods significantly. Also, the nematic phase was extended to lower volume fractions under the influence of an electric field.

The combination of an electric field between 0.03 and 0.14 V/ μm and an increased volume fraction due to sedimentation caused the formation of a crystal structure that has not been experimentally observed before: the C_3 -symmetric crystal structure. This structure consists of hexagonally ordered rods, of which neighboring rods differ by $L/3$ in height because dipole-dipole interactions make it unfavorable for them to be side-by-side. C_3 -symmetric crystals were observed both in systems of short and long rods.

Fields higher than 0.14 V/ μm were found to induce string formation so strongly that sedimentation was counteracted. When the field was pointing in the same direction as gravity, particles that were positioned flat on the bottom of the sample acted as templates for particles that were positioned above them, which resulted in the formation of comb-like structures at small gap widths. At large gap widths, columns of tightly packed rods were formed that showed C_3 -symmetric crystalline order.

5.6. ACKNOWLEDGEMENTS

First of all, we would like to thank Rao Vutukuri for demonstrating the electric field cell construction, the pleasant collaboration while experimenting and fruitful discussions about the performed experiments. Also, we wish to thank Michiel Hermes for useful experimental suggestions and discussions. Part of the measurements of the orientation of the rods as a function of the electric field were performed by Bart de Leeuw.

6

Rods in combined shear and gravitational fields

ABSTRACT

Steady shear flow was successfully applied to align rod-like silica particles with an aspect ratio of 6, and create shear induced nematic, columnar and smectic liquid crystal phases, aligned with the director in the flow direction. Upon application of steady shear to rods in an isotropic phase, a shear induced para-nematic was almost instantly formed. After sufficient sedimentation, the alignment induced by the shear was maintained in the sample when the shear was stopped and upon further sedimentation a shear aligned smectic- B phase was formed. When the shear was continuously applied during sedimentation a columnar phase was formed, with its director pointing in the velocity-direction. The application of oscillatory shear led to the formation of smectic-like domains in a sample that was previously in a shear aligned nematic state. Although these experiments are only preliminary, they give a strong indication that shear is a powerful external field to align colloidal liquid crystal phases over larger areas.

6.1. INTRODUCTION

When subjected to shear flow, liquid crystals can exhibit a variety of surprising phenomena, which arise because of the anisotropic shape of the rods. From a theoretical point of view, the behavior of dense systems of elongated particles in shear flow was investigated by Hess [150] and by Doi and Edwards [151, 152], resulting in an equation that governs the time development of the orientational distribution function. In the absence of flow, the Doi-Edwards-Hess (DEH) theory reduces to the Onsager description of equilibrium nematic liquid crystals [25]. The variety of states, depending on the initial state of the liquid crystal and the shear rate, that is predicted by the DEH theory is extensively described in, for instance, reference [153]. In summary, the DEH theory predicts that all particles in the *nematic* phase collectively ‘tumble’ in the shear plane at low shear rates, which means that the unit vector pointing along the average direction of the long axes of the particles, i.e., the director, describes an orbit in the plane defined by the velocity and the velocity gradient vectors [154, 155]. Tumbling is only observed if the director is initially in the shear plane. It is also possible that the director describes a time-periodic orbit oblique to the shearing plane, which is called the ‘kayaking’ state [156]. With increasing shear rates, tumbling and kayaking go over into ‘wagging’, where the director oscillates between two angles in the plane defined by the flow and the gradient of the flow. ‘Log-rolling’ is a state in which the director is initially aligned along the vorticity direction and remains there. At high shear rates, the director is arrested in the shear plane and the rods stay aligned with the flow.

Experimentally, several predictions of the DEH theory have been confirmed using systems of polymeric liquid crystals. Tumbling and shear alignment were found at different shear rates in nematic solutions of poly(benzyl-glutamate) (PBG) [157]. Also, the existence of the wagging and log-rolling state have been confirmed by experiments [158, 159]. The behavior of *colloidal* rods in shear flow was studied using a system of *fd*-virus [160, 161], showing quantitative agreement between the DEH-theory and this colloidal system. Brownian dynamics simulations on the periodic orientational motions in the nematic phase of long rods ($20 < L/D < 60$), performed by Tao *et al.* [162–164], were also consistent with DEH theory and the *fd*-virus experiments. The fact that also particles with much shorter aspect ratio ($L/D = 3$) perform kayaking, wagging and flow aligning behavior was shown by simulations on ellipsoids in shear flow [165].

The effect of shear flow on smectic phases has often been studied in the configuration where the layers are parallel to the planes of constant velocity. For instance, theoretical models inspired by experimental results are treated in references [166, 167]. In this configuration, the layering is stable up to a certain critical shear rate. At higher shear rates, the director and the smectic layers were found to adjust their alignment through undulations of the layers and realignment of the director relative to the layers to end

up in a state where the layers are perpendicular to the shear plane, as experimentally shown in references [168–170]. Theory and computer simulations show that shear that is applied to smectic phases that are oriented with their layers parallel to the gradient-vorticity plane, also causes structural changes [171, 172]. It was found that the layers tilt progressively with increasing shear. At a critical shear, however, the particles were found to rearrange themselves; the sample melts near the center and reforms with a reduced tilt consistent with the layers that are still present at the walls. Shear induced melting and recrystallization was also measured experimentally in smectic-*A* and smectic-*B* phases of butyloxy-benzylidene-octylaniline [173].

In this chapter, we present preliminary results of our first experiments on the combined effect of shear and gravity on a dispersion of $L/D = 6$ silica rods using confocal microscopy. In contrast to polymeric liquid crystals or *fd*-virus systems, silica rods allow for quantitative 3D real-space studies on the single particle level, while scattering techniques, that measure average quantities well, but yield little information about single particle behavior, were used in earlier studies. Furthermore, silica rods, opposed to polymeric systems, are affected significantly by gravity. Here, we use the concentrating effect of gravity to create shear aligned dense phases in systems that were initially in the isotropic phase.

6.2. EXPERIMENTAL

6.2.1. Shear cell

A parallel plate shear cell was used in which both the top and bottom plate can be moved independently, as shown schematically in Fig. 6.1 and described in detail in reference [90]. The shear cell was mounted on an inverted confocal microscope. The bottom plate was a 0.13-0.16 mm thick smooth glass plate with an area of $24 \times 50 \text{ mm}^2$ and the top glass plate was a 0.5-0.6 mm thick smooth glass plate of 10 by 33 mm. The glass plates were attached to holders (called cassettes) with the help of two-component glue and an optical flat to guarantee flatness. The cassettes were placed into their respective translation stages, where they rest on three ball bearings of which the heights can be adjusted to achieve parallelism and the desired spacing h . The distance between the glass plates was minimized in order to use as little dispersion as possible. The values of h that were used varied between 30 and 50 μm . The positions of the top and bottom plate were determined using a confocal microscope in reflection mode.

Shear rate $\dot{\gamma}$ and maximum strain amplitude γ_{max} in the shear cell are given by:

$$\dot{\gamma} = \frac{v_T + v_B}{h} \quad \text{and} \quad \gamma_{max} = \frac{A_T + A_B}{h}, \quad (6.1)$$

where v_T and v_B are the speeds of the top and bottom plate, respectively. A is the amplitude of the oscillation.

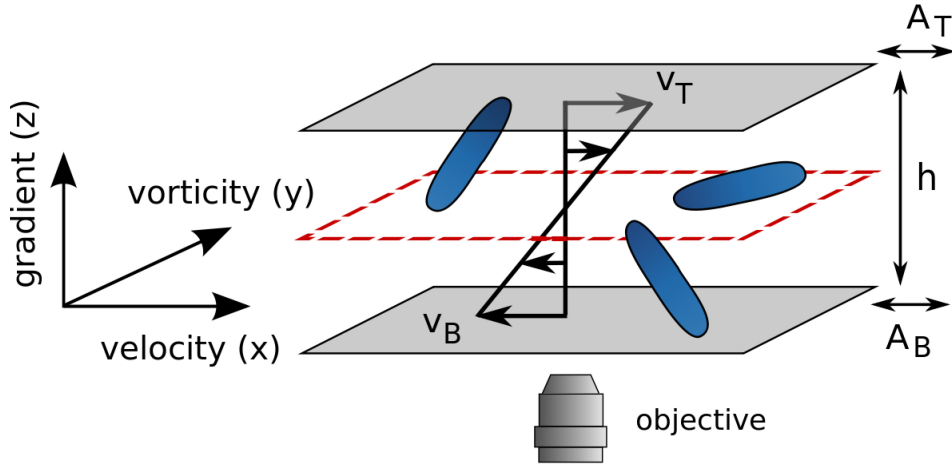


FIGURE 6.1. Schematic representation of the shear cell. Top and bottom plate, separated by a distance h , move in opposite directions with amplitude A and velocity v . This creates a zero velocity plane (denoted by the dashed lines) in the space between them. The vertical position of the zero velocity plane can be set to any height by changing the velocities of the plates but keeping h constant.

Since top and bottom plates move in opposite directions, a zero-velocity plane is created in the space between them. The position of the zero-velocity plane can be adjusted by tuning v_T and v_B :

$$z_{zvp} = \frac{h}{1/r + 1} \quad \text{with} \quad r = \frac{v_B}{v_T}. \quad (6.2)$$

In this chapter the convention is used that the x -axis is along the velocity direction, the y -axis along the vorticity direction and the z -axis along the gradient direction (see Fig. 6.1).

6.2.2. Dispersion

Silica rods, prepared as described in Chapter 2 and 3, were used with length $L = 3.3 \mu\text{m}$ and diameter $D = 550 \text{ nm}$ ($L/D = 6.0$). The corresponding polydispersities were 10% in length and 11% in diameter. The system consisted of non-fluorescent core particles with a 30 nm FITC-labeled fluorescent inner shell and a 190 nm non-fluorescent outer shell. Confocal microscopy measurements of dense sediments of this system showed that the effective diameter of the rods is approximately 200 nm larger than the diameter measured by transmission electron microscopy (TEM).

The solvent mixture consisted of dimethylsulfoxide (DMSO, $\geq 99.9\%$, Sigma-Aldrich) and ultrapure water (Millipore system). The particles were dispersed in DMSO first, after which water was added until the refractive index was matched by eye. This resulted in a 10/0.85 volume ratio of DMSO/water with an index of refraction of 1.47 and a viscosity of 1.92 cP (at 20°C). The volume fraction of the dispersion was 0.3.

6.2.3. Confocal microscopy and image analysis

Confocal microscopy measurements were performed on a Leica SP2 confocal, using a $100\times$ oil immersion objective (Leica) with a numerical aperture of 1.4. Confocal images were analyzed using the algorithm described in Section 3.3.3 and [81]. The orientation of the rods was used to calculate the two-dimensional nematic order parameter S_{2D} :

$$S_{2D} = \frac{1}{N} \left\langle \sum_{i=1}^N \cos(2\theta_i) \right\rangle, \quad (6.3)$$

where θ_i is the in-plane angle between the i^{th} rod's long axis and the nematic director. S_{2D} takes on an average value between 0 for a completely disordered (isotropic) phase, and 1 for a phase perfectly oriented in the plane of view.

6.3. RESULTS AND DISCUSSION

6.3.1. Alignment induced by shear flow

The influence of shear flow on the average nematic order in a dispersion of $L/D = 6$ silica rods was studied by applying steady shear, with a shear rate of 33 s^{-1} and a strain amplitude of 67, to a dispersion with an initial volume fraction of 0.3. The distance between the plates was approximately $30 \mu\text{m}$. Before applying shear, the system was in the isotropic phase in the zero-velocity plane. Since it is difficult to find the orientation and position of the rods in 3D in systems that have high mobility, the orientation was measured in 2D planes. The nematic order parameter (Eq. 6.3) is expected to work best when the rods align in parallel to the plane of view, which is what they are expected to do when shear is applied. Also, the alignment with the shear is best studied in the zero-velocity (2D) plane of the shear cell, so that particles do not move too quickly out of view by the shear motion. The orientational order parameter S_{2D} was therefore determined for confocal images in this plane. Figure 6.2 shows that a shear induced nematic phase (also called a para-nematic) with its director pointing in the velocity-direction was formed when the sample was subjected to shear flow. The flow induced nematic slowly relaxed back towards the equilibrium isotropic phase when the shear was stopped. However, in the 50 seconds that the shear was stopped in Fig. 6.2c, the sample had not had enough time to reach the equilibrium phase before the shear was reapplied. Almost instantaneously after (re)applying steady shear, the nematic order parameter increased to a plateau level of approximately 0.6.

Shear alignment was observed for shear rates of 2.6 s^{-1} and higher. Phenomena such as tumbling, kayaking, wagging and log-rolling that were predicted to occur at low shear rates have not been observed in our samples (yet). While it would be interesting to study these phenomena on the single particle level, which our system does allow for, it is difficult to get the sample in the right state. Tumbling etc. has been observed for nematic liquid crystals only. Our system of $L/D = 6$ rods in principle shows a

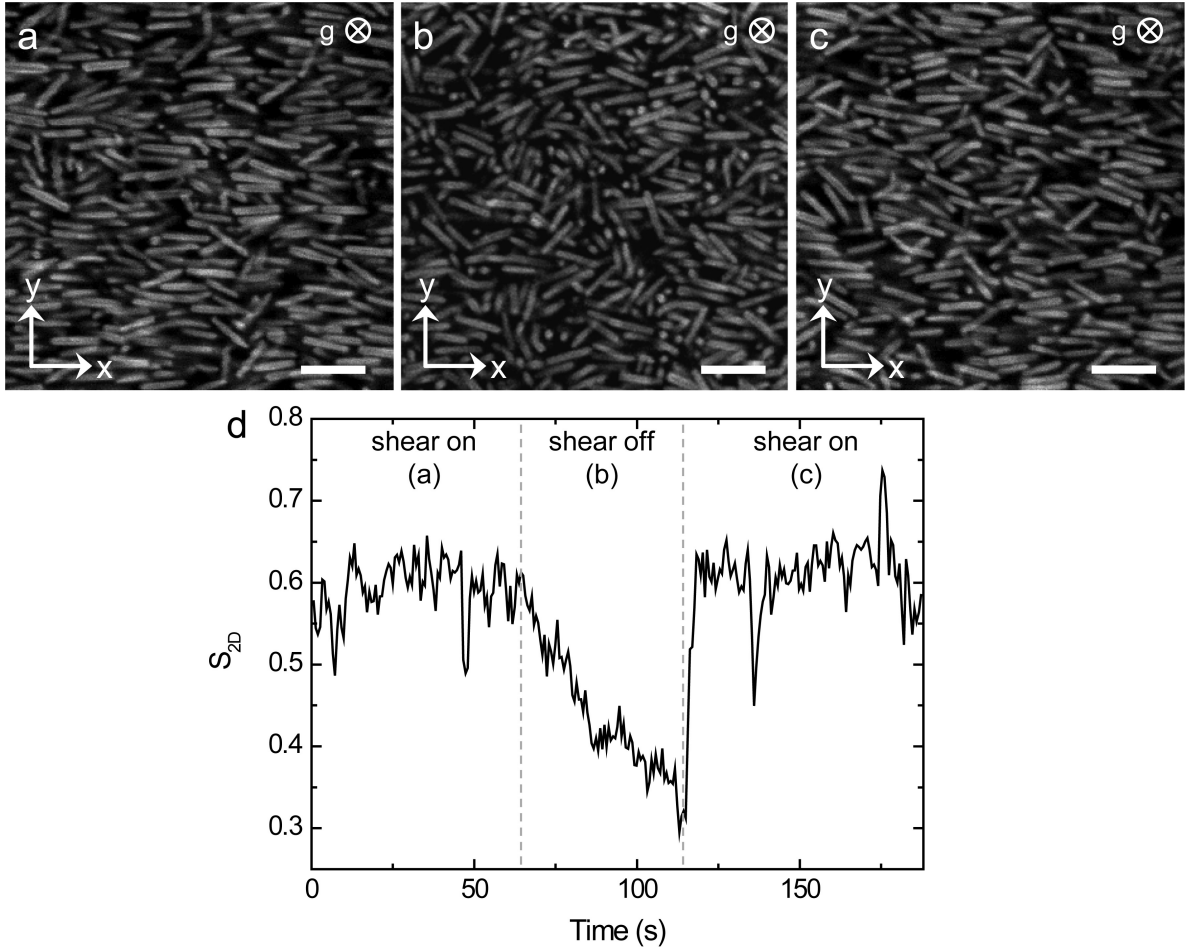


FIGURE 6.2. Shear alignment of the isotropic phase (shear rate 33 s^{-1} , strain amplitude 67). (a) Shear induced nematic phase. (b) Configuration of rods approximately 45 s after the shear was stopped. (c) Shear induced nematic 10 s after the shear was reapplied. (d) Orientational order parameter as a function of time, where shear was applied from the start, stopped for about 50 seconds and was then reapplied. Scale bars indicate $5 \mu\text{m}$.

nematic phase (see Chapter 4), but only in a small range of volume fractions. Due to the sensitivity of the rods to gravity, the samples tended to form a smectic rather than a nematic phase. Therefore, careful fine-tuning of the dispersion's concentration will be required to make these measurements possible. Alternatively, a mixture of rods with different dimensions and aspect ratios can be used to frustrate the formation of a smectic phase. The time-scale of tumbling, with periods between 10 s for shear rates of 1 s^{-1} to 0.2 s for shear rates of 100 s^{-1} that were measured in *fd*-virus suspensions [160], are accessible using confocal microscopy. So, in principle, 3D real space studies of phenomena such as tumbling, kayaking, wagging and log-rolling could be possible using silica rods.

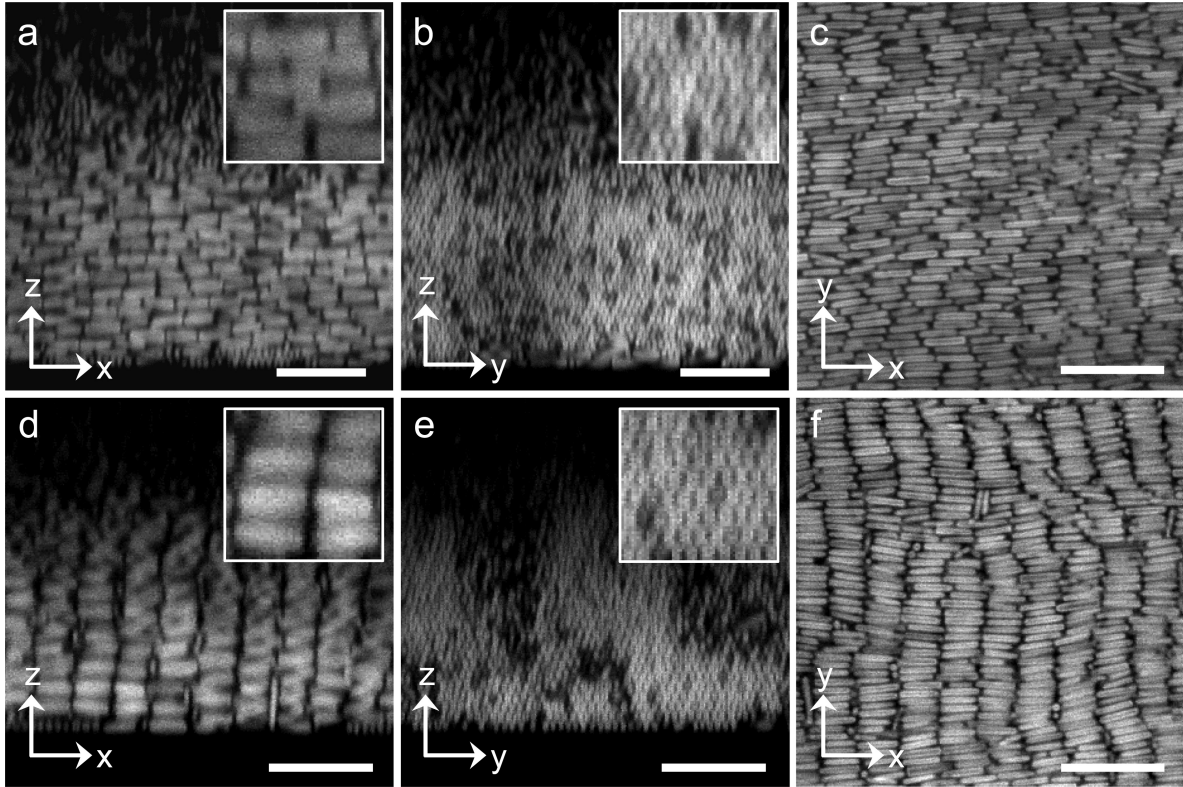


FIGURE 6.3. Shear aligned columnar and smectic phases in different planes. v is the velocity direction, ∇v the gradient direction and ω the vorticity direction. (a-c) When subjected to a shear flow with a shear rate of 2.6 s^{-1} and a strain amplitude of 5.3, a sample with initial volume fraction of 0.3 ordered into a shear aligned columnar phase. (d-f) After shear melting the sample to a paranematic and leaving it to sediment in the absence of shear, the sample was almost completely smectic within 1 hour. Scale bars indicate $10 \mu\text{m}$.

6.3.2. Shear aligned columnar and smectic phases

Combining the ability of shear flow to align the rods and that of gravity to increase concentration, it was possible to create a shear-aligned columnar, or a shear aligned smectic phase on the bottom of the shear cell. Which phase was formed depended on when the shear was stopped. The columnar phase was created by applying steady shear, with a shear rate of 2.6 s^{-1} and a strain amplitude of 5.3, for 3.5 hours. In this time, the volume fraction of rods on the bottom of the sample increased sufficiently to allow for a phase transition from a shear aligned nematic, with its director pointing in the velocity direction, to a shear induced columnar phase. Figure 6.3a-c shows confocal images of the columnar through three different planes. In the velocity-gradient plane as well as in the velocity-vorticity plane, the rods were ordered in horizontally oriented columns. The hexagonal stacking of the columns is visible in the vorticity-gradient plane.

Subjecting the columnar phase to a shear flow with a shear rate of 13.2 s^{-1} and strain amplitude of 26.3, destroyed the 3D order of the sample, but an average orientation of the rods in the velocity direction remained (para-nematic phase). The volume fraction of the rods on the bottom of the sample was sufficiently high at this point to maintain the alignment caused by the shear when the flow was stopped. After cessation of the shear and subsequent sedimentation, the particles ordered in a shear aligned smectic phase within 1 hour, as shown in Fig. 6.3d-f. The rods in the smectic layers of this phase are ordered hexagonally, as shown in Fig. 6.3e. The structure was therefore identified as a smectic-*B* phase.

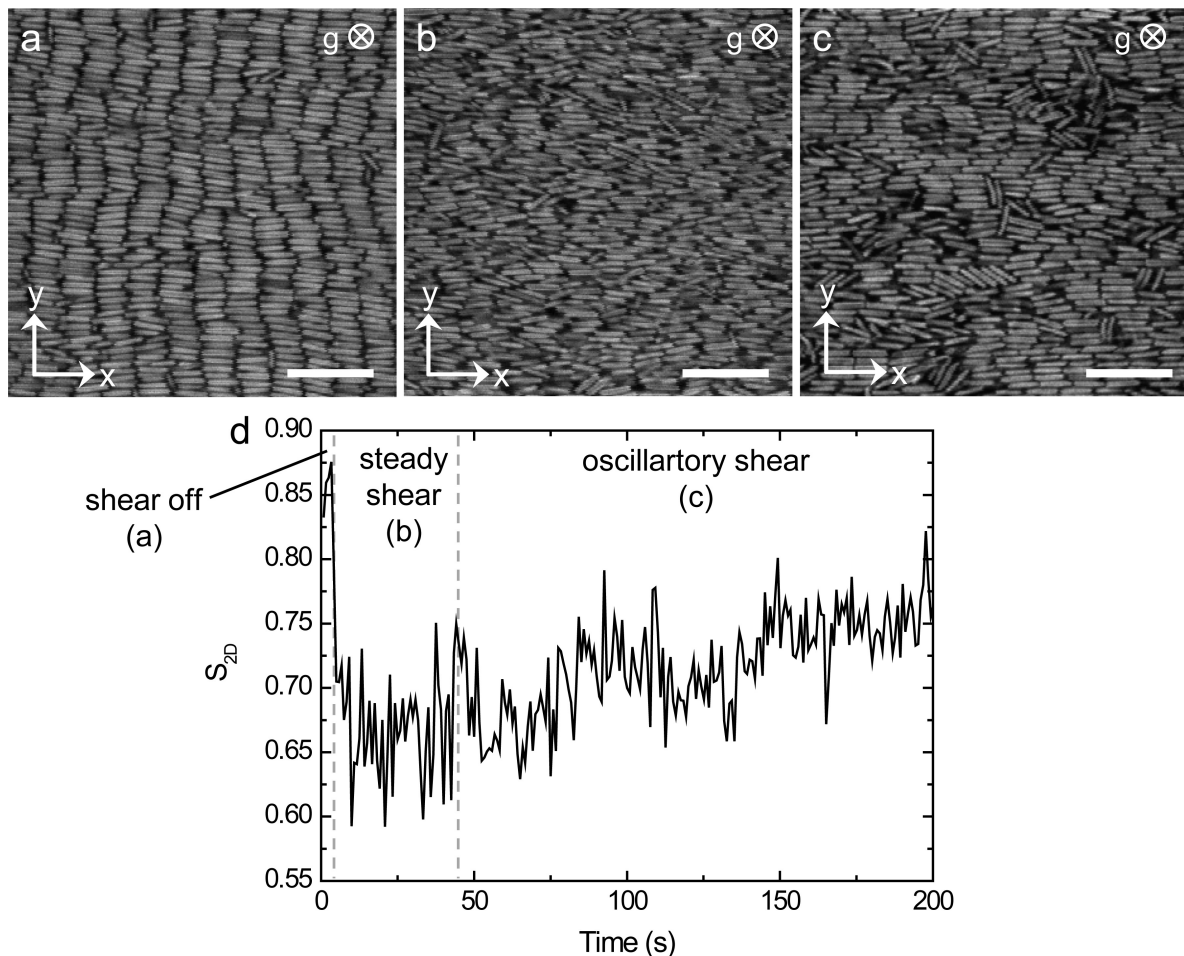


FIGURE 6.4. Application of oscillatory shear to a dispersion of rods. (a) A sedimentation induced shear-aligned smectic phase. (b) Shear melting into a para-nematic. (c) After applying oscillatory shear (shear rate 33 s^{-1} , strain amplitude 7), ordered columnar/smectic-like domains were induced in the para-nematic sample. (d) The nematic order parameter S_{2D} increased significantly when oscillatory shear was applied to the sample. Scale bars indicate $10 \mu\text{m}$.

6.3.3. Oscillatory shear

Besides steady shear, the rods were also subjected to oscillatory shear. Oscillatory shear has been used in several recent experiments to increase the crystalline order of nearly jammed, glassy and gel systems of colloidal spheres [174, 175]. Even in stable fluids of hard-sphere colloids, ordered structures can be formed under the influence of oscillatory shear [176].

The effect of oscillatory shear was studied in a sedimented sample of rods. Before applying oscillatory shear, the rods were subjected to steady shear (shear rate 33 s^{-1} , strain amplitude of 7) and afterwards left to sediment so that a shear aligned smectic formed with a nematic order parameter of 0.85 (Fig. 6.4d). This is the state the system was in at $t = 0$ in Fig. 6.4a. Subsequently, the smectic phase was shear melted to a para-nematic phase with $S_{2D} = 0.65$ by applying large amplitude (~ 25) steady shear (Fig. 6.4b). Upon the application of oscillatory shear, with a shear rate of 33 s^{-1} and a strain amplitude of 7, small smectic or columnar-like domains were formed (Fig. 6.4c). The significant increase in the average nematic order parameter S_{2D} during shear can be clearly seen in Fig. 6.4d. Details about this intriguing phenomenon, such as its stability and development in time, require more experimental work.

6.4. CONCLUSIONS

Steady shear flow was successfully applied to align rod-like silica particles and create shear induced nematic, columnar and smectic liquid crystal phases. Upon application of steady shear to rods in the isotropic phase, a shear induced nematic was almost instantly formed. Although phenomena like tumbling, kayaking, wagging and log-rolling were not observed in our samples during these preliminary experiments, we expect that these phenomena can be studied on the single particle level and in 3D real space using our system as well, probably at lower volume fractions.

Combining the ability of shear flow to align the rods and that of gravity to increase concentration, it was possible to create shear-aligned dense phases on the bottom of the shear cell. After sufficient sedimentation, the alignment induced by the shear was maintained in the sample when the shear was stopped and upon further sedimentation a shear aligned smectic-*B* phase was formed. When the shear was continuously applied during sedimentation a columnar phase was formed, with its director in the velocity-direction. Although these first experiments are preliminary, it is already clear that shear is a powerful field to induce order over large distances.

The application of oscillatory shear to a shear aligned nematic resulted in the formation of smectic-like domains. More experiments are required to examine this phenomenon in more detail.

6.5. ACKNOWLEDGEMENTS

This work was done in collaboration with Thijs Besseling.

7

Directing smectic liquid crystal phases of silica rods by colloidal epitaxy

ABSTRACT

Smectic liquid crystal phases that were formed spontaneously by rods with aspect ratios larger than 5 were aligned successfully by colloidal epitaxy. Templates consisting of trenches of various widths (up to 2 times the length of the rods) and spacings ranging from 0.5 to 3.5 μm were used to align the smectic phases. The aligned area was restricted to the template area with sharp boundaries. For rods with effective aspect ratios smaller than 4, that do not form smectics spontaneously, templates with trench widths smaller than the rod length were used to induce the formation of an aligned smectic-*B* phase. Larger trench widths did induce more order than was measured in sediments on a flat wall, but less than induced by the narrow trenches.

7.1. INTRODUCTION

The control over alignment of liquid-crystal (LC) phases has been investigated extensively because of its importance in optical and optoelectronic applications, such as liquid crystal displays [177]. The effect of the container wall is particularly important and is expressed by the anchoring strength (for a review see e.g. [178]). Anchoring can be planar, tilted or homeotropic depending on whether the anchoring directions are, respectively, parallel, tilted or perpendicular to the interface. A method that is often used to control the director of mostly nematic LC phases consists of rubbing a thin polymer layer with a velvet cloth, creating microscopic grooves on the surface of the polymer [179, 180]. However, as concluded in a review, it is still not well established what the molecular mechanism is for the alignment [181]. One of the reasons is that it is quite hard to disentangle the more specific chemical effects from pure geometrical reasons. A big advantage of studying the effects of anchoring mechanisms by a colloidal LC model system is that the geometry can be studied separately from chemical details as both can be changed independently. Here, we studied the effects of linear grooves made by lithography on an almost hard-rod-like colloidal model system with aspect ratios between 3.4 and 6.0. The wetting behavior of such model systems at unstructured walls was studied by Dijkstra *et al.* [120].

For spherical colloids, it is known that structured walls are a powerful tool to control the growth of colloidal crystals. Experiments that studied the behavior of spheres on templated surfaces showed that colloidal crystals can be dictated to have certain crystal orientations or structures, which can even be metastable [182–186]. Templates were used to grow for instance face centered cubic (FCC) crystals in samples of colloidal spheres that upon sedimentation on a flat wall show random hexagonal stacking. Also, colloidal epitaxy was used to induce the formation of metastable hexagonally close packed (HCP) crystal structures, with stacking sequences dictated by the template. It was shown by computer simulations that the hard sphere crystal wets a smooth wall [187]. However, this transition is very close to the bulk freezing transition (at 98.3%). A correctly structured wall, however, can already induce crystal layers well below bulk freezing (as much as 30% below the bulk pressure) [188, 189].

Although several experimental, theoretical and computer simulation studies have been devoted to the behavior of spherical colloids on a template, work on colloidal rods is much more rare. Being one of the few, Harnau *et al.* reported on the behavior of hard-rod fluids near geometrically structured substrates [190]. They found that a structure of right-angled trenches imposes more ordering inside the pores than on a flat wall. In this work, we experimentally studied the effect of right-angled trenches on a system of almost hard-rod-like colloids.

	L (μm)	σ_L (%)	D (nm)	σ_D (%)	L/D	l_g (μm)
B35	3.3	10	550	11	6.0	0.7
B47	2.1	9.5	620	6.6	3.4	0.9
B48	2.6	8.5	630	6.3	4.0	0.7
N51	2.7	10	530	6.3	5.0	0.9

TABLE 7.1. Properties of the systems of colloidal rods that were used in this chapter. Here, L is the end-to-end length of the rods, D the diameter, σ the polydispersity. L/D the aspect ratio and l_g the gravitational height.

7.2. EXPERIMENTAL

7.2.1. Dispersions

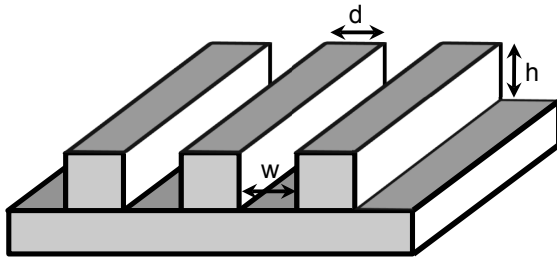
Four systems of silica rods were used, each having different dimensions and aspect ratios (see Table 7.1). The rods were prepared as described in Chapter 2 and 3. System B35 consisted of non-fluorescent core particles with a 30 nm fluorescein isothiocyanate (FITC) labeled fluorescent inner shell and a 190 nm non-fluorescent outer shell. The rods of B47 had an FITC-labeled core and a 150 nm non-fluorescent shell. Systems B48 and N51 had a rhodamine isothiocyanate (RITC) labeled core and a 175 or 150 nm non-fluorescent shell, respectively. B47, B48 and N51 all had a fluorescent pattern that faded from head to toe.

Particle size distributions were determined by transmission electron microscopy (TEM), using a Technai 10 and 12 electron microscope (FEI company). The average length $\langle L \rangle$ and diameter $\langle D \rangle$ of the rods, as well as their standard deviation δ , were measured using iTEM imaging software. The polydispersity is defined as $\sigma_L = \delta_L / \langle L \rangle$. For each sample 50 to 100 particles were measured. The effective diameter of each system of rods was measured by confocal microscopy (Leica SP2) on the bottom of a sedimented sample and was 200 ± 10 nm larger than the diameter measured by TEM for all systems. The effective length was assumed to be also 200 μm larger than the hard-core length.

The solvent mixture consisted of glycerol ($\geq 99\%$, Sigma-Aldrich) and ultrapure water (Millipore system). The particles were dispersed in water first, after which glycerol was added until the refractive index was matched by eye. This resulted in a 0.82/0.18 volume ratio of glycerol/water with an index of refraction of 1.45 and a viscosity of ~ 80 cP (at 20°C).

7.2.2. Templates

The templates that were used in this chapter consisted of areas of $0.1 \times 1 \text{ mm}^2$ in which trenches of different dimensions were created by lithography (see Fig. 7.1). The trenches were 0.1 mm long.



Template	h (nm)	w (μm)	d (μm)
A	610	2.0	0.5
B	610	3.3	3.5
C	610	4.0	2.2
D	610	4.8	1.8
E	610	5.5	1.2

FIGURE 7.1. Schematic representation of the used templates on the left with their dimensions listed in the table on the right.

Master patterns were prepared by electron beam lithography using poly(methylmethacrylate) (PMMA) coated indium tin oxide (ITO) coated glass slides. First, the ITO slides (30-60 Ω , Diamond coatings limited) were cleaned by sonication in acetone for 5 to 10 minutes, after which they were rinsed with isopropyl alcohol. Then they were blown dry with nitrogen first and subsequently dried in an oven for 10 minutes at 180°C in air. A layer of hexamethyldisilazane (HMDS) was spincoated on the ITO slides using a Karl Suss Delta 80 spincoater. The substrates were dried again at 180°C for 1.5 min and a 610 nm thick PMMA-layer was deposited by spincoating a 1-8% w/w solution of 950k PMMA in anisole at 2800 rpm for 40 seconds. After spincoating, the PMMA was baked at 180°C for 1 hour. The patterns were written in the PMMA-layer using an electron beam lithography system (Raith e-LiNE). Doses of 100, 200, 400 and 800 $\mu\text{C}/\text{cm}^2$ were used, of which the lowest dose resulted in patterns with the intended dimensions. Higher doses resulted in broader trenches, because more PMMA was etched away. After electron beam writing, the templates were developed by immersing them in a 1:3 mixture of methyl isobutyl ketone (MIBK) and isopropanol for 90 seconds. The development was stopped by rinsing the substrates with pure isopropanol.

Soft lithography [191] was used to transfer the pattern of the master template to a new cover slide in two steps. First, the negative of the pattern was transferred into a soft mold. Soft molds were made from poly(dimethyl siloxane) (PDMS). The PDMS precursor and curing agent (both in one set, Dow Corning Sylgard 184) were mixed in a 10:1 weight ratio, after which bubbles were removed by short centrifugation (10 seconds at 2000 rpm, Heraeus Sepatech Labofuge Ae). A drop of PDMS precursor mixture was placed on the pattern and left to cure at room temperature for 3 days. The PDMS was then removed from the template and post-cured in an oven at 100°C in air for 1 hour [192].

In the second step, the soft mold was transferred to the final material, leaving a copy of the original pattern. This was done by pressing the PDMS-mold firmly in a small drop of UV glue (Norland Optical Adhesive 68) on a glass cover slide (Menzel no. 1

or 0). The glue was exposed to long wavelength UV light (~ 350 nm) through the mold for at least 2 hours to cure. The dimensions of the resulting templates are listed in Fig. 7.1. The PDMS-molds were used multiple times, but did degrade. The template with dimensions $d \times w$ of 2.0 by 0.5 μm template was successfully created for about five times using the same mold, after that a new mold was required, because the trenches were partially filled with UV-glue.

7.2.3. Sample cells

Sample cells for the B35 rods were constructed by gluing a 1 mm high spacer (object slide, Menzel-Gläzer) onto an object slide with UV-glue (Norland No. 68). The cover slides carrying the templates were glued on top of that with the template on the inside of the cell. After filling with a 0.5 volume percent dispersion, the cells were closed with UV-glue. Finally, the cells were positioned with the slide carrying the template on the bottom.

For the rods with smaller aspect ratios a higher sample cell had to be fabricated due to the lower concentration ($\phi \sim 0.001$) of the dispersion that was used. This type of sample cell consisted of a cover slide (thickness ~ 100 μm) carrying the template with a cylindrical container glued on top of that. The container was made from a pipette tip and had an inner diameter of 7.45 mm. The container was filled with 0.5 ml of dispersion and closed with parafilm to prevent evaporation of the solvent. After 12 days, when confocal microscopy measurements showed that the sediment did not increase anymore, the supernatant was removed and the samples were filled up with another 0.5 ml of dispersion. This resulted in ~ 12 layers for system N51 and ~ 5 layers for system B48.

7.2.4. Confocal microscopy and image analysis

Confocal microscopy measurements were performed on a Leica SP2 confocal, using a $63\times$ oil immersion objective (Leica) with a numerical aperture of 1.4. Confocal images of 30×30 μm^2 were analyzed using the algorithm described in Section 3.3.3 and [81]. The orientation of the rods was used to calculate the two-dimensional nematic order parameter S_{2D} :

$$S_{2D} = \frac{1}{N} \left\langle \sum_{i=1}^N \cos(2\theta_i) \right\rangle, \quad (7.1)$$

where θ_i is the in-plane angle between the i^{th} rod's long axis and the nematic director, measured in the image plane. S_{2D} takes on an average value between 0 for a completely disordered (isotropic) phase, and 1 for a phase perfectly oriented in the plane of view.

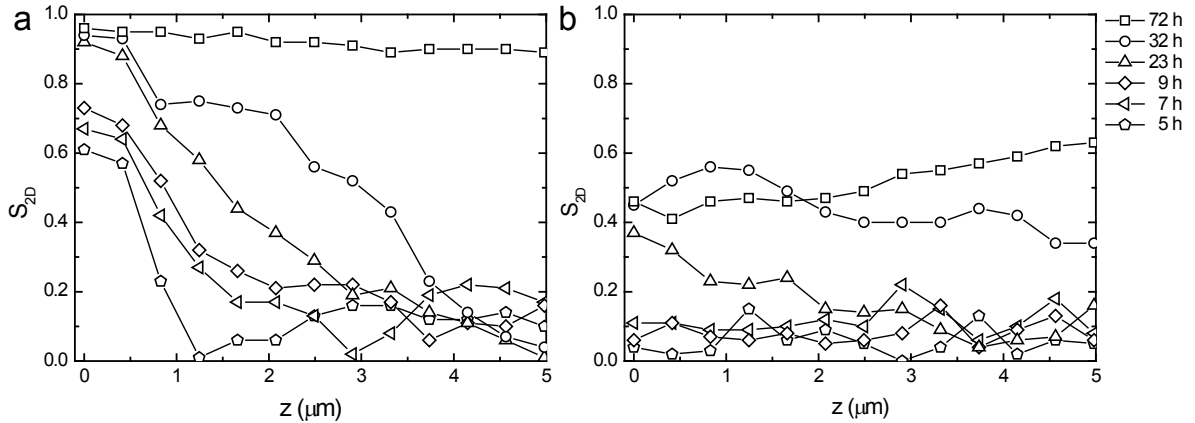


FIGURE 7.2. Sedimentation of B35 ($L/D = 6.0$) rods followed in time. (a) Increased order due to sedimentation on template B ($h \times w \times d = 0.61 \times 3.3 \times 3.5 \mu\text{m}$). (b) Sedimentation on a flat wall.

7.3. RESULTS AND DISCUSSION

In Chapter 4 we showed that a dispersion of rods of which the volume fraction increased due to sedimentation, formed nematic and smectic- A and B liquid crystal phases for aspect ratios higher than 5, while for aspect ratios smaller than 5 no liquid crystal phases were observed. Here, we present our first preliminary observations on the influence of a template on the orientation and phase behavior of both short ($L/D < 5$) and long rods ($L/D > 5$).

7.3.1. Sedimentation of long rods onto a flat or patterned surface

The effect of templates compared to a flat surface on concentrated sediments of long rods was studied using systems B35 and N51 (for dimensions, see Table 7.1). Starting from a dilute dispersion ($\varphi < 0.005$), the volume fraction at the bottom slowly increased in time due to sedimenting particles. Based on the equation for the sedimentation velocity (Eq. 4.4, see Chapter 4), the rods from B35 need around 55 hours to sediment 1 mm. The accompanying increase in orientational order that was measured for system B35 is shown in Fig. 7.2. Here, the nematic order parameter S_{2D} is plotted as a function of height from the bottom of the sample ($z = 0$), for several sedimentation times. Although the depth of the trenches is less than $1k_B T$ (see Table 7.1 for the gravitational lengths of the rods), the effect of the template is visible directly from the start of the sedimentation process. The confinement in the trenches caused alignment in the bottom layer (approximately $1 \mu\text{m}$) of the sample when a template was present. The orientational order in the trenches increased with increasing volume fraction in the following hours of sedimentation. At this same point in time, on the flat wall next to the template, no order could be detected at all (see Fig. 7.2b), which suggests that the template wets the ordered phase. After about one day, the order above the trenches

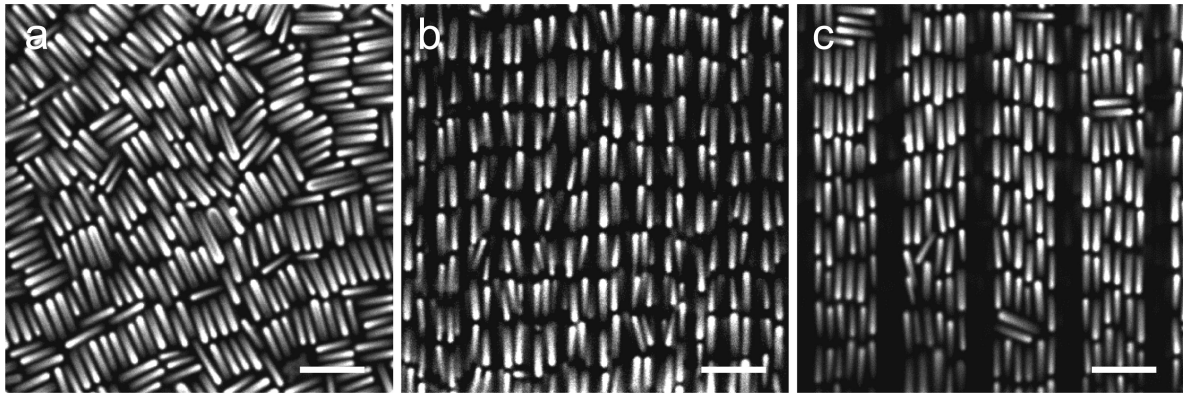


FIGURE 7.3. Bottom layer in a sediment of long rods (N51) on different surfaces. (a) On a flat surface. (b) On template A ($h \times w \times d = 0.61 \times 2.0 \times 0.5 \mu\text{m}$). (c) On template E ($h \times w \times d = 0.61 \times 5.5 \times 1.2 \mu\text{m}$). Scale bars indicate $5 \mu\text{m}$.

started to increase as well as the order above the flat wall. However, at all times the rods above the template showed more alignment than those that sedimented on the flat wall. After three days, the system had reached its equilibrium state and the order did not change anymore.

After the sediment had formed, the bottom layer was studied in more detail. A flat surface had a planar anchoring effect; the rods oriented parallel to the surface, as shown in Fig. 7.3a. Furthermore, neighboring rods oriented in the same direction and started to form smectic rows, but the sample showed many small domains and defects. When the rods sedimented on a template with a trench-width smaller than the length of the rods (Fig. 7.3b), all rods on the bottom aligned in the direction of the trenches. Again, the rods showed the onset of ‘layer’ formation, where the layers were perpendicular to the length of the trenches, although this was limited to the two rods that fitted side by side in the trench. Overall, however, the pairs of rods in neighboring trenches lay side by side, which was probably caused by the layers that formed above. For trench-widths larger than the rod-length (up to $2 L_{eff}$), long rods still oriented predominantly in the direction along the trenches, although small defects of rods oriented perpendicularly to the trenches were also observed (Fig. 7.3c).

Since the height of the trenches was less than one effective rod-diameter, the trenches could accommodate only one layer of rods. The influence of the orientation induced by the template on the rest of the sediment is shown in Fig. 7.4. In this figure, the orientational order and direction of the director in the entire sediment are plotted for various trench-widths after establishment of the equilibrium profile. For both long-rod systems, all templates induced high orientational order ($S_{2D} \sim 0.9$) up to about $8 \mu\text{m}$ high in the sediment. A mismatch between the width of the trench and the length of the rod did not lead to a decrease in induced order, at least up to widths of 2 times

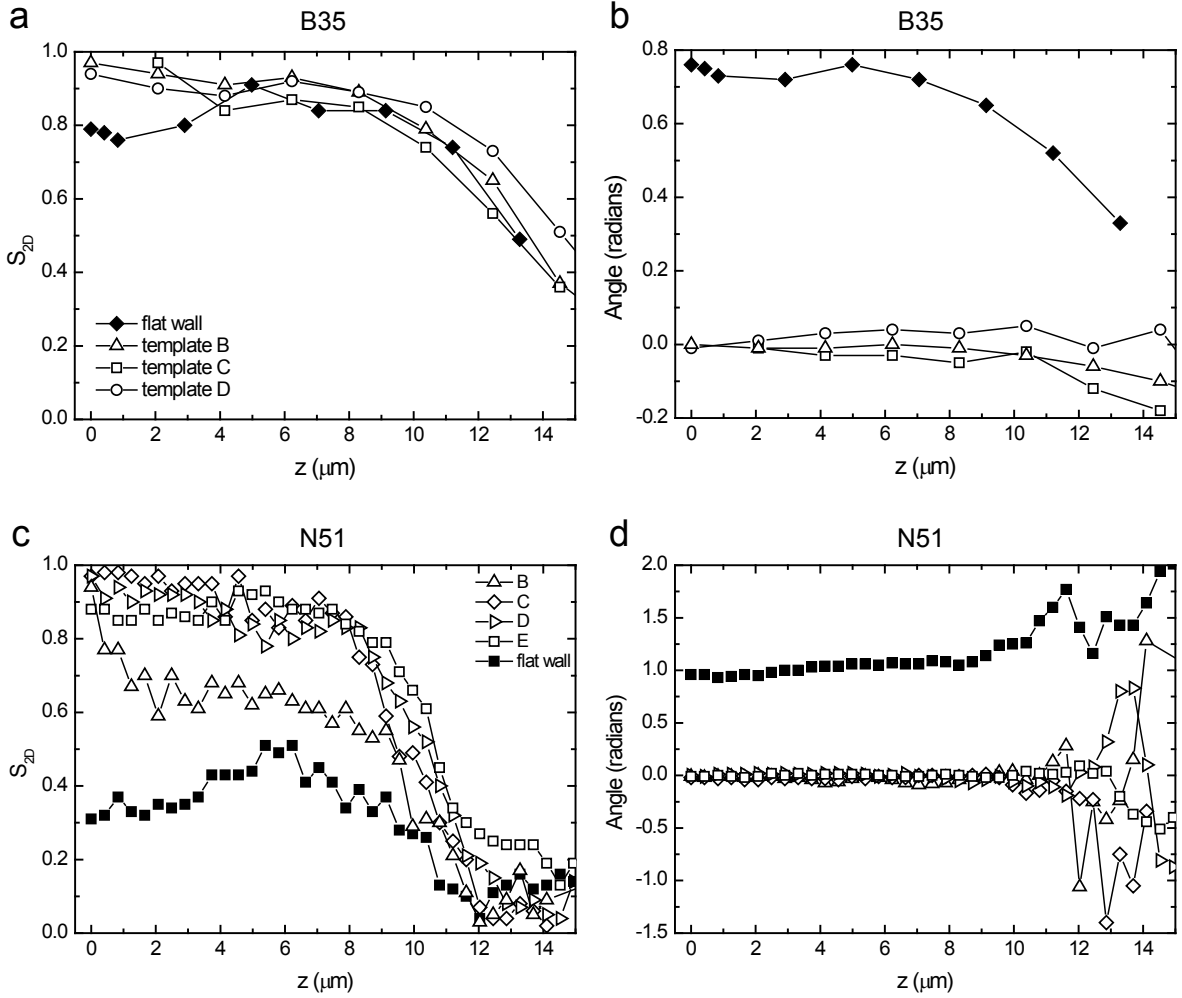


FIGURE 7.4. Orientational order parameter as a function of height after establishment of the equilibrium profile on different templates. (a) B35 ($L/D = 6.0$) after 5 days, and (c) N51 ($L/D = 5.1$) after 20 days. Angle between the director and the direction along the trenches as a function of height for (b) B35, and (d) N51.

the rod length. The sediment consisted of approximately 10 layers of rods ordered in a smectic- B phase on the bottom, above which the order decreased as depicted in Fig. 7.5. The decrease in orientational order in the top part was caused by the lower volume fraction of the dispersion at this point. Because of this observation, we expect that the height of the aligned sediment can be increased simply by adding more particles (e.g. by starting with a higher sample cell). When a template was present, the director of the smectic phase pointed along the trenches for all studied trench-widths.

On a flat wall, the planar anchoring was also continued throughout the sediment, as can be seen in Fig. 7.4b/d. The director started at an arbitrary angle parallel to the surface, and stayed at this angle for the entire sediment. But, since the rods were less well ordered from the beginning, the orientational order parameter in the bottom

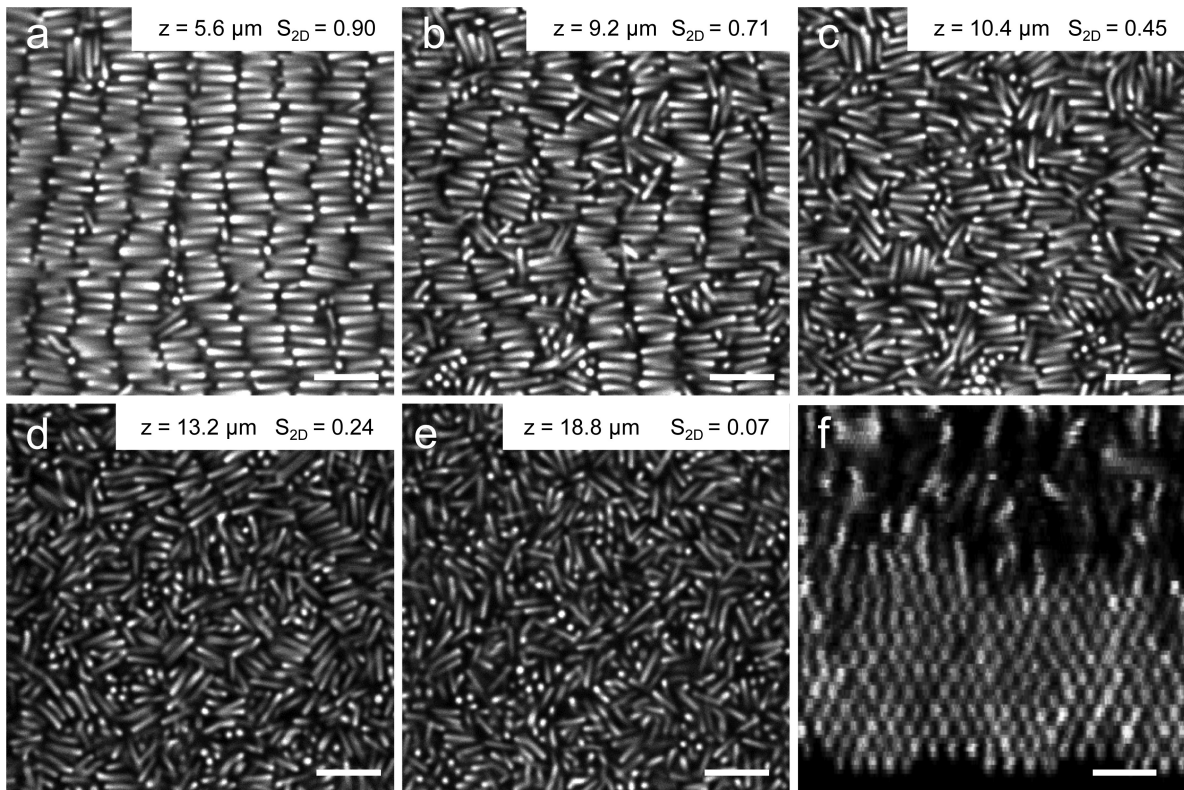


FIGURE 7.5. (a-e) Confocal microscopy images in the xy -plane of the N51 sample on template E ($h \times w \times d = 0.61 \times 5.5 \times 1.2 \mu\text{m}$), taken at different heights above the template and corresponding to the curve shown in Fig. 7.4c. Scale bars indicate $5 \mu\text{m}$. (f) yz -image showing hexagonal stacking in the bottom 10 layers of the sediment. Scale bar indicates $3 \mu\text{m}$.

layers of a sediment on a flat wall did not reach values as high as in the sediments on a template. Higher up in the sample, the orientational order parameter could reach values equal to those above a template. However, the degree of ordering strongly depended on the position in the sample, because it consisted of many domains and was locally strongly defected. For Fig. 7.4a one of the larger domains was chosen, which is the reason that the orientational order parameter is higher than that in Fig. 7.2 and 7.4c.

At the edges of the templated region, the effect of the template is clearly visible. Figure 7.6 shows that the induced orientation by the template restricted itself to the template area only, with amazingly sharp boundaries even several layers above the template. In both directions, along and perpendicular to the trenches, the induced orientation ended at the same position as the end of the template. Along the trenches, layers extended from the template area to the flat wall area, but changed orientation as soon as they were positioned above a flat wall.

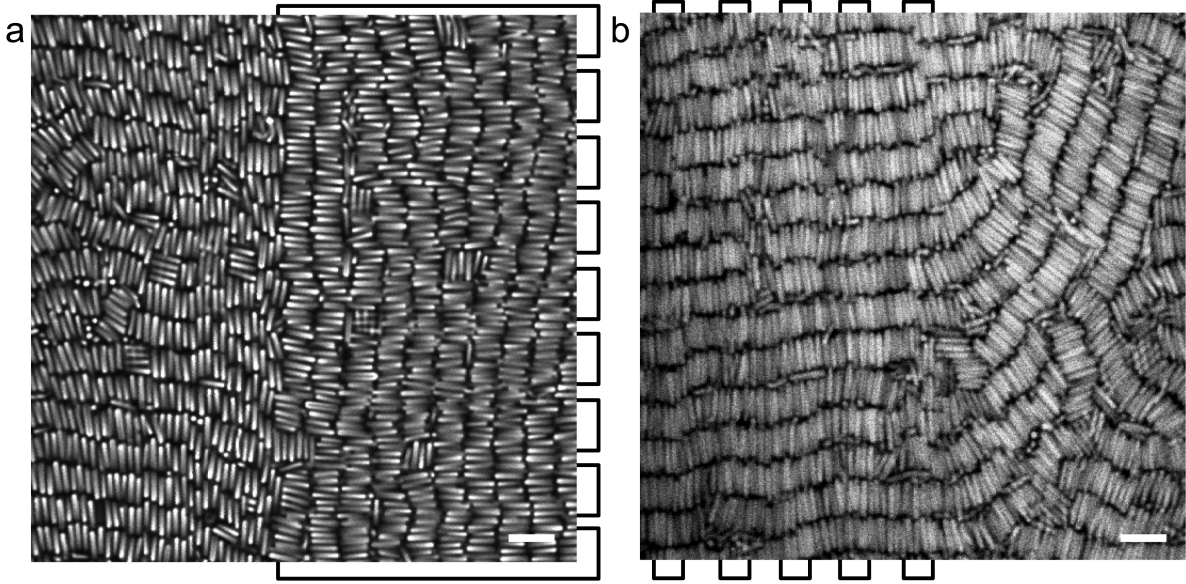


FIGURE 7.6. Confocal images $4 \mu\text{m}$ up in the sediment at the edge of the template. The position of the trenches is indicated around the edges of the images. (a) N51 on template E ($h \times w \times d = 0.61 \times 5.5 \times 1.2 \mu\text{m}$). (b) B35 on template B ($h \times w \times d = 0.61 \times 3.3 \times 3.5 \mu\text{m}$). Induced long-range order is present above the template only. Next to the template, in both directions along and perpendicular to the trenches, no effect of the template is visible. Scale bars indicate $5 \mu\text{m}$.

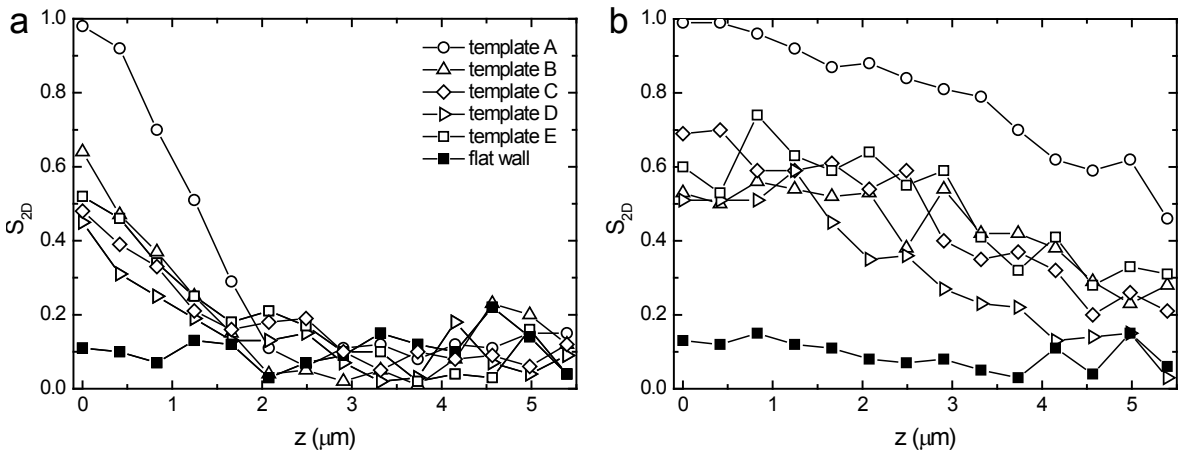


FIGURE 7.7. Orientational order parameter as a function of height in a sediment of B48 ($L/D = 4.0$). (a) After 9 days of sedimentation. (b) After 16 days of sedimentation.

7.3.2. Sedimentation of short rods onto a flat or patterned surface

Short rods, with an aspect ratio smaller than 5, do not show liquid crystalline phase behavior. In Chapter 4 we showed that in these systems hexagonal layers were formed in random directions, without clear stacking of the layers. However, by letting the short rods sediment onto a template, stacking of the hexagonal layers could be induced. Equivalently to the sedimenting systems of long rods, increased orientational order for short rods (B47 or B48) was first observed inside the trenches of the templates (Fig. 7.7a). But where the width of the trenches did not influence the order for long rods, short rods were clearly oriented better by a template with trench-widths smaller than the rods' length. Most likely this difference is related to the fact that this system has its aspect ratio close to the value below which liquid crystal phases are not found. Figure 7.7b shows that the orientational order parameter of the rods in the narrow trenches was almost 1 and above it around 0.9. For trenches wider than one rod-length S_{2D} was around 0.6 and on the flat wall only 0.1. The corresponding real-space images of the bottom four layers of these sediments are shown in Fig. 7.8.

When the trench-width was smaller than one rod-length, the rods oriented parallel to the trenches and formed pairs. Similar to the samples of long rods, these pairs were positioned parallel in neighboring trenches. Above the template, the rods were ordered in layers oriented perpendicular to the trenches (Fig. 7.8 left column).

For trench-widths larger than one rod-length, the rods were less well oriented, as shown in the middle column of Fig. 7.8. Inside the trenches the rods were oriented either parallel or perpendicular to the trenches, with between 70 and 80% of the rods in the parallel orientation. The amount of mismatch between the width of the trenches and the length of the rods did not influence the ratio of rods oriented parallel or perpendicular to the trench. For the largest mismatch (2.3 μm long rods in a 5.5 μm wide trench), still 70% of the rods pointed in the direction of the trenches. This is significantly different from the samples of long rods, where over 90% of the rods was oriented parallel to the trenches. Again, this difference is most likely caused by the fact that the collective effects at short aspect ratios were less strong. The increased number of rods that were oriented perpendicularly, combined with the tendency of the rods to form uncorrelated layers resulted in a sediment with layers running mostly parallel or perpendicular to the template in the bottom of the sediment and in random directions in the top.

On a flat wall, the rods were oriented such that they lay parallel to the surface, with no preferential orientation otherwise. As a result, the layers above showed the same random orientation; the rods were oriented such that they lay in plane and formed rows in random directions so that a low orientational order parameter was measured. Higher up above the plane (see Fig. 7.8) more rods started to be oriented not parallel with the wall anymore. As mentioned before, in systems of short rods the hexagonally ordered layers seem to be oriented in random directions, without clear stacking of the

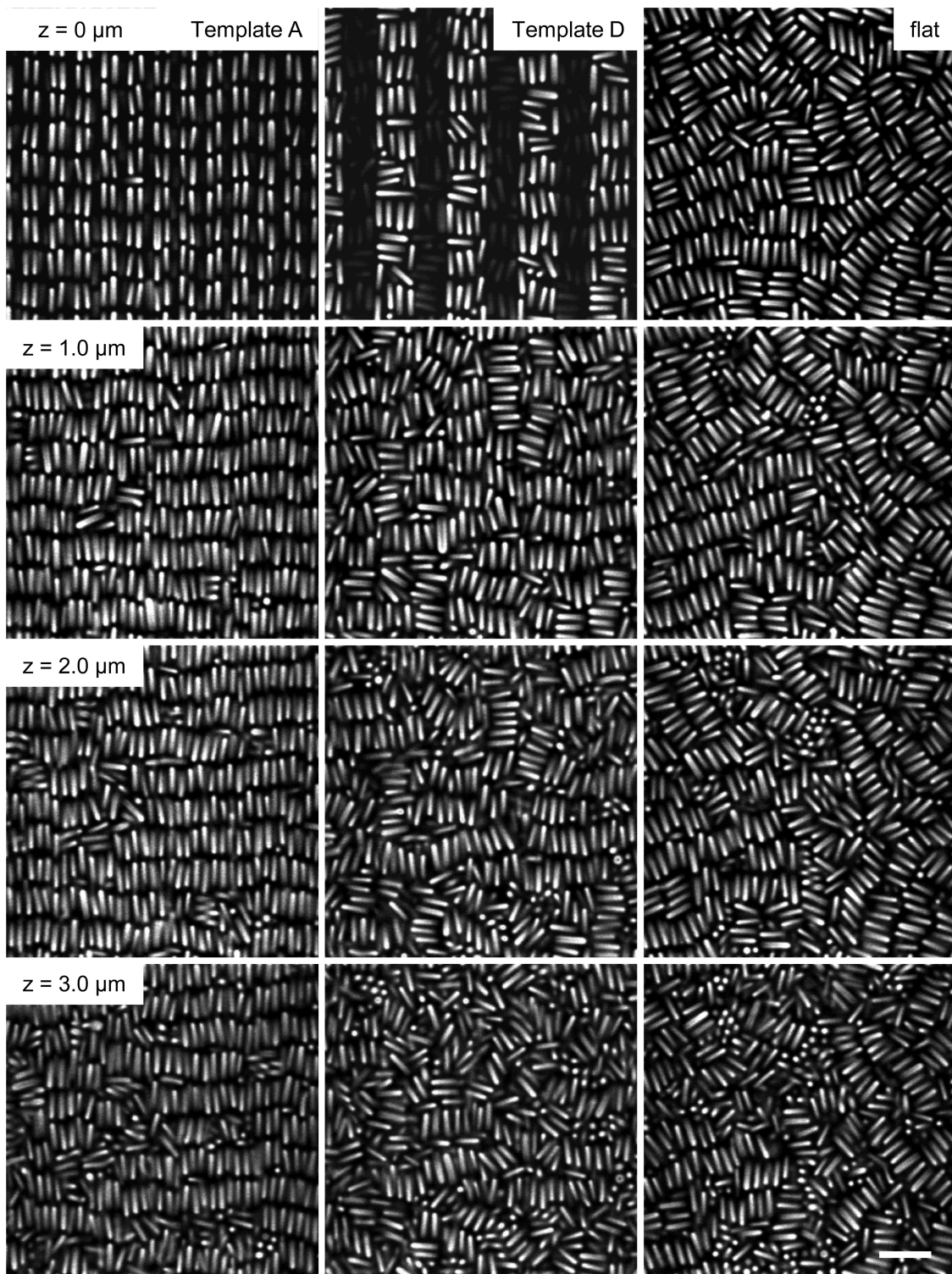


FIGURE 7.8. Confocal images of a sediment of B48 on different templates at 4 different heights. An aligned smectic was formed above template A. Trench widths larger than the rod-length induced more orientational order than in sediments that formed on a flat wall, but not as much as the narrower template. Scale bar indicates $5 \mu\text{m}$.

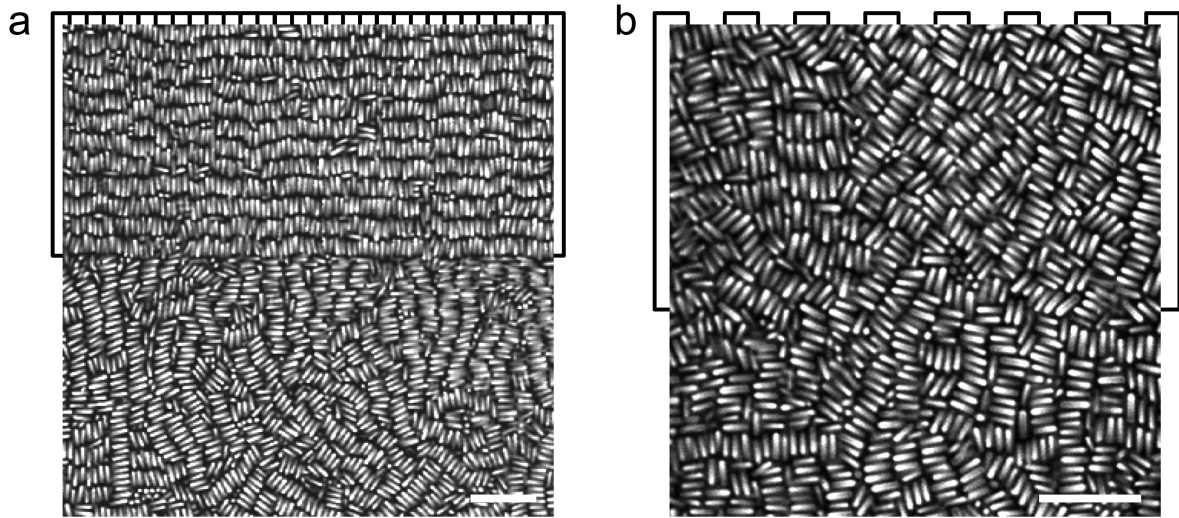


FIGURE 7.9. Confocal images several microns up in the sediment at the edge of the template. (a) B48 on template A ($h \times w \times d = 0.61 \times 2.0 \times 0.5 \mu\text{m}$). (b) B47 on template B ($h \times w \times d = 0.61 \times 3.3 \times 3.5 \mu\text{m}$). For short rods only trenches less than one rod-length wide influenced the alignment of the sediment. Scale bars indicate $10 \mu\text{m}$.

layers. Yet, as we observed in Chapter 4, the scattering pattern in thick sediments of these rods appears to be that of a smectic- B phase. Therefore, the structure as shown in the right column of Fig. 7.8 might be seen as a strongly defected smectic- B phase. On the other hand, Fig. 5.6 shows that after inducing alignment using an electric field, the phase relaxes back to a more disordered state when the field is turned off. If this phase is a separate stable phase, our measurements as shown in Fig. 7.8 suggest that the smectic- B phase wets the templates wall and that the lowering of free energy for this phase at such a structured wall as compared to a smooth wall is significant. More experiments need to be done to find out what the optimal parameters are and these results also indicate that simulations or theory would be interesting and beneficial to interpret and guide further experimental work.

Also for short rods, the effect of the template is restricted to the template area, with sharp boundaries even higher up from the template, but only for certain templates. Figure 7.9 shows the edge of a template with a trench-width smaller than the length of the rods (a), and one where the trench-width was larger than the length of the rods (b). In the first case, a clear difference was observed for the ordering above and next to the template, while in the second case no difference was observed.

7.4. CONCLUSIONS

Smectic liquid crystal phases that are formed by rods with effective aspect ratios larger than 5 were aligned by templates that consisted of trenches with a depth of

about the rod thickness and for a range of widths and spacings between the trenches. The aligned area was restricted to the template area with sharp boundaries, but the induced order extended almost through the full height of the sediment, and is therefore expected to continue when more particles are used. Trenches with widths up to 2 times the rod length and spacings ranging from 0.5 to 3.5 μm were used to align the smectic phases.

Short rods, which do not easily form layered phases by themselves, were best aligned using a template with trench widths smaller than the rod length. Using these templates orientational order parameters higher than 0.9 were measured in a sediment of nicely stacked layers. When the trench width was larger than the length of the rods, only 70 to 80% of the rods in the trenches became aligned, resulting in a more disordered sediment with an orientational order parameter around 0.6. Still, this was better than the orientational order parameter on a flat wall, which was around 0.1.

Although more experiments need to be performed to find the optimal template parameters, these results suggest that well chosen templates can induce at least alignment of the smectic- B phase and maybe even pre-freezing of this phase.

7.5. ACKNOWLEDGEMENTS

We would like to thank Gijs Vollenbroek at AMOLF and Judith Wijnhoven for the preparation of the master patterns.

Bibliography

- [1] T. Graham. Liquid diffusion applied to analysis. *Philosophical transactions of the royal society of London*, 151:183, 1861.
- [2] R. Brown. A brief account of microscopical observations made in the months of June, July and August, 1827, on the particles contained in the pollen of plants; and on the general existence of active molecules in organic and inorganic bodies. *Phil. Mag.*, 4:161–173, 1828.
- [3] A. Einstein. Über die von der molekularkinetischen theorie der wärme geforderte bewegung von in ruhenden flüssigkeiten suspendierten teilchen. *Ann. Phys.*, 322(8):549–560, 1905.
- [4] J. Perrin. Mouvement brownien et réalité moléculaire. *Ann. Chim. Phys.*, 18:5–114, 1909.
- [5] J. Perrin. *Les atomes*. Alcan, Paris, 1913.
- [6] W. Poon. Colloids as big atoms. *Science*, 304:830–831, 2004.
- [7] A. Vrij, E.A. Nieuwenhuis, H.M. Fijnaut, and W.G.M. Agterof. *Faraday discussions of the chemical society*, 65:101, 1978.
- [8] P. Pusey and W. van Megen. Phase behaviour of concentrated suspensions of nearly hard colloidal spheres. *Nature*, 320:340–342, 1986.
- [9] P.G. de Gennes and J. Prost. *The physics of Liquid Crystals*. Oxford University Press, 2nd edition, 1995.
- [10] G. Friedel. *Ann. Phys.*, 18:273, 1922.
- [11] F. Reinitzer. Beiträge zur kenntniss des cholesterins. *Monatsh. Chem./Chem. Monthly*, 9(1):421–441, 1888.
- [12] O. Lehmann. Über fließende krystalle. *Z. Phys. Chem.*, 4:462472, 1889.
- [13] R. Williams. Optical rotatory effect in nematic liquid phase of p-azoxyanisole. *Phys. Rev. Lett.*, 21:342, 1968.
- [14] H. Zocher. Über freiwillige strukturbildung in solen. *Z. Anorg. Allg. Chem.*, 147:91, 1925.
- [15] F.C. Bawden, N.W. Pirie, J.D. Bernal, and I. Fankuchen. Liquid crystalline substances from virus-infected plants. *Nature*, 138:1051, 1936.
- [16] G. Oster. Two-phase formation in solutions of tobacco mosaic virus and the problem of long-range forces. *J. Gen. Physiol.*, 33:445–473, 1950.
- [17] P.A. Buining and H.N.W. Lekkerkerker. Isotropic-nematic phase separation of a dispersion of organophilic boehmite rods. *J. Phys. Chem.*, 97:11510–11516, 1993.
- [18] F. M. van der Kooij and H. N. W. Lekkerkerker. Formation of nematic liquid crystals in suspensions of hard colloidal platelets. *J. Phys. Chem. B*, 102(40):7829–7832, 1998.
- [19] D. van der Beek and H. N. W. Lekkerkerker. Liquid crystal phases of charged colloidal platelets. *Langmuir*, 20:8582–8586, 2004.
- [20] Zvonimir Dogic and Seth Fraden. Smectic phase in a colloidal suspension of semiflexible virus particles. *Phys. Rev. Lett.*, 78(12):2417–2420, 1997.
- [21] F. Livolant and Y. Bouligand. *J. Phys. (Paris)*, 47:1813, 1986.
- [22] K.M. Keville, E.I. Franses, and J.M. Caruthers. preparation and characterization of monodisperse polymer microspheroids. *Journal of Colloid and Interface Science*, 144:103, 1991.

- [23] C.C. Ho, A. Keller, J.A. Odell, and R.H. Ottewill. Preparation of monodisperse ellipsoidal polystyrene particles. *Colloid Polymer Science*, 271:469, 1993.
- [24] D. Mukhija and M.J. Solomon. Nematic order in suspensions of colloidal rods by application of a centrifugal field. *Soft Matter*, 7:540–545, 2011.
- [25] L. Onsager. The effect of shape on the interaction of colloidal particles. *Ann. N. Y. Acad. Sci.*, 51:627–659, 1949.
- [26] D. Frenkel and B.M. Mulder. *Mol. Phys.*, 55:1171, 1985.
- [27] D. Frenkel, H.N.W. Lekkerkerker, and A. Stroobants. Thermodynamic stability of a smectic phase in a system of hard rods. *Nature*, 332:822–823, 1988.
- [28] H. Löwen. Colloidal dispersions in external fields: recent developments. *J. Phys. Condens. Matter*, 20:404201, 2008.
- [29] B. Comiskey, J.D. Albert, H. Yoshizawa, and J. Jacobson. An electrophoretic ink for all-printed reflective electronic displays. *Nature*, 394:253, 1998.
- [30] U. Dassanayake, S. Fraden, and A. van Blaaderen. Structure of electrorheological fluids. *J. Chem. Phys.*, 112:3851–3858, 2000.
- [31] A. Yethiraj and A. van Blaaderen. A colloidal model system with an interaction tunable from hard sphere to soft and dipolar. *Nature*, 421:513–517, 2003.
- [32] M. Parthasarathy and D. Klingenberg. Electrorheology: mechanisms and models. *Mater. Sci. Eng.*, R17:57, 1996.
- [33] W. Wen, C. Weisbuch, D. Phuong, G. Lu, W. Ge, C. Chan, and P. Sheng. Neutral nanoparticle-based display. *Nanotechnology*, 16:598, 2005.
- [34] J. Zhu, M. Li, W. Meyer, R.H. Ottewill, STS-73 Space Shuttle Crue, W.B. Russel, and P.M. Chaikin. Crystallization of hard sphere colloids in μ -gravity. *Nature (London)*, 387:883, 1997.
- [35] S. Hachisu and K. Takano. Pressure of disorder to order transition in monodisperse latex. *Adv. Colloid and Interface Sci.*, 16:233, 1982.
- [36] R. Piazza, T. Bellini, and V. Degiorgio. Equilibrium sedimentation profiles of screened charged colloids: a test of the hard-sphere equation of state. *Phys. Rev. Lett.*, 71:4267, 1993.
- [37] M.A. Rutgers, J.H. Dunsmuir, J.-Z. Xue, W.B. Russel, and P.M. Chaikin. Measurement of the hard-sphere equation of state using screened charged polystyrene colloids. *Phys. Rev. B*, 53:5043, 1996.
- [38] E. van den Pol, A. Lupascu, P. Davidson, and G.J. Vroege. The isotropic-nematic interface of colloidal goethite in an external magnetic field. *J. Chem. Phys.*, 133:164504, 2010.
- [39] M. Mittal and E.M. Furst. Electric field-directed convective assembly of ellipsoidal colloidal particles to create optically and mechanically anisotropic thin films. *Advanced Functional Materials*, 19:3271–3278, 2009.
- [40] H. Kawamoto. The history of liquid-crystal displays. *Proceedings of the IEEE*, 90:460–500, 2002.
- [41] S. Fraden, G. Maret, D.L.D. Caspar, and R.B. Meyer. Isotropic-nematic phase transition and angular correlations in isotropic suspensions of tobacco mosaic virus. *Phys. Rev. Lett.*, 63:2068–2071, 1989.
- [42] P.A. Buining, A.P. Philipse, and H.N.W. Lekkerkerker. Phase behavior of aqueous dispersions of colloidal boehmite rods. *Langmuir*, 10:2106–2114, 1994.
- [43] O. Pelletier, P. Davidson, C. Bourgeaux, and C. Livage. *J. Europhys. Lett.*, 48:53, 1999.
- [44] H. Maeda and Y. Maeda. *Langmuir*, 11:1446, 1995.

- [45] H. Maeda and Y. Maeda. Liquid crystal formation in suspensions of hard rodlike colloidal particles: Direct observation of particle arrangement and self-ordering behavior. *Physical Review Letters*, 90:018303, 2003.
- [46] C.M. van Kats, P.M. Johnson, J.E.A.M. Meerakker, and A. van Blaaderen. Synthesis of monodisperse high-aspect-ratio colloidal silicon and silica rods. *Langmuir*, 20:11201–11207, 2004.
- [47] A. Mohraz and M.J. Solomon. Direct visualization of colloidal rod assembly by confocal microscopy. *Langmuir*, 21:5298–5306, 2005.
- [48] P.M. Johnson, C.M. van Kats, and A. van Blaaderen. Synthesis of colloidal silica dumbbells. *Langmuir*, 21:11510–11517, 2005.
- [49] A.F. Demirors, P.M. Johnson, C.M. van Kats, A. van Blaaderen, and A. Imhof. Directed self-assembly of colloidal dumbbells with an electric field. *Langmuir*, 26:14466–14471, 2010.
- [50] J. Zhang, H. Liu, Z. Wang, and N. Ming. Au-induced polyvinylpyrrolidone aggregates with bound water for the highly shape-selective synthesis of silica nanostructures. *Chemistry a European Journal*, 14:4374–4380, 2008.
- [51] V.A. Tolpekin, M.H.G. Duits, D. van den Ende, and J. Mellema. Aggregation and breakup of colloidal particle aggregates in shear flow, studied with video microscopy. *Langmuir*, 20:2614–2627, 2004.
- [52] K.A. Dick. *Prog. Cryst. Growth Charact. Mater.*, 54:138, 2008.
- [53] W. Stöber and A. Fink. Controlled growth of monodisperse silica spheres in the micron size range. *Journal of Colloid and Interface Science*, 26:62–69, 1968.
- [54] A. van Blaaderen, J. van Geest, and A. Vrij. Monodisperse colloidal silica spheres from tetraalkoxysilanes: Particle formation and growth mechanism. *Journal of Colloid and Interface Science*, 154:481–501, 1992.
- [55] H. Giesche. Synthesis of monodispersed silica powders ii. controlled growth reaction and continuous production process. *Journal of the European Ceramic Society*, 14:205–214, 1994.
- [56] L Wang, S. Tomura, F. Ohashi, M. Maeda, M. Suzuki, and K. Inukai. Synthesis of single silica nanotubes in the presence of citric acid. *Journal of Materials Chemistry*, 11:1465–1468, 2001.
- [57] M.P. Zheng, Y.P. Jin, L.G. Jin, and M.Y. Gu. Characterization of TiO₂-PVP nanocomposites prepared by the sol-gel method. *J. Mat. Sci. Lett.*, 19:433–436, 2000.
- [58] G.P. van der Beek and M.A. Cohen Stuart. Polymer adsorption and desorption studies via H NMR relaxation of the solvent. *Langmuir*, 7:327–334, 1991.
- [59] A. van Blaaderen and A.P.M. Kentgens. Particle morphology and chemical microstructure of colloidal silica spheres made from alkoxysilanes. *Journal of Non-Crystalline Solids*, 149:161–178, 1992.
- [60] R. Besseling, I. Lucio, E.R. Weeks, and W.C.K. Poon. Quantitative imaging of colloidal flows. *Advances in colloid and interface science*, 146:1–17, 2009.
- [61] A. van Blaaderen. Quantitative real-space analysis of colloidal structures and dynamics with confocal scanning light microscopy. *Progress in colloid and interface science*, 104:59–65, 1997.
- [62] A.D. Dinsmore, E.R. Weeks, V. Prasad, A.C. Levitt, and D.A. Weitz. Three-dimensional confocal microscopy of colloids. *Applied optics*, 40:4152–4159, 2001.
- [63] V. Prasad, D. Semwogerere, and E.R. Weeks. Confocal microscopy of colloids. *J. Phys.: Condens. Matter*, 19:113102, 2007.
- [64] U. Gasser, E.R. Weeks, A. Schofield, P.N. Pusey, and D.A. Weitz. *Science*, 292:258, 2001.

- [65] J.P. Hoogenboom, P. Vergeer, and A. van Blaaderen. A real-space analysis of colloidal crystallization in a gravitational field at a flat bottom wall. *J. Chem. Phys.*, 119:3371–3383, 2003.
- [66] Y.L. Wu, D. Derks, A. van Blaaderen, and A. Imhof. Melting and crystallization of colloidal hard-sphere suspensions under shear. *Proc. Natl. Acad. Sci.*, 106:10564, 2009.
- [67] D. Derks, Y.L. Wu, A. van Blaaderen, and A. Imhof. Dynamics of colloidal crystals in shear flow. *Soft Matter*, 5:1060–1065, 2009.
- [68] M. Minsky. Memoir on inventing the confocal scanning microscope. *Scanning*, 10:128–138, 1988.
- [69] J.B. Pawley. *Handbook of biological confocal microscopy*. Springer, 3rd edition, 2006.
- [70] S.W. Hell. Far-field optical nanoscopy. *Science*, 316:1153–1158, 2007.
- [71] S.W. Hell. Microscopy and its focal switch. *Nature methods*, 6:24–32, 2009.
- [72] Y.C. Ding, P. Xi, and Q.S. Ren. Hacking the optical diffraction limit: review on recent developments of fluorescence nanoscopy. *Chinese science bulletin*, 56:1857–1876, 2011.
- [73] B. Harke, C.K. Ullal, J. Keller, and S.W. Hell. Three-dimensional nanoscopy of colloidal crystals. *Nano Lett.*, 8:1309–1313, 2008.
- [74] M.C. Jenkins and S.U. Egelhaaf. Confocal microscopy of colloidal particles: towards reliable, optimum coordinates. *Advances in colloid and interface science*, 136:65–92, 2008.
- [75] P.J. Lu, P.A. Sims, H. Oki, J.B. Macarthur, and D.A. Weitz. Target-locking acquisition with real-time confocal (tarc) microscopy. *Opt. Express*, 15:8702–8712, 2007.
- [76] P.J. Lu. *Gelation and phase separation of attractive colloids*. Thesis, Harvard University, 2008.
- [77] A. van Blaaderen and A. Vrij. Synthesis and characterization of colloidal dispersions of fluorescent, monodisperse silica spheres. *Langmuir*, 8:2921, 1992.
- [78] N.A.M. Verhaegh and A. van Blaaderen. Dispersions of rhodamine-labeled silica spheres - synthesis, characterization, and fluorescence confocal scanning laser microscopy. *Langmuir*, 10:1427–1438, 1994.
- [79] A.F. Demirörs. *Anisotropic colloids: synthesis and phase behavior of eccentric, dimer and string-like colloids*. Thesis, Utrecht University, 2010.
- [80] G. Bosma, C. Pathmamanoharan, E.H.A. de Hoog, W.K. Kegel, A. van Blaaderen, and H.N.W. Lekkerkerker. *J. Colloid Interface Sci.*, 245:292, 2002.
- [81] T.H. Besseling, M. Hermes, and A. van Blaaderen. Paper on identifying the position and orientation of rods from confocal microscopy data. *in progress*.
- [82] A. Labrosse and A. Burneau. Characterization of porosity of ammonia catalysed alkoxy silane silica. *Journal of Non-crystalline solids*, 221:107–124, 1997.
- [83] C. Vonk, S.M. Oversteegen, and J.E.G.J. Wijnhoven. Synthesis of fluorescent silica-coated gibbsite platelets. *J. Colloid and Interface Science*, 287:521–525, 2005.
- [84] A. Imhof, M. Megens, J.J. Engelberts, D.T.N. de Lang, R. Sprik, and W.L. Vos. Spectroscopy of fluorescein (fitc) dyed colloidal silica spheres. *J. Phys. Chem. B*, 103:1408–1415, 1999.
- [85] A. van Blaaderen and A. Vrij. Synthesis and characterization of monodisperse colloidal organo-silica spheres. *J. Colloid and Interface Science*, 156:1–18, 1993.
- [86] A. van Blaaderen and P. Wiltzius. Real-space structure of colloidal hard-sphere glasses. *Science*, 270:1177–1179, 1995.
- [87] E. Eggen, M. Dijkstra, and R. van Roij. Effective shape and phase behavior of short charged rods. *Phys. Rev. E*, 79:041401, 2009.
- [88] A. Mohraz and M.J. Solomon. Direct visualization of colloidal rod assembly by confocal microscopy. *Langmuir*, 21:5298–5306, 2005.

- [89] L.T. Shereda, R.G. Larson, and M.J. Solomon. Boundary-driven colloidal crystallization in simple shear flow. *Physical review letters*, 105:228302, 2010.
- [90] Y.L. Wu. *Control over colloidal crystallization by shear and electric fields*. Thesis, Utrecht University, 2007.
- [91] G.J. Vroege and H.N.W. Lekkerkerker. Phase transitions in lyotropic colloidal and polymer liquid crystals. *Rep. Prog. Phys.*, 55:1241–1309, 1992.
- [92] M.A. Bates and D. Frenkel. Influence of polydispersity on the phase behavior of colloidal liquid crystals: A monte carlo simulation study. *Journal of Chemical Physics*, 109:6193–6199, 1998.
- [93] A. Stroobants, H.N.W. Lekkerkerker, and T. Odijk. *Macromolecules*, 19:2232, 1986.
- [94] E.M. Kramer and J. Herzfeld. Avoidance model for soft particles. II. positional ordering of charged rods. *Phys. Rev. E*, 61:6872–6878, 2000.
- [95] H. Graf and H. Löwen. *Phys. Rev. E*, 59:1932, 1999.
- [96] P.G. Bolhuis and D. Frenkel. *J. Chem Phys.*, 106:666, 1997.
- [97] Z. Dogic and S. Fraden. Ordered phases of filamentous viruses. *Curr. Opin. Colloid Interface Sci.*, 11:47–55, 2006.
- [98] M.P. Lettinga, E. Barry, and Z. Dogic. Self-diffusion of rod-like viruses in the nematic phase. *Europhysics Letters*, 71:692–698, 2005.
- [99] B.J. Lemaire, P. Davidson, J. Ferré, J.P. Jamet, D. Peterman, P. Panine, I. Dozov, and J.P. Jolivet. Physical properties of aqueous suspensions of goethite (α -FeOOH) nanorods: Part I: In the isotropic phase. *Eur. Phys. J. E*, 13:291–308, 2004.
- [100] B.J. Lemaire, P. Davidson, J. Ferré, J.P. Jamet, D. Peterman, P. Panine, I. Dozov, and J.P. Jolivet. Physical properties of aqueous suspensions of goethite (α -FeOOH) nanorods: Part II: In the nematic phase. *Eur. Phys. J. E*, 13:309–319, 2004.
- [101] E. van den Pol, A.V. Petukhov, D.M.E. Thies-Weessie, D.V. Byelov, and G.J. Vroege. Liquid crystal phase behavior of sterically stabilized goethite. *Journal of Colloid and Interface Science*, 352:354–358, 2010.
- [102] E. van den Pol, A.A. Verhoeff, A. Lupascu, M.A. Diaconeasa, P. Davidson, I. Dozov, B.W.M. Kuipers, D.M.E. Thies-Weesie, and G.J. Vroege. Magnetic-field-induced nematic-nematic phase separation and droplet formation in colloidal goethite. *J. Phys.: Condens. Matter*, 23:194108, 2011.
- [103] S. Boersma. *J. Chem. Phys.*, 32, 1960.
- [104] M.M. Tirado, C.L. Martinez, and J. Garcia de la Torre. Comparison of theories for the translational and rotational diffusion coefficients of rod-like macromolecules. application to short dna fragments. *J. Chem. Phys.*, 81:2047–2052, 1984.
- [105] Z. Dogic, A.P. Philipse, S. Fraden, and J.K.G. Dhont. Concentration-dependent sedimentation of colloidal rods. *Journal of chemical physics*, 113:8368–8380, 2000.
- [106] C.P. Royall, R. van Roij, and A. van Blaaderen. Extended sedimentation profiles in charged colloids: the gravitational length entropy, and electrostatics. *J. Phys.: Condens. Matter*, 17:2315–2326, 2005.
- [107] J.C. Crocker and D.G. Grier. Methods of digital video microscopy for colloidal studies. *J. Colloid Interface Sci.*, 179:298, 1996.
- [108] A.V. Petukhov, J.H.H. Thijssen, D.C. 't Hart, A. Imhof, A. van Blaaderen, I.P. Dolbnya, A. Snigirev, A. Moussaid, and I. Snigireva. Microradian x-ray diffraction in colloidal photonic crystals. *J. Appl. Crystallogr.*, 39:137–144, 2006.

- [109] A. Snigirev, V. Kohn, I. Snigireva, and B. Lengeler. A compound refractive lens for focusing high energy x-rays. *Nature*, 384:49–51, 1996.
- [110] V. Kohn, I. Snigireva, and A. Snigirev. Diffraction theory of imaging with compound refractive lens. *Optics Communications*, 216:247–260, 2003.
- [111] M. Drakopoulos, A. Snigirev, I. Snigireva, and J. Schilling. X-ray high resolution diffraction using refractive lenses. *Appl. Phys. Lett.*, 86:014102, 2005.
- [112] S.V. Savenko and M. Dijkstra. Sedimentation and multiphase equilibria in suspensions of colloidal hard rods. *Phys. Rev. E*, 70:051401, 2004.
- [113] E. Grelet. Hexagonal order in crystalline and columnar phases of hard rods. *PRL*, 100:168301, 2008.
- [114] C. Murray. *Experimental studies of melting and hexatic order in two-dimensional colloidal suspensions*, in: *Bond-orientational order in condensed matter systems*. Springer-Verlag, New York, 1992.
- [115] H. Maeda and Y. Maeda. Measurement of density distributions for colloidal β -FeOOH rods in suspensions exhibiting phase separations: the role of long-range forces in smectic ordering. *J. Chem. Phys.*, 121:12655, 2004.
- [116] E. van den Pol, D.M.E. This-Weesie, A.V. Petukhov, G.J. Vroege, and K. Kvashnina. Influence of polydispersity on the phase behavior of colloidal goethite. *J. Chem. Phys.*, 129:164715, 2008.
- [117] D.J. Courtemanche, T.A. Pasmore, and F. van Swol. A molecular-dynamics study of prefreezing hard-spheres at a smooth hard-wall. *Molecular Physics*, 80:861–875, 1993.
- [118] M. Dijkstra. Capillary freezing or complete wetting of hard spheres in a planar hard slit? *PRL*, 93:108303, 2004.
- [119] S. Dietrich. *Phase transitions and critical phenomena*. Academic Press, London, 1988.
- [120] M. Dijkstra, R. van Roij, and R. Evans. Wetting and capillary nematization of a hard-rod fluid: a simulation study. *PRE*, 63:051703, 2001.
- [121] L Harnau and S. Dietrich. Wetting and capillary nematization of binary hard-platelet and hard-rod fluids. *Phys. Rev. E*, 66:051702, 2002.
- [122] Y. Iwashita and H. Tanaka. Pattern evolution of an edge-dislocation array in a lyotropic lamellar phase confined in a wedge-shaped cell: defect formation, relaxation and recombination. *Phys. Rev. E*, 77:041706, 2008.
- [123] R. van Roij, P. Bolhuis, B. Mulder, and D. Frenkel. Transverse interlayer order in lyotropic smectic liquid crystals. *Physical Review E*, 52:1277–1281, 1995.
- [124] J.S. van Duijnvelde and M.P. Allen. Free energy barriers for interlayer diffusion in the smectic-a phase of hard spherocylinders. *Molecular Physics*, 90:243–250, 1997.
- [125] H. Löwen. Anisotropic self-diffusion in colloidal nematic phases. *Phys. Rev. E*, 59:1989–1995, 1999.
- [126] E. Grelet, M.P. Lettinga, M. Bier, R. van Roij, and P. van der Schoot. Dynamical and structural insights into the smectic phase of rod-like particles. *J. Phys.: Condens. Matter*, 20:494213, 2008.
- [127] M.P. Lettinga and E. Grelet. Self-diffusion of rodlike viruses through smectic layers. *Phys. Rev. Lett.*, 99:197802, 2007.
- [128] M.P.B. van Bruggen, H.N.W. Lekkerkerker, and J.K.G. Dhont. Long-time translational self-diffusion in isotropic dispersions of colloidal rods. *Phys. Rev. E*, 56:4394–4403, 1997.
- [129] M.P.B. van Bruggen, H.N.W. Lekkerkerker, G. Maret, and J.K.G. Dhont. Long-time translational self-diffusion in isotropic and nematic dispersions of colloidal rods. *Phys. Rev. E*, 58:7668–7677, 1998.

- [130] R. Matena, M. Dijkstra, and A. Patti. Non-gaussian dynamics in smectic liquid crystals of parallel hard rods. *Physical Review E*, 81:021704, 2010.
- [131] A. Patti, D. El Masri, R. van Roij, and M. Dijkstra. Collective diffusion of colloidal hard rods in smectic liquid crystals: Effect of particle anisotropy. *Journal of Chemical Physics*, 132:224907, 2010.
- [132] V.J. Anderson and H.N.W. Lekkerkerker. Insights into transition kinetics from colloids science. *Nature*, 416:811–815, 2002.
- [133] E.D. Morrison. Synthesis of vanadium oxide colloidal dispersions for antistatic coatings. *Mater. Res. Soc. Symp. Proc.*, 432:121–131, 1997.
- [134] Y. Vlasov, X. Bo, J. Sturm, and D. Norris. On-chip natural assembly of silicon photonic bandgap crystals. *Nature*, 414:289, 2001.
- [135] A. Gast and C. Zukoski. Electrorheological fluids as colloidal suspensions. *Adv. Colloid Interf. Sci.*, 30:153, 1989.
- [136] J.D. Forster, J.G. Park, M. Mittal, H. Noh, C.F. Schreck, C.S. O’Hern, H. Cao, E.M. Furst, and E.R. Dufresne. Assembly of optical-scale dumbbells into dense photonic crystals. *ACS Nano*, 5:6695–6700, 2011.
- [137] S.P. Stoylov. *Colloid electro-opticals, theory, techniques, applications*. Academic Press: New York, 1991.
- [138] B.M.I. van der Zande, G.J.M. Koper, and H.N.W. Lekkerkerker. Alignment of rod-shaped gold particles by electric fields. *J. Phys. Chem. B*, 103:5754–5760, 1999.
- [139] A.M. Zhivkov, B.M.I. van der Zande, and S.P. Stoylov. Electro-optics of metal particles: electric birefringence of gold rods. *Colloids and Surfaces A: Physicochem. Eng. Aspects*, 209:299–303, 2002.
- [140] K. Kang. Diffusivity in an electric-field-induced homeotropic phase of charged colloidal rods. *EPL*, 92:18002, 2010.
- [141] K. Kang and J.K.G. Dhont. Double-layer polarization induced transitions in suspensions of colloidal rods. *EPL*, 84:14005, 2008.
- [142] J.K.G. Dhont and K. Kang. Electric-field-induced polarization and interactions of uncharged colloids in salt solutions. *Eur. Phys. J. E*, 33:51–68, 2010.
- [143] M. Rotunno, T. Bellini, Y. Lansac, and M.A. Glaser. Phase behavior of polarizable spherocylinders in external fields. *Journal of Chemical Physics*, 121:5541–5549, 2004.
- [144] M.P.B. van Bruggen and H.N.W. Lekkerkerker. Metastability and multistability: gelation and liquid crystal formation in suspensions of colloidal rods. *Langmuir*, 18:7141–7145, 2002.
- [145] H. Ma, W. Wen, W.Y. Tam, and P. Sheng. Dielectric electrorheological fluids: theory and experiment. *Adv. Phys.*, 52:343, 2003.
- [146] J. Venermo and A. Sihvola. Dielectric polarizability of circular cylinder. *Journal of Electrostatics*, 63:101–117, 2005.
- [147] A.-P. Hynninen and M. Dijkstra. Phase diagram of dipolar hard and soft spheres: manipulation of colloidal crystal structures by an external field. *Phys. Rev. Lett.*, 94:138303, 2005.
- [148] A.-P. Hynninen and M. Dijkstra. Phase behavior of dipolar hard and soft spheres. *Phys. Rev. E*, 72:051402, 2005.
- [149] *CRC Handbook of Chemistry and Physics*. CRC Press, 92nd edition, 2011.
- [150] S. Hess. Fokker-planck-equation approach to flow alignment in liquid crystals. *Z. Naturforsch.*, 31:1034–1037, 1976.
- [151] M. Doi. *J. Polym. Sci., Polym. Phys. Ed.*, 19:229, 1981.

- [152] M. Doi and S.F. Edwards. *The theory of polymer dynamics*. Clarendon Press: Oxford, U.K., 1986.
- [153] S. Hess and M. Kröger. Regular and chaotic orientational and rheological behaviour of liquid crystals. *J. Phys. Condens. Matter*, 16:S3835–S3859, 2004.
- [154] G. Marrucci and P.L. Maffettone. Description of the liquid-crystalline phase of rodlike polymers at high shear rates. *Macromolecules*, 22:4076–4082, 1989.
- [155] R.G. Larson. Arrested tumbling in shearing flows of liquid crystal polymers. *Macromolecules*, 23:3983–3992, 1990.
- [156] R.G. Larson and H.C. Öttinger. Effect of molecular elasticity on out-of-plane orientations in shearing flows of liquid-crystalline polymers. *Macromolecules*, 24:6270–6282, 1991.
- [157] W.R. Burghardt and G.G. Fuller. Role of director tumbling in the rheology of polymer liquid crystal solutions. *Macromolecules*, 24:2546, 1991.
- [158] M. Grosso, S. Crescitelli, E. Somma, J. Vermant, P. Moldenaers, and P.L. Maffettone. Prediction and observation of sustained in a shear liquid crystalline polymer. *Phys. Rev. Lett.*, 90:098304, 2003.
- [159] J. Mewis, M. Mortier, J. Vermant, and P. Moldenaers. Experimental evidence for the existence of a wagging regime in polymeric liquid crystals. *Macromolecules*, 30:1323–1328, 1997.
- [160] M.P. Lettinga, Z. Dogic, H. Wang, and J. Vermant. Flow behavior of colloidal rodlike viruses in the nematic phase. *Langmuir*, 21:8048, 2005.
- [161] M.P. Lettinga and J.K.G. Dhont. Non-equilibrium phase behaviour of rod-like viruses under shear flow. *J. Phys.: Condens. Matter*, 16:S3929, 2004.
- [162] Y. Tao, W.K. den Otter, and W.J. Briels. Kayaking and wagging of rods in shear flow. *Phys. Rev. Lett.*, 95:237802, 2005.
- [163] Y.G. Tao, W.K. den Otter, and W.J. Briels. Periodic orientational motions of rigid liquid-crystalline polymers in shear flow. *J. Chem. Phys.*, 124:204902, 2006.
- [164] Y.G. Tao, W.K. den Otter, and W.J. Briels. Kayaking and wagging of liquid crystals under shear: comparing director and mesogen motions. *EPL*, 86:56005, 2009.
- [165] N. Mori, H. Fujioka, and R. and Semura. Brownian dynamics simulations for suspension of ellipsoids in liquid crystalline phase under simple shear flows. *Rheologica acta*, 42:102–109, 2003.
- [166] G.K. Auernhammer, H.R. Brand, and H. Pleiner. Shear-induced instabilities in layered liquids. *Phys. Rev. E*, 66:061707, 2002.
- [167] I.W. Stewart and F. Stewart. Shear flow in smectic A liquid crystals. *J. Phys.: Condens. Matter*, 21:465101, 2009.
- [168] C.R. Safinya, E.B. Sirota, R.F. Bruinsma, C. Jeppesen, R.J. Plano, and L.J. Wenzel. Structure of membrane surfactant and liquid crystalline smectic lamellar phases under flow. *Science*, 261:588–591, 1993.
- [169] H. Leist, D. Maring, T. Thurn-Albrecht, and U. Wiesner. Double flip of orientation for a lamellar diblock copolymer under shear. *J. Chem. Phys.*, 110:8225–8228, 1999.
- [170] P. Panizza, P. Archambault, and D. Roux. Effects of shear on the smectic A phase of thermotropic liquid crystals. *J. Phys. II*, 5:303, 1995.
- [171] G.R. Luckhurst, G. Saielli, and T.J. Sluckin. Shear-induced structural changes of a smectic-A phase: a computer simulation study. *Phys. Rev. E*, 65:041717, 2002.
- [172] N.J. Mottram, T.J. Sluckin, S.J. Elston, and M.J. Towler. Shear-induced melting of smectic-A liquid crystals. *Phys. Rev. E*, 62:5064–5080.

- [173] M. Cagnon and G. Durand. Positional anchoring of smectic liquid crystals. *Phys. Rev. Lett.*, 70:2742–2745, 1993.
- [174] N. Duff and D.J. Lacks. Shear-induced crystallization in jammed systems. *Phys. Rev. E*, 75:031501, 2007.
- [175] P.A. Smith, G. Petekidis, S.U. Egelhaaf, and W.C.K. Poon. Yielding and crystallization of colloidal gels under oscillatory shear. *Phys. Rev. E*, 76:041402, 2007.
- [176] B.J. Ackerson and P.N. Pusey. Shear-induced order in suspensions of hard spheres. *Phys. Rev. Lett.*, 61:1033, 1988.
- [177] J. Cognard. Alignment of nematic liquid-crystals and their mixtures. *J. Molec. Cryst. Liq. Cryst.*, 51:1–77, 1982.
- [178] B. Jerome. Surface effects and anchoring in liquid crystals. *Reports on Progress in Physics*, 54:391, 1991.
- [179] H. Zocher. Über die optische Anisotropie selektiv absorbierender stoffe und uber mechanische Erzeugung von Anisotropie. *Naturwissenschaften*, 13:1015–1021, 1925.
- [180] J. Hoogboom, T. Rasing, A.E. Rowan, and R.J.M. Nolte. LCD alignment layers. Controlling nematic domain properties. *J. Mater. Chem.*, 16:1305–1314, 2006.
- [181] S. Ishihara. How far has the molecular alignment of liquid crystals been elucidated? *J. Display Technol.*, 1:30–40, 2005.
- [182] A. van Blaaderen, R. Ruel, and P. Wiltzius. Template-directed colloidal crystallization. *Nature*, 385:321, 1997.
- [183] J.P. Hoogenboom, A.K. van Langen-Suurling, J. Romijn, and A. van Blaaderen. Hard-sphere crystals with hcp and non-close-packed structure grown by colloidal epitaxy. *Phys. Rev. Lett.*, 90:138301, 2003.
- [184] A. van Blaaderen and P. Wiltzius. Growing large, well-oriented colloidal crystals. *Adv. Mater.*, 9:833, 1997.
- [185] J.P. Hoogenboom, A.K. Langen-Suurling, J. Romijn, and A. van Blaaderen. Epitaxial growth of a colloidal hard-sphere hcp crystal and the effects of epitaxial mismatch on crystal structure. *Phys. Rev. E*, 69:051602, 2004.
- [186] K.H. Lin, J.C. Crocker, V. Prasad, A. Schofield, D.A. Weitz, T.C. Lubensky, and A.G. Yodh. Entropically driven colloidal crystallization on patterned surfaces. *Phys. Rev. Lett.*, 85:1770, 2000.
- [187] M. Dijkstra and R. van Roij. Entropic wetting in colloidal suspensions. *J. Phys.: Condens. Matter*, 17.
- [188] M. Heni and H. Löwen. Surface freezing on patterned substrates. *Phys. Rev. Lett.*, 85:3668–3671, 2000.
- [189] M. Heni and H. Löwen. Precrystallization of fluids induced by patterned substrates. *J. Phys. Condens. Matter.*, 13:4675–4696, 2001.
- [190] L. Harnau, F. Penna, and S. Dietrich. Colloidal hard-rod fluids near geometrically structured substrates. *Phys. Rev. E*, 70:021505, 2004.
- [191] Y. Xia and G. Whitesides. Soft lithography. *Angew. Chem. Int. Ed.*, 37:550, 1998.
- [192] E.C.M. Vermolen. *Manipulation of colloidal crystallization*. Thesis, Utrecht University, 2008.

Summary

This thesis treats colloidal silica rods. In particular, it deals with the synthesis and characterization of fluorescent silica rods for confocal laser scanning microscopy studies in part 1, and with the study of the phase behavior of these particles in several external fields in part 2.

Although the experimental study of spherical colloids has been extensive, similar studies on rod-like particles are rare because suitable model systems are scarce. To fulfill this need, we presented the synthesis of monodisperse rod-like silica colloids with tunable dimensions in **Chapter 2**. Rods were produced with diameters of 200 nm and larger and lengths up to 10 μm , which resulted in aspect ratios ranging from 1 to 25. The longer aspect ratio rods formed both nematic and smectic liquid crystal phases. The growth mechanism of these rods involves emulsion droplets of water in pentanol, inside which silica condensation takes place. Since the silica nucleus is attached to the water/pentanol interface, the supply of reactants to the nucleus is anisotropic, causing it to grow on one side only, which results in rod formation. The material properties of the resulting silica rods were compared to those of Stöber silica spheres by methods such as NMR and porosimetry.

The silica rods as prepared in Chapter 2 were made suitable for quantitative real-space studies by ‘conventional’ confocal laser scanning microscopy. In **Chapter 3**, we presented and discussed several methods of fluorescent labeling to prepare rods with different fluorescent patterning, ranging from constant fluorescence levels to gradients from one rod-end to the other, and even patterns of two colors. Single particle imaging was achieved by creating core-shell rods that had a fluorescent core and a non-fluorescent shell. Alternatively, the rods could be coated with 3-(trimethoxysilyl)propyl methacrylate or octadecyltrimethoxysilane and dispersed in a solvent with a low dielectric constant to induce micron-sized double layers. To enable quantitative measurements, a tracking algorithm was developed that identifies the rods’ positions and orientations in 2D optical slices. Initial testing of the method showed that projected 2D orientational order parameters can be used to assess the 3D orientational order parameter in both dilute and strongly interacting systems.

In the second part of the thesis, the newly developed model system was used to study the phase behavior of rods in external fields. In **Chapter 4**, colloidal silica rods with aspect ratios ranging from 3.6 to 8.0 were studied in the gravitational field. Besides the expected nematic and smectic liquid crystalline phases for the higher aspect

ratios, we found a smectic- B phase at high densities for all systems. By combining real-space confocal laser scanning microscopy and small angle X-ray scattering methods, a phase diagram depending on concentration and aspect ratio was constructed, which shows good qualitative agreement with simulation results in the literature for hard spherocylinder systems. Additionally, real-space measurements on the single-particle level provided preliminary information on defects and dynamics.

In **Chapter 5**, the effect of external electric fields on the behavior of colloidal rods in dilute and concentrated dispersions is described. In the dilute regime, the rods aligned themselves with the applied field due to an induced dipole moment. By measuring the distribution of orientations of the rods with confocal microscopy, the polarization of the rods was determined. The results can be described with a theoretical model for the polarization of ellipsoids. In more concentrated dispersions, external electric fields were used to influence the phase behavior of the rods. Para-nematic phases were induced this way, as well as well-aligned smectic phases with a decreased number of defects. At high field strengths, a new crystal structure was observed that consisted of strings of rods ordered in a hexagonal pattern in which neighboring rods were shifted by a third of their length in height.

Steady shear flow was successfully applied to align rod-like silica particles with an aspect ratio of 6 in **Chapter 6**. Shear induced nematic, columnar and smectic liquid crystal phases were created that were aligned with their director in the flow direction. Upon application of steady shear to rods in an isotropic phase, a shear induced para-nematic was almost instantly formed. After sufficient sedimentation, the alignment induced by the shear was maintained in the sample when the shear was stopped and upon further sedimentation a shear aligned smectic- B phase was formed. When the shear was continuously applied during sedimentation a columnar phase was formed, with its director pointing in the velocity-direction. The application of oscillatory shear led to the formation of smectic-like domains in a sample that was previously in a shear aligned nematic state. Although the experiments described in Chapter 6 are only preliminary, they give a strong indication that shear is a powerful external field to align colloidal liquid crystal phases over larger areas.

To conclude, templates were used to direct sedimenting rods in **Chapter 7**. Smectic liquid crystal phases that were formed spontaneously by rods with aspect ratios larger than 5 were aligned successfully by colloidal epitaxy. Templates consisting of trenches of various widths (up to 2 times the length of the rods) and spacings ranging from 0.5 to 3.5 μm were used to align the smectic phases. The area with well aligned rods was restricted to the template area with sharp boundaries. For rods with effective aspect ratios smaller than 4, which do not form smectics spontaneously, templates with trench widths smaller than the rod length were used to induce the formation of an aligned

smectic-*B* phase. Larger trench widths did induce more order than was measured in sediments on a flat wall, but less than induced by the narrow trenches.

Samenvatting voor iedereen

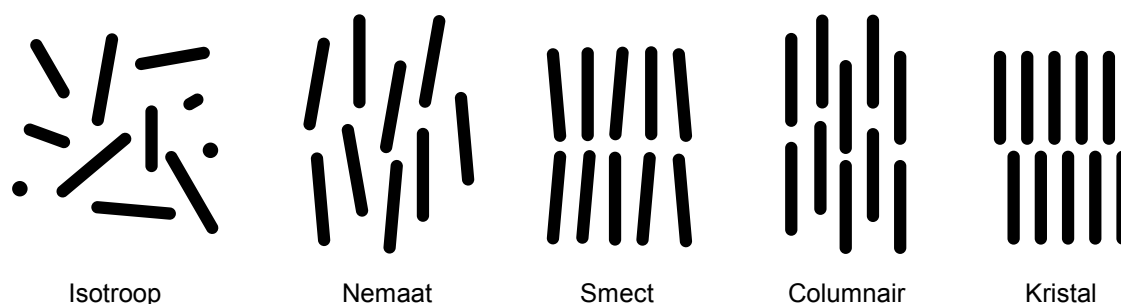
Zoals de titel al aangeeft: dit proefschrift gaat over colloïdale silicastaafjes. Maar wat zijn colloïden eigenlijk? En wat is er zo interessant aan staafjes? Het antwoord op deze vragen wordt hieronder gegeven, evenals een samenvatting van de resultaten van het onderzoek.

COLLOÏDEN

Colloïden zijn kleine deeltjes met afmetingen tussen enkele nanometers (een miljoenste millimeter) en enkele micrometers (een duizendste millimeter). Ter vergelijking: de dikte van een haar is ongeveer 100 micrometer. Colloïden zijn dus heel klein, maar wel groot genoeg om ze te bestuderen met een microscoop. De term ‘colloïd’ komt van het Griekse *κoλλα*, dat ‘lijm’ betekent. Deze naam is in 1861 bedacht door Thomas Graham, die een plakkerig goedje vond toen hij een waterige oplossing door perkament filterde. De deeltjes die aan het perkament bleven plakken noemde hij colloïden. Colloïden zijn terug te vinden in veel producten die we iedere dag gebruiken. We eten ze, drinken ze en smeren ze op onze huid of muur, ze stromen zelfs door onze aderen. Mayonaise, melk, crèmes, verf en bloed zijn voorbeelden van colloïdale systemen. Omdat ze in zoveel producten voorkomen, is het bestuderen van colloïden belangrijk voor verschillende takken van industrie. Maar naast hun toepassing in industriële producten, worden colloïden in de wetenschap gebruikt als modelsysteem voor atomen en moleculen. Doordat ze groot genoeg zijn om ze met een gewone lichtmicroscoop te kunnen zien en tegelijkertijd klein genoeg om zich in bepaalde opzichten hetzelfde te gedragen als atomen en moleculen, zijn colloïden een ideaal modelsysteem.

VLOEIBARE KRISTALLEN

Net als atomen en moleculen, komen colloïden voor in verschillende toestanden (fases), die afhangen van de concentratie deeltjes. Als de concentratie heel laag is vormen de deeltjes een gas, bij iets hogere concentratie ontstaat een vloeistof en bij de hoogste concentraties vormt zich een kristal. Ook kan er bij hoge concentraties een glasfase ontstaan, wanneer de deeltjes niet genoeg tijd krijgen om zich te ordenen. Iets bijzonders gebeurt er wanneer de deeltjes erg anisotroop zijn (uitgerekt zoals een staafje bijvoorbeeld, of juist plat zoals een schijf). Deze deeltjes kunnen een keur aan fases vormen met eigenschappen die tussen die van de vloeistof- en de kristalfase inliggen.



FIGUUR 1. Schematische weergave van staafjes in verschillende vloeibare kristalfases.

Deze fases worden vloeibare kristallen genoemd en ze kunnen worden ingedeeld in drie klassen: de nematen, de smecten en de columnaire fases. Een schematische weergave van deze fases is afgebeeld in figuur 1.

Voor staafjes wordt de pure vloeistoffase de isotrope fase genoemd. In deze fase hebben alle staafjes een willekeurige oriëntatie en positie. Volledige orde daarentegen, is er in de kristallijne fase, waarin zowel de oriëntatie als de positie van de staafjes geordend is. De vloeibare kristalfases liggen qua ordening tussen de isotrope en kristallijne fase in. De fase die het meest lijkt op de isotrope fase is de nematische fase. In deze fase wijzen de staafjes gemiddeld allemaal dezelfde kant op, terwijl hun posities nog steeds willekeurig verdeeld zijn. In de smectische fase wijzen de staafjes ook dezelfde kant op, en vormen ze bovendien lagen. Binnen de lagen gedragen de staafjes zich nog steeds als een vloeistof, ze hebben in dat opzicht dus nog een willekeurige positie in twee van de drie richtingen. De columnaire fase bestaat uit kolommen van staafjes, waarbij er binnen de kolommen geen orde is, maar de kolommen onderling wel geordend zijn.

Vloeibare kristallen werden voor het eerst waargenomen in 1888, in een systeem van cholesterolderivaten. Later is ontdekt dat deze fases voorkomen in veel meer systemen: langgerekte organische moleculen bijvoorbeeld. In 1920 werden vloeibare kristalfases voor het eerst gezien in colloïdale systemen. Sindsdien worden colloïden veel gebruikt om deze fases te onderzoeken. Systemen die hiervoor vaak gebruikt worden zijn kleideeltjes zoals goethiet en gibbsiet, maar ook biologische systemen zoals een aantal virussen en DNA worden veel gebruikt. Er zijn echter maar weinig systemen waarbij de anisotrope deeltjes individueel met (confocale) microscopie bestudeerd kunnen worden. De in dit proefschrift beschreven colloïdale staafjes zijn een mooie aanvulling op de verzameling van anisotrope colloïden die individueel bestudeerd kunnen worden. In tegenstelling tot veel andere systemen vormen onze staafjes zowel nematische als smectische fases.

HET MAKEN VAN SILICASTAAFJES

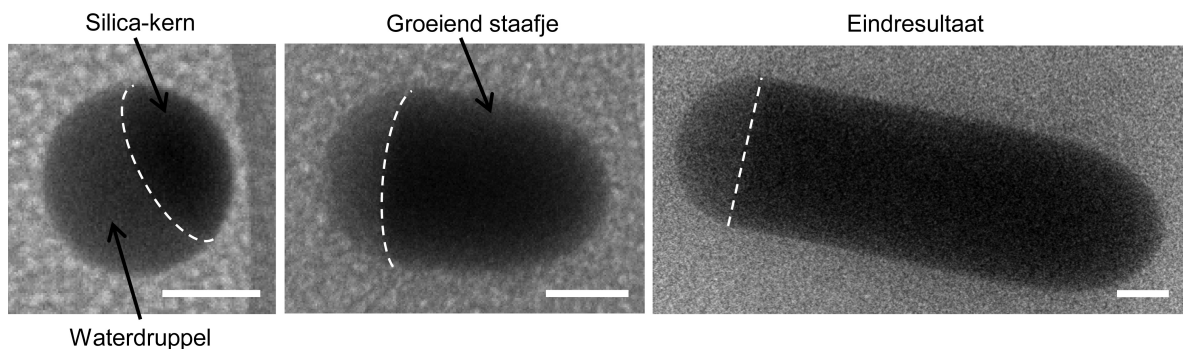
In het eerste deel van dit proefschrift, Hoofdstuk 2 en 3, is beschreven hoe silicastaafjes gemaakt worden en hoe ze bewerkt worden om ze als modelsysteem voor confocale microscopiestudies te gebruiken.

Synthese van silicastaafjes

De synthese van silicastaafjes, zoals beschreven in Hoofdstuk 2, geschiedt op een heel eenvoudige manier; alle benodigde chemicaliën worden in de juiste verhouding samengevoegd, goed geschud en vervolgens met rust gelaten tot de staafjes zich hebben gevormd. Tijdens het schudden ontstaan er kleine waterdruppeltjes in de vloeistof, waaruit de staafjes groeien. De stof waaruit de staafjes worden opgebouwd lost namelijk veel beter op in water dan in de omringende vloeistof. Vervolgens vormt zich een klein silica deeltje aan het oppervlak van zo'n waterdruppel. Nieuw silica kan dan alleen vanuit de waterdruppel aangroeien, waardoor de silica kern als het ware uit de druppel wordt geduwd (zie figuur 2). Hierdoor ontstaat er een staafvormig deeltje. De lengte van de staafjes kan op een aantal manieren beïnvloed worden (bijvoorbeeld door de concentraties van de chemicaliën te veranderen), zodat we staafjes van een paar honderd nanometer tot ongeveer 10 micrometer lang kunnen maken. Wanneer de reactie verstoord wordt, kunnen deeltjes met een andere vorm ontstaan. Zo zijn er bijvoorbeeld bollen gemaakt, kronkelige staafjes, lange structuren met uitstulpingen die op doortakken lijken, deeltjes die lijken op een lisdodde en zelfs een soort poppetjes die bestaan uit een staafje met een bolschil aan een uiteinde.

Aanpassen voor confocale microscopie

Voor het bestuderen van colloïden worden al jarenlang silica bollen gebruikt. Nu we een manier hebben gevonden om staafjes te maken van hetzelfde materiaal, willen we deze op dezelfde manier bestuderen als de bollen. Hiervoor wordt confocale microscopie gebruikt, een techniek waarbij een laser wordt gebruikt om de deeltjes te belichten



FIGUUR 2. De groei van een silicastaafje uit een waterdruppel. De schaallijn geeft 100 nm weer.

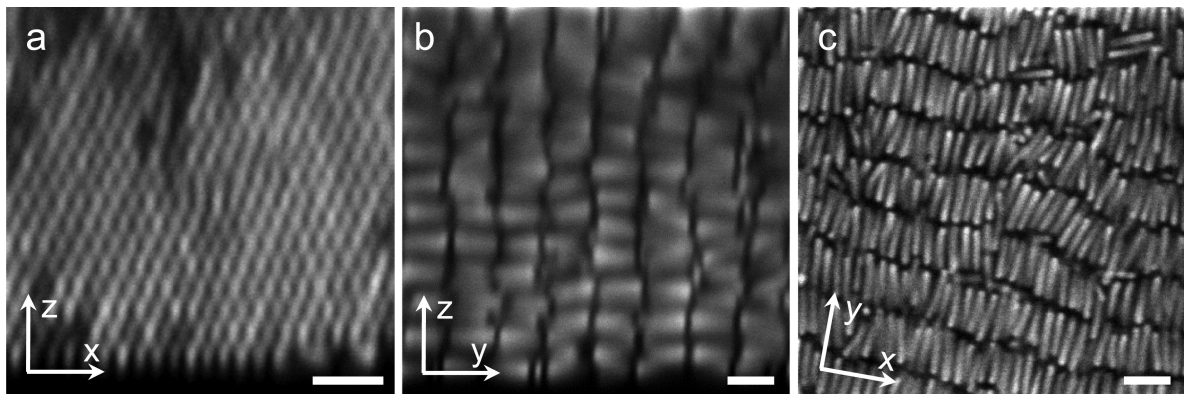
zodat ze op een andere golflengte gaan fluoresceren. Om deze techniek op de staafjes toe te passen moet er een fluorescente stof worden ingebouwd. In Hoofdstuk 3 staan verschillende manieren om dit te bereiken, die elk hun eigen fluorescente patroon tot gevolg hebben. Naast het inbouwen van de fluorescente stof moet er ook voor gezorgd worden dat de fluorescente delen ver genoeg uit elkaar zitten om aparte deeltjes te kunnen onderscheiden in plaats van één fluorescente zee. Dit kan bijvoorbeeld bereikt worden door de deeltjes te bedekken met een extra laag silica die niet fluorescent is, of door ze zo geladen te maken dat ze elkaar afstoten en op die manier ver genoeg van elkaar blijven.

HET MANIPULEREN VAN HET FASEGEDRAG VAN STAAFJES

In het tweede deel van dit proefschrift wordt aandacht besteed aan de staafjes als modelsysteem voor het bestuderen van het fasegedrag van staafvormige deeltjes. Hierbij is er gebruik gemaakt van externe velden (invloeden van buitenaf) om het fasegedrag te beïnvloeden. Niet alleen vormen externe velden een nuttig instrument om de eigenschappen van colloïden te onderzoeken, ze bieden ook een middel om hun ordening te sturen in een voor toepassingen gewenste richting. Zwaartekracht is bijvoorbeeld een extern veld dat altijd een rol speelt in experimenten die op aarde plaatsvinden. Andere externe velden, zoals elektrische velden, stroming en gestructureerde wanden kunnen worden gebruikt om de fases die de colloïden vormen te beïnvloeden.

Zwaartekracht

In Hoofdstuk 4 is het fasegedrag van staafjes in het zwaartekrachtveld beschreven. Omdat de silicastaafjes een hogere dichtheid hebben dan het oplosmiddel waarin ze zich bevinden, zakken ze onder invloed van de zwaartekracht langzaam naar de bodem. Dit verschijnsel heet sedimentatie. Doordat de staafjes sedimenteren, ontstaat er een verdeling waarbij ze op de bodem heel geconcentreerd zijn en de concentratie hogerop afneemt. Aangezien de vorming van de verschillende fases afhangt van de concentratie, ontstaan er zo meerdere fases in één capillair. In Hoofdstuk 4 zijn de fases van staafjes met een lengte-diameterverhouding variërend van 3.5 tot 8.0 bestudeerd door middel van röntgendiffractie en confocale microscopie. De resultaten zijn samengevat in een fase-diagram dat afhangt van de lengte-diameterverhouding en concentratie van de staafjes. Voor korte staafjes, met een lengte-diameterverhouding kleiner dan 5, zijn er geen vloeibare kristalfases gevonden. Deze deeltjes gedragen zich in feite net als bollen. In systemen van langere staafjes daarentegen, zijn nematische en smectische fases gevonden. In tegenstelling tot wat computersimulaties voorspelden, is er geen kristalfase gevonden bij de hoogste concentraties, maar een smectisch-*B* fase (zie figuur 3 voor een voorbeeld van deze fase). Naast het bepalen van het fase-diagram biedt ons nieuwe systeem voor het eerst de mogelijkheid om de staafjes afzonderlijk af te



FIGUUR 3. Confocale microscopieplaatjes van een smectisch-*B* fase. (a) Een verticale doorsnede door één van de lagen laat zien dat de staafjes binnen de lagen hexagonaal geordend zijn. (b) Een verticale doorsnede loodrecht op de lagen laat de lagen van onder tot boven zien. (c) Horizontale doorsnede: staafjes in lagen. De schaallijn geeft $3 \mu\text{m}$ weer.

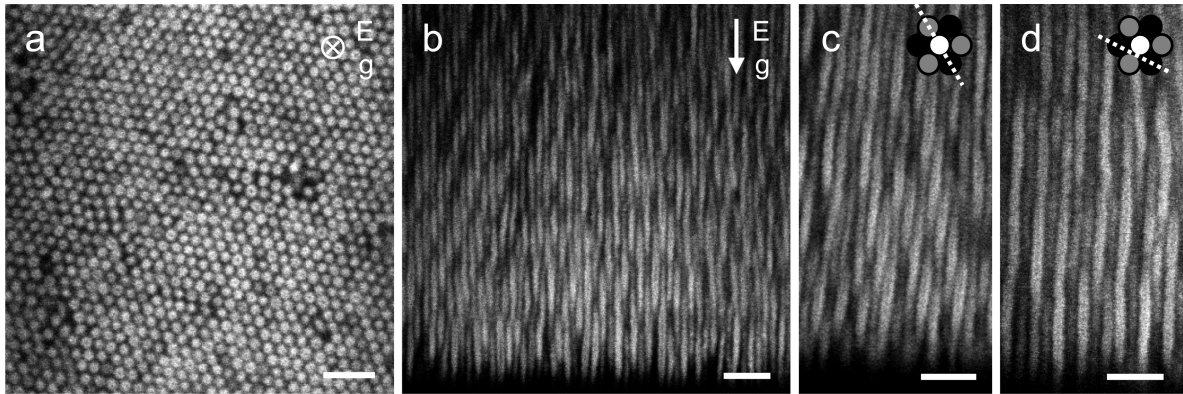
beelden. Hierdoor konden defecten, zoals deeltjes die tussen de lagen gepositioneerd waren, voor het eerst direct worden waargenomen. Ook dynamische aspecten, zoals diffusie, kunnen nu op het niveau van één deeltje worden bestudeerd.

Elektrisch veld

Het fasegedrag van staafjes dat in Hoofdstuk 4 is beschreven kan beïnvloed worden door een elektrisch veld aan te leggen. Wanneer staafjes zich in een elektrisch veld bevinden, worden ze gepolariseerd. Dit betekent dat ze netto aan één kant positief en aan de andere kant negatief geladen zijn. Het gevolg van deze polarisatie is dat de staafjes zich met hun lengte-as in de richting van het veld oriënteren. Door een elektrisch veld aan te leggen is het dus mogelijk een nematische fase te creëren bij concentraties waarbij zonder veld een isotrope fase bestaat. Daarnaast kan het veld gebruikt worden om het aantal defecten in smectische fases te verminderen. Tot slot hebben we een nieuwe kristalstructuur gevonden bij hoge veldsterktes (zie figuur 4). In een hoog elektrisch veld is de geïnduceerde lading van de staafjes zo hoog dat ze niet meer naast elkaar in lagen willen zitten zoals het geval is zonder veld. Hierdoor ontstaat er een structuur waarbij de staafjes nog wel hexagonaal ordenen, maar waarbij buren eenderde van hun lengte in hoogte zijn verschoven.

Stroming

Een tweede manier om vloeibare kristalfases te beïnvloeden is beschreven in Hoofdstuk 6. In dit hoofdstuk is de vloeistof die de colloïden bevat in stroming gebracht door twee platen, waartussen de deeltjes zich bevinden, in tegengestelde richting te bewegen. Door de stroming werden de staafjes in dezelfde richting georiënteerd. Welke fases er vervolgens werden gevonden hing af van hoe lang de stroming was toegepast.



FIGUUR 4. Een nieuwe kristalstructuur van staafjes in een hoog elektrisch veld. (a) Horizontale doorsnede: hexagonale orde in één richting. (b) Vertikale doorsnede: de staafjes zijn eenderde van hun lengte verschoven ten opzichte van hun burens. (c) en (d) Vertikale doorsnedes onder verschillende hoeken. De schaallijn geeft $5 \mu\text{m}$ weer in a en $3 \mu\text{m}$ in b-d.

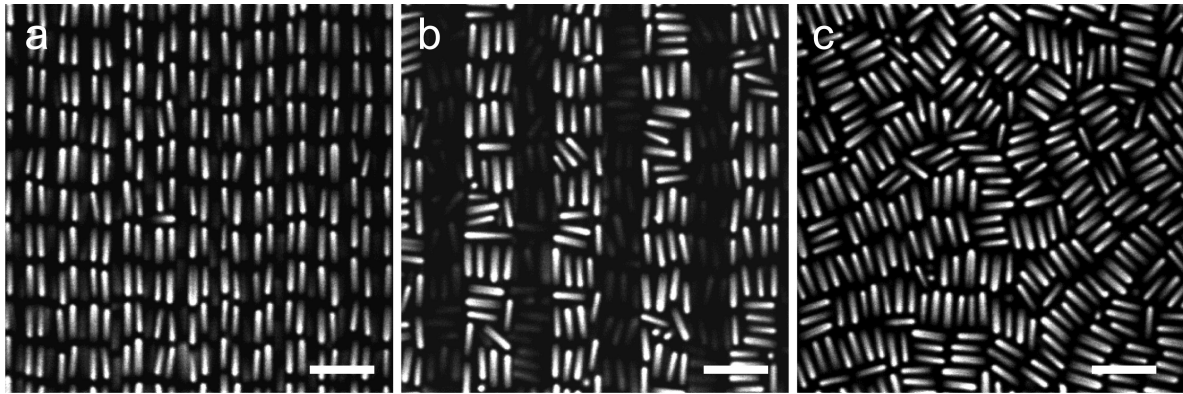
Het is namelijk mogelijk om de stroming alleen te gebruiken om de staafjes uit te lijnen, en vervolgens alleen de zwaartekracht het werk te laten doen. Zo ontstond er een uitgelijnde smectische fase op de bodem van de experimenteelcel. Een andere mogelijkheid is om de stroming gedurende het hele sedimentatieproces toe te passen. In dat geval vormde er zich geen smectische, maar een columnaire fase op de bodem.

Gestructureerde bodem

In Hoofdstuk 7 hebben we gekeken naar de invloed van de structuur van de bodem op het sediment van staafjes. Op een vlakke bodem oriënteerden de staafjes zich vooral parallel aan de bodem; ze lagen er plat op. Wanneer er echter een structuur van gootjes op de bodem was aangebracht, kon de oriëntatie van de staafjes nog meer beïnvloed worden. Afhankelijk van de breedte van de gootjes en de lengte van de staafjes zijn er verschillende effecten geobserveerd. Voor lange staafjes, die uit zichzelf al nematische en smectische fases vormen, maakte de breedte van de gootjes niet zoveel uit. Zelfs als de gootjes twee keer zo breed waren als een staafje lang is, gingen de staafjes nog steeds in de lengterichting van de gootjes liggen. Voor kortere staafjes was dit niet het geval, hier was duidelijk een betere uitlijning wanneer de breedte van de gootjes kleiner was dan de lengte van de staafjes (zie figuur 5).

BELANG VAN DIT ONDERZOEK

Het onderzoek naar staafvormige colloïden dat in dit proefschrift is beschreven valt onder de fundamentele wetenschap. In dit deel van de wetenschap draait het om kennis omwille van de kennis en niet om directe toepassingen. Dit wil niet zeggen dat die toepassingen er nooit komen. Veel belangrijke nieuwe uitvindingen zijn via



FIGUUR 5. Korte staafjes in gootjes van verschillende breedte. (a) In gootjes smaller dan de lengte van de staafjes wijzen de staafjes dezelfde kant op. (b) Minder goede uitlijning in gootjes breder dan de staaf lengte. (c) Staafjes op een vlakke bodem. De schaallijn geeft $5 \mu\text{m}$ weer.

fundamenteel onderzoek tot stand gekomen. De laser en de transistor zijn hier voorbeelden van. Toch waren de uitvinders van deze toepassingen hier niet expliciet naar op zoek. Het valt dus vaak niet goed te voorspellen wat de uitkomsten van fundamenteel onderzoek zullen zijn. Een recente toepassing waaraan onderzoek aan colloïden een grote bijdrage heeft geleverd is de elektronische inkt in e-readers. Ook de bijzondere eigenschappen van vloeibare kristallen worden toegepast, namelijk in LCD-schermen (Liquid Crystal Display). Het nieuw ontwikkelde systeem van staafjes dat in dit proefschrift is beschreven opent nieuwe deuren om vloeibare kristalfases te bestuderen en wie weet waartoe dat in de toekomst zal leiden.

Dankwoord

Een proefschrift komt vaak niet tot stand door het werk van één enkel persoon. Zo ook in dit geval. Op deze plaats wil ik graag een aantal mensen bedanken voor hun hulp en ondersteuning gedurende de afgelopen vier jaar.

Allereerst wil ik mijn promotor Alfons van Blaaderen en co-promotor Arnout Imhof bedanken voor de grote rol die zij als begeleiders hebben gespeeld bij dit project. De ruimte die ik heb gekregen om binnen het onderwerp mijn eigen weg in te slaan heb ik erg gewaardeerd. Bovendien zijn jullie adviezen en ideeën voor experimenten van grote waarde voor mijn onderzoek geweest.

Carlos van Kats, Gulşen Heessels-Gürboğa, Peter Helfferich en Judith Wijnhoven bedank ik voor het draaiende houden van het lab en voor alle ondersteunende diensten. Carlos wil ik bovendien bedanken voor het delen van al zijn kennis over silica syntheses. Voor al hun hulp op het gebied van elektronen microscopie wil ik Chris Schneijdenberg en Hans Meeldijk graag bedanken.

Al mijn collega's wil ik bedanken voor hun belangstelling en de fijne samenwerking. In het bijzonder noem ik Johan Stiefelhagen en Michiel Hermes, bij wie ik altijd terecht kon met een experimenteel probleem. Ook de samenwerking met Thijs Besseling gedurende de shearexperimenten was bijzonder waardevol. Thijs en Michiel, ook ontzettend bedankt voor al jullie werk aan de computercode om staafjes te tracken. Dmitry Byelov wil ik graag bedanken voor zijn grote bijdrage aan de X-ray scatteringexperimenten. Bart de Nijs, ook jij bedankt voor het meten bij nacht en ontij in Grenoble. Arjen van de Glind wil ik bedanken voor zijn introductie in analysetechnieken om mijn deeltjes te karakteriseren. Voor de experimenten met staafjes in een elektrisch veld bedank ik Rao Vutukuri voor de samenwerking op experimenteel vlak en Thomas Troppenz voor zijn belangstelling vanuit een theoretisch perspectief. Ook de studenten die ik begeleid heb, Nick Christogiannis en Bart de Leeuw, bedankt voor jullie bijdrage aan mijn onderzoek.

Mijn kamergenoten Ahmet Demirörs en Rao Vutukuri bedank ik voor wetenschappelijke en minder wetenschappelijke discussies. Voor niet-wetenschappelijke bijdragen aan een mooie promotietijd wil ik ook de rest van mijn collega's bedanken. Van altijd wel gezelschap om je gedachten te verzetten tijdens een pauze, het liefst met zelfgemaakte taart van Joost de Graaf, tot samen kanoën, kamperen, schaatsen en klimmen. Iedereen van de Soft Condensed Mattergroep die ik nog niet genoemd heb: bedankt voor alles!

Verder wil ik mijn ouders en zussen bedanken voor alle geloof in mij en steun te allen tijde. Mijn vader en schoonvader bedank ik voor het reduceren van het aantal type-,

taal- en spelfouten in dit proefschrift. En tot slot de persoon die werkelijk alle ups en downs heeft meebeleefd: Stijn, heel erg bedankt dat je er voor me bent en bent geweest! Volgens mij moet je ondertussen net zoveel weten van staafjes als ik!

Curriculum Vitae

Anke Kuijk was born on 3 December, 1983 in Deventer, The Netherlands. She graduated from the Eddy Hillesum Lyceum in Deventer in 2002, after which she began her study on Molecular Sciences at Wageningen University. After one year she decided to move focus to Physics at Utrecht University, from which she obtained her bachelor's degree in 2006 and her master's degree (cum laude) in 2007. As part of the bachelor program she worked on the improvement of the efficiency of evaporative cooling that is used for the creation of Bose-Einstein condensates, under supervision of Richard van der Stam and Peter van der Straten. During the master program Chemistry and Physics, she worked on the synthesis and phase behavior of binary mixtures of silica colloids in electric fields for one year. This research project was supervised by Job Thijssen, Dannis 't Hart, Esther Vermolen and Alfons van Blaaderen. In December 2007 she started her PhD research in the Soft Condensed Matter group at Utrecht University under supervision of Arnout Imhof and Alfons van Blaaderen. She presented her work at several national and international conferences, including physics@FOM, Playing Colloidal Mikado II, several Dutch Soft Matter Meetings, the Jülich Soft Matter days, the 7th Liquid Matter Conference and the 2nd International Soft Matter Conference. Her research on the synthesis and phase behavior of colloidal silica rods is described in this thesis.